Flexible Electronics for Large Area Sensing and Stimulation

Caroline Yu

Submitted in partial fulfillment of the

requirements for the degree of

Doctor of Philosophy

under the Executive Committee

of the Graduate School of Arts and Sciences

COLUMBIA UNIVERSITY

2020

ABSTRACT

Flexible Electronics for Large Area Sensing and Stimulation

Caroline Yu

Advancements in soft materials and hybrid flexible electronics have enabled developments in flexible circuits and wearables. Where rigid electronics are extremely precise over small physical areas, flexible electronics have the capability to sense over large curved areas. From the onset of epidermal electronics and flexible transistors, there have been great advancements in sensing over soft curved objects, such as human skin or brain tissue.

This thesis focuses on hybrid flexible electronics to sense and stimulate over large areas. The aim of the systems presented is to provide insight into complex navigation and sensor processing systems. In addition to the design, fabrication, and characterization of each device, several important characteristics of each device are investigated: material choice, curvature limits, and device sensitivity. The first device presented in this thesis uses strain gauges to track the bending of neurosurgery navigation stylets for catheter placement. The strain gauge fabrication and characterization is presented. Adhesive testing, stylet bending modeling, and noise techniques are also discussed as they were found to be critical components of the system. The device's limit of detection is 1 mm tip displacement. The purpose of the second set of devices presented is to gain object information from curved or edged robotic structures. Three sensing modes were explored: piezoelectric, strain, and capacitive. The piezoelectric sensor was founded to have a 6.7 times increase in sensitivity when an open-cell foam compliant layer is used. The strain sensor was found to have a gauge factor of 2.83 on a silicone layer and 1.5 on a polymer layer. The combination of the piezoelectric and strain sensing modes is presented. The capacitive sensor is able to detect object shape using inverse problem mathematical techniques. The third device and system presented is a flexible electrode array for stimulating the electroreceptors of electric fish. The spatial and temporal control of a conformal stimulation array enables the decoding of motor signals in the brain. The array fabrica-

tion and system development is presented. Surface modification of the electrode array successfully altered the surface energy of the array to match that of the fish for the optimal array-fish interface.

In summary, the development and integration of these flexible electronic devices has been achieved. It was found that the interface between the flexible electronic devices and binding objects is critical to device sensitivity and reliability.

Table of Contents

List of Figures

List of Tables

Acknowledgments

I would like to first thank my advisor, John Kymissis, for his unwavering cheerleading and guidance throughout my time in CLUE. His energy and expertise nurtures my research. Not only have I gained engineering experience, John has given me priceless advice for "getting to yes", difficult conversations, and presentations.

I would also like to thank my collaborators, in the order of when they stepped into my PhD life: Peter Allen, Verizon/NYC Media Lab, Synaptive Medical, Nathaniel Sawtell, Patricia Culligan, and Diego Restrepo. My exploration of flexible sensors began with their need for augmenting their exceptional research. A special thanks to Helen Xun Hou for being an amazing mentor and collaborator. To my collaborators who have spent countless hours debugging hardware and collecting data with me: Krista Perks, Jake Varley, Haokai Zhao, Connor McCullough, David Watkins, and Max Xu. To the high school interns, undergraduate students, and master's students, whose work has contributed to these projects: Joe Chen, Jai Smith, Carrie Hsu, Ben Golbin, Sarah Thompson, Narumi Wong, Jaylene Salas, and Yuliang Xu. It has been a rewarding experience to work with such motivated and intelligent scientists and engineers. Shoutout to Tian Sun and Jiho Yoon, who spent a short time in our lab and still exceeded all of our expectations.

Thank you to my thesis committee for your ideas and support: Peter Allen, Dion Khodagholy, Nathaniel Sawtell, and Jamie Teherani.

Thank you to Columbia University's electrical engineering administrative staff, specifically Elsa Sanchez and Laura Castillo, for always being there to help and guide me.

Thank you to the staff of Columbia's Nanofabrication Facility, especially Jaeeun Yu, James Vichiconti, and Nava Sternberg. You always go above and beyond to improve fabrication processes and equipment and listen to our thoughts and ideas.

Acknowledgements go to NSF IGERT for funding the first two years of my studies, NSF NRI for funding our research on robotics, Verizon's Open Innovation team and NYC Media Lab for their support on Plant Spike, Synaptive Medical for giving us the exceptional opportunity to work

Part I

Thesis

Chapter 1

Introduction

1.1   Motivation and Approach

Flexible technologies have brought about significant advancements in many fields, including consumer and medical industries. Because of their lightweight nature and ability to perform in high strain orientations, flexible technologies enable users to perform functions not possible with rigid devices. To highlight two use cases of flexible technologies ushering in a new era of consumer and medical devices, flexible displays and wearable medical monitoring devices will be presented.

Flexible displays take advantage of flexible substrates and advancements in fabrication processes. From Xerox PARC's electronic paper introduced in the 1970s [1] to Samsung's most recent OLED-based foldable phone [2], flexible displays use thin bendable substrates. In the case of electronic paper, a thin layer of transparent plastic was used. In the case of OLED-based displays, flexible plastic is also used instead of the standard glass substrates used in organic light emitting diode displays. Because OLED deposition does not require high temperature fabrication processes, roll-to-roll fabrication on plastic substrates is possible [3]. In addition to large advances in fabrication techniques, flexible displays are a testament to how advanced circuitry can help scale a device to high resolution and a multi-billion dollar industry. This thesis takes inspiration from flexible displays by using flexible printed circuit board substrate materials to reduce device weight and stretchable substrate materials to enable high device-bending angles.

Wearable medical monitoring devices have gained traction from improved sensor sensitivity and device lifetime. The most common health monitors include heart rate, blood oximetry, blood pressure, and ECG. Beyond these sensing modes, much work is still in the research and development phase. The focus on flexible electronics that conform to the human skin has ushered in a multitude of skin-like health monitoring devices [4–6].

From a more general standpoint, various materials and processes explored for flexible technologies include piezoresistive composites [7], silver nanowire networks [8], carbon nanotube films [9], and printing processes [10]. From a sensor device standpoint, an extensive list of sensor types has been explored [11]. The greatest challenges in flexible technologies include reliability and adaptability. To address the challenges of adopting current sensor technology to a flexible version, material exploration and characterization as well as sensor optimization is needed.

The sensors and systems presented in this thesis consist of stiff metals patterned on flexible and, sometimes, stretchable materials. From a materials standpoint, these devices are therefore hybrid devices, where the metal and substrates respond differently to mechanical strain. The mechanics of hard films on soft substrates has been extensively explored and has ushered in a new field of systems that combine hybrid biomedical and movement sensors with advanced circuitry and data analysis [12].

Each sensor presented in this thesis follows the same design approach: design, fabrication, characterization, design optimization, device prototype, and, finally, system development. Sensor design was completed in Layout Editor. Fabrication was completed in Columbia University's Nano Initiative cleanroom and the Columbia Laboratory for Unconventional Electronics. Custom PCBs were designed with Altium CircuitMaker and fabricated by PCB Minions. Various PCBs were also fabricated and assembled by MacroFab. Custom setups were built for each sensor's characterization.

1.2 Concepts

There are several concepts that this thesis is based upon. From materials to sensor technology, these concepts establish a foundation for flexible and miniature sensor technologies.

1.2.1 Flexible Materials

The flexible devices presented in this thesis have either polyimide or polydimethylsiloxane (PDMS) as their substrate. Polyimide is a polymer widely used in the electronic industry because of its resistance to heat and chemicals. For example, DuPont's Kapton CR polyimide film shrinkage at $400°C$ is 0.6% [13]. Both materials can be spin-coated and cured to form a thin layer. Other flexible material options include polyethylene naphthalate (PEN) and silicone rubbers (Ecoflex).

Property	PDMS	Polyimide
Young's Modulus (MPa)	~ 400	5000
Tensile Strength (MPa)	2.24	192
Mass Density ($\frac{g}{cm^3}$)	0.97	~ 1.4
Dielectric Constant	2.3 - 2.8	4 (106 Hz)

Table 1.1: Flexible material properties [13][14].

1.2.2 Piezoelectric Sensing

Piezoelectric materials generate electric charge from mechanical movement. Various movements of interest include pressure, force, or strain. Piezoelectric materials have a net dipole moment. When the material is mechanically stressed, charge is generated. A piezoelectric transducer can be modeled as a charge source with a shunt capacitor and resistor, as shown in Figure 1.1. The capacitance is determined by material size and properties while the resistance accounts for the dissipation of static charge [15]. When metal is placed on the top and bottom of the material, the charge generated can be measured by reading the voltage across the capacitor stack.

Polyvinylidene difluoride (PVDF) is the piezoelectric material chosen for the relative movement sensor presented in this work. PVDF has several properties that make it attractive for robotic tactile sensing: high mechanical to electrical conversion, large piezo strain constant, reasonable film thickness for sensor development, and relatively low Young's modulus compared to other polymers.
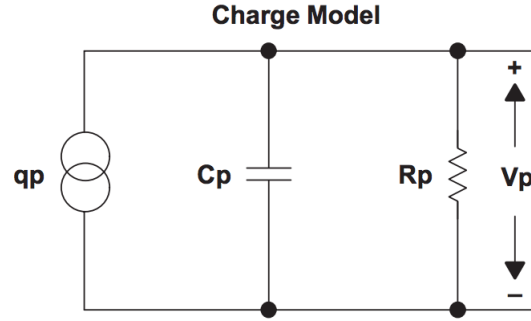
Figure 1.1: PVDF circuit model [15].

1.2.3 Strain Sensing

The classic strain gauge consists of a flexible substrate and a patterned metal foil. When the strain gauge is affixed to an object that bends, it will change in resistance while bending or compressing along an axis. An example commercial strain gauge (Figure 1.2) has a base resistance of 350 Ω, grid size of 2.5 mm $\times$ 2.9 mm, and aluminum as the self-temperature-compensation material.
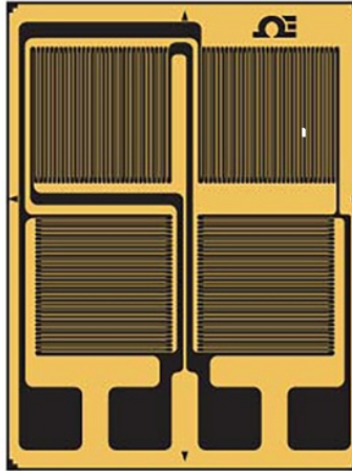
Figure 1.2: Commercial strain gauge [16].

A strain gauge's gauge factor (GF) relates applied strain to change in resistance:

$$GF = \epsilon \frac{\Delta R}{R_0}$$

where ϵ is the strain applied to the strain gauge, ΔR is the change in resistance from the applied

strain, and R_0 is the base resistance of the strain gauge. Thin-film strain gauges on flexible polymers act on the same principle; however, the strain mechanism varies with the material. The resistance of a thin-film strain gauge can be found using the following equation:

$$R = \frac{\rho L}{tw}$$

where ρ is the material resistivity, L is the trace length, t is the trace film thickness, and w is the trace width.

1.2.4 Capacitive Sensing

Capacitive sensors typically have a parallel plate capacitor plates and are used for pressure sensors in robotic applications. In the parallel plate configuration, the capacitance modulates if the distance between the two plates change:

$$C = \frac{\epsilon_0 \epsilon_r A}{d}$$

The fringing field of an object can also be used as a capacitor sensor. In this configuration, a different permittivity object will modulate the electric field as shown in Figure 1.3. Typically, electromagnetic simulations are performed to characterize the electric field with appropriate boundary conditions. Common applications include touch buttons, liquid level sensing, and object proximity detection.
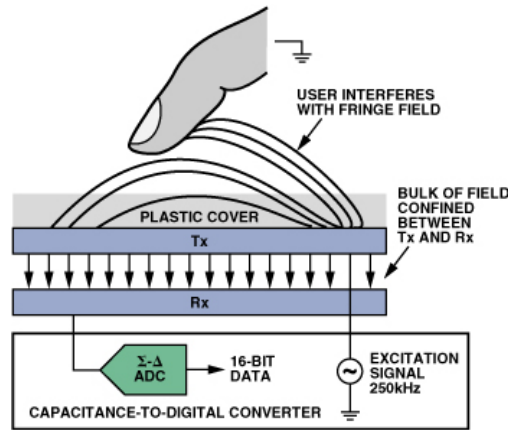
Figure 1.3: Typical fringing capacitance sensor [17].

1.3   Thesis Structure

This thesis is organized into four chapters:

Chapter 1 discusses a strain sensor to track the bending and tip location of neurosurgery placement stylets.

Chapter 2 discusses three types of flexible sensors to augment robotic grasping: piezoelectric, strain, and capacitive. The design, fabrication, characterization, and application of each sensor is presented along with the integration of sensing modes onto a one-layer device.

Chapter 3 discusses a flexible stimulation electrode array for neuroscience applications. The design, fabrication, and characterization of the electrode array is presented. The system design is also presented.

Chapter 4 presents a low-cost low-power BLE-connected IoT module for monitoring soil health and environmental features including temperature, light intensity, soil moisture, and pH. The PCB design, BLE usage, and experimental data are presented.

Two projects in the appendices are presented. The first appendix discusses an ITO electrode array for neuronal recordings. The second appendix discusses correlating a mouse's external environment with neural responses by combining sound detection and mouse head and pinna movement data on a small implanted PCB.

Chapter 2

Strain sensor for the tracking of neurosurgery stylet bending[1]

2.1 Motivation

A sensing device by its simplest definition consists of a sensor that transforms an input to an electrical signal. The electrical signal is conditioned and integrated into a part of a system.

The first sensing device presented in this thesis consists of a strain gauge sensor to track the bending of a navigation stylet during surgical insertion. Neurosurgery procedures are often complex; surgeons need to locate tissue and how it relates to neighboring brain tissue before and during a procedure. For procedures that remove a meningioma, or often-benign slow-growing tumor, navigation and senses are used to remove the tissue with minimal brain damage. Polymer catheters are typically navigated and placed by using trackable metal stylets. Various technology exists to track the stylet as a whole entity [18]. An example navigation and white matter simulation is shown in Figure 2.1. Synaptive Medical's BrightMatter^{TM} Guide system incorporates dynamic tractography with intraoperative instruments. Surgeons are therefore able to accurately execute a

---

[1]Based on C. Yu, K. Kam, M. R. Cavallari, and I. Kymissis, *Tip Tracking of Surgical Navigation Stylets Using Integrated Strain Sensors*, 2020 IEEE International Conference on Flexible and Printable Sensors and Systems (FLEPS), *Submitted*.

planned approach and minimize any unwanted tissue damage.

<div align="center">(a)</div>

<div align="center">(b)</div>
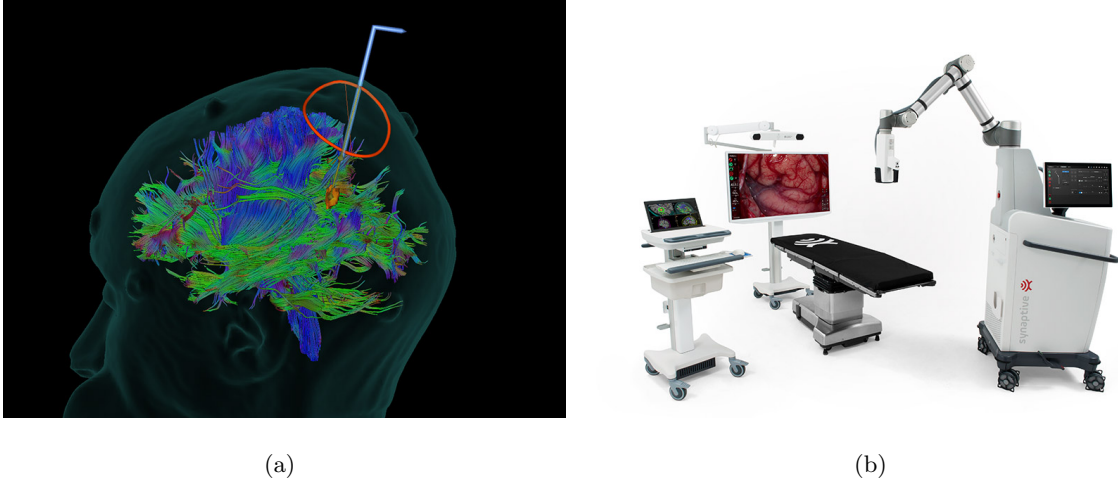
Figure 2.1: (a) Surgical navigation with white matter tractography and stylet tracking [18]. (b) Operating room with navigation technology. [18]

As the navigation stylet is placed into the brain to reach the desired location, pressure from brain tissue has been found to bend the stylet tip. Although the stylet as a whole entity may be accurately tracked, the precise location of the tip is unknown. In this environment, a mechanical or non-optical option is necessary to locate the stylet tip location.

Various sensors have been demonstrated to measure tissue hardness as well as surgery or EEG electrode bending. These sensors include force sensors [19–22] and a piezoresistive tactile sensor [23]. Previously demonstrated electrode bending measurement systems use material assumptions and implementation plans [24–27]. These sensors have several characteristics that make it unsuitable for the application at hand such as having a large form factor, being difficult to add onto existing systems, and requiring line of sight for optical tracking. Hosseinabadi et al. (2019) demonstrated a complete system that tracks robotic shafts using optical force sensing with tenths of microns accuracy; however, the diameter of the device is more than eight millimeters, which is unsuitable for neurosurgery applications [28].

The key requirements for this application include high accuracy for stylet tip deflections between 1 mm and 1 cm and being minimal in size when integrated with existing navigation systems. This

chapter discusses a strain gauge sensor and system for tracking the bending of neurosurgery stylets. The strain gauges are integrated at the base end of a surgical stylet to track its bending. The location of the strain gauges at the base end of the stylet allow for minimal to no contact with brain tissue. When force from brain tissue at the stylet's tip causes the stylet to bend, the strain gauges wrapped around the stylet are strained and their resistances change. The fabrication and characterization of metal strain gauges on polydimethylsiloxane (PDMS) as well as polyimide is demonstrated. The strain gauges can record movement in a two-dimensional plane and are wrapped around a 1.3 mm diameter industry-grade stylet used in neurovascular surgical procedures. By combining strain gauge design optimization, device-stylet adhesive optimization, and low-noise signal processing techniques, the device presented in this chapter has a limit of detection of 0.75 mm tip displacement.

2.2 Methodology

2.2.1 Fabrication and Adhesion

A thin-film silver strain gauge sensor is patterned onto PDMS (Sylgard 184, Dow Corning) and is then adhered to a 1.3 mm diameter ventricular catheter placement stylet (Brainlab).
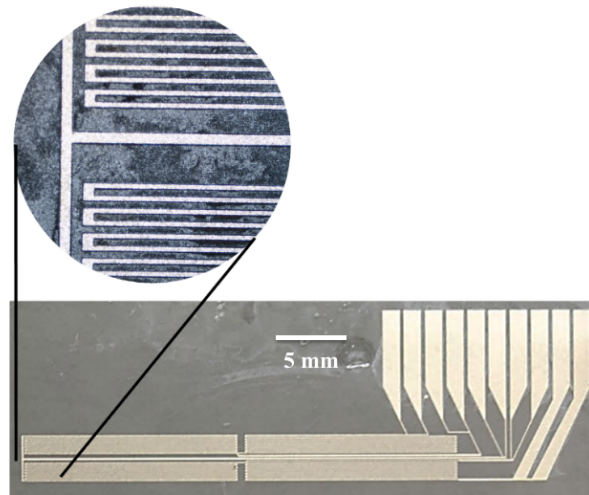
Figure 2.2: Strain gauge sensor serpentine design with electrode pads.

A serpentine strain gauge design is used to provide a large base resistance in a small surface area as shown in Figure 2.2. The base resistance is calculated using Equation 2.1 where R is the base (unstrained) resistance, ρ is the resistivity of thin film silver, L is the total length of the strain gauge trace, t is the thin-film thickness, and w is the serpentine trace width. The fabricated device has a total trace length of 16.5 cm, trace metal film thickness of 60 nm, and trace width of 25 μm. Each strain gauge has a base resistance of 3.3 kΩ over a surface area of 14 mm^2.

$$R = \rho \frac{L}{tw} \tag{2.1}$$

The fabrication process flow is shown in Figure 2.3. First, a glass carrier (100 mm soda lime, University Wafer) is cleaned, treated with UV/ozone plasma, then exposed to trichloro(1H,1H,2H,2H-perfluorooctyl)silane (Sigma Aldrich) in a desiccator as an anti-adhesion monolayer. PDMS is spin-coated to a thickness of 70 μm using the static dispense technique and cured at 100°C for 1 hour (Dow Corning). 60 nm of silver is thermally evaporated and positive photoresist (S1811) is spin-coated onto the silver. The sample is then exposed using a mask aligner (SÜSS MicroTec MA6) and developed in AZ300MIF (Integrated Micro Materials). The silver is wet-etched using silver etchant (Transene).
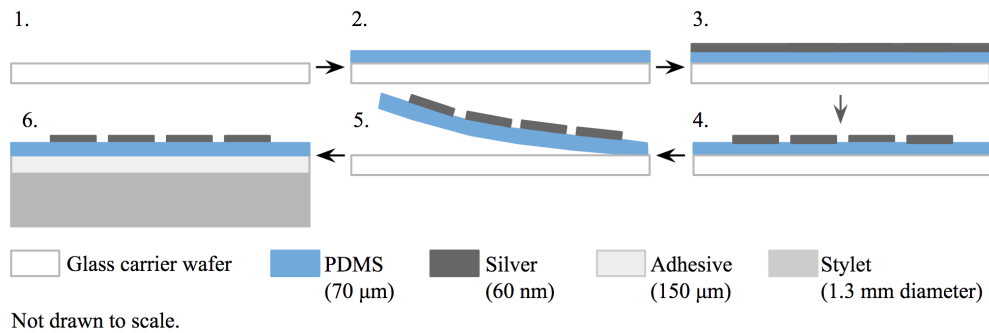
Figure 2.3: Strain gauge sensor fabrication process flow.

To adhere the strain gauges onto the stylet, the PDMS is peeled off the fabrication carrier glass wafer by rolling it onto a carrier rod. Then, the strain gauge is rolled off the rod onto silicone gel adhesive (PS-1829, Polymer Science) and placed on top of acrylic double-sided tape (3M-9629PC,

3M). Finally, the acrylic side is rolled onto the navigation stylet. Spring-back 302/304 stainless steel wire was used as a phantom stylet (McMaster Carr). A navigation tracker was 3D printed with an area to hold and stabilize the heat seal connection on a custom PCB.

Pull-off strength adhesive testing was performed to determine the adhesive strength of various adhesives to PDMS and the stylet (ASTM D4541-17) (Figure 2.4). The adhesive characteristics taken into consideration were adhesive material, adhesive thickness, and backing material. Various adhesive materials have different bonding strengths to PDMS and metal. The adhesive's thickness affected the ease of the adhesion process and gauge factor. The backing material affected the ease of the adhesion process as well.

For the adhesive characterization testing, various adhesives were attached to a flat thin layer of stainless steel. PDMS was then adhered to the top adhesive layer. Tweezers were securely affixed to an Admet force testing machine to pull the PDMS layer. PDMS delaminated from the adhesive layer or both the PDMS and the adhesive delaminated from the stainless steel layer; whichever condition occurred demonstrated which interface had stronger adhesion. A simple ranking of adhesive strength was first generated to determine which adhesives should be tested using the pull strength test. Adhesives are shown in Table 2.1 and 2.2.

The combined adhesive stack of PS-1829 and 3M-9629PC has a pull strength of 1.33 $\pm$ 0.081 N/cm while PS-2151, a double-sided silicone gel / acrylic adhesive, has a pull strength of 1.18 $\pm$ 0.143 N/cm (Figure 2.5).
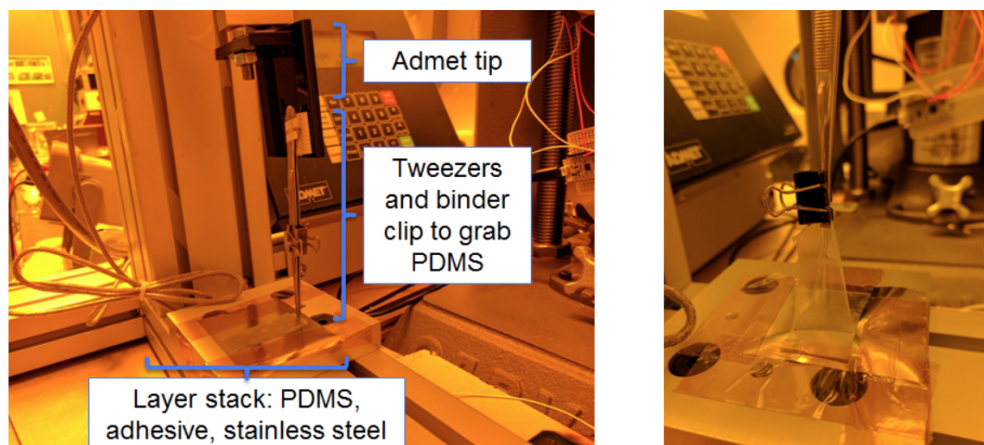
Figure 2.4: Pull-off strength adhesive testing setup.
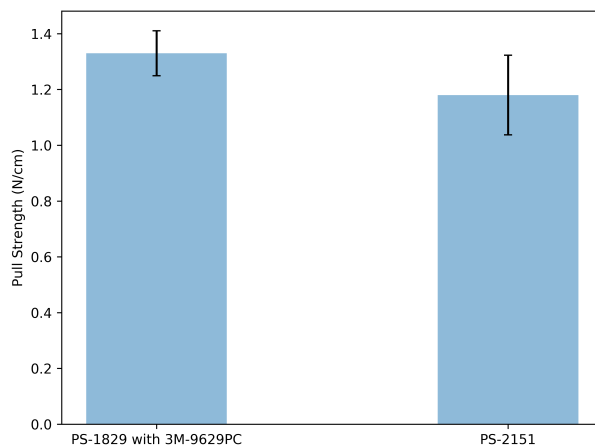
Figure 2.5: Adhesive pull-strength results.

Tape	Material	Thickness (μm)	Adheres well to:
3M 4905	VHB	500	polycarbonate, acrylic
3M 9629PC	Acrylic	89	high/low surface energy plastics
3M 9626	Acrylic	50	irregular surface plastics
3M F9469PC	Acrylic	130	broad range of surfaces

Table 2.1: 3M adhesive list.

Adhesive	Adhesive Stack	Adhesive + Material Stack	Total Adhesive Thickness (μm)	General Pull Scale (1 - 10)
PS-1829	silicone gel	silicone gel + stainless steel sheet	180	2
PS-1829	silicone gel	silicone gel + double stick acrylic tape + stainless steel sheet		7
PS-2041	silicone gel + polyurethane carrier + acrylic	silicone gel + polyurethane carrier + acrylic + stainless steel sheet	220	2
PS-2041	silicone gel + polyurethane carrier + acrylic	acrylic + polyurethane carrier + silicone gel + stainless steel sheet	220	6
PS-2151	silicone gel + polyurethane carrier + acrylic	silicone gel + polyurethane carrier + acrylic + stainless steel sheet	220	2
PS-2151	silicone gel + polyurethane carrier + acrylic	acrylic + polyurethane carrier + silicone gel + stainless steel sheet	220	7

Table 2.2: Polymer Science adhesive list and characterization.

2.2.2 Modeling

Once the strain gauges are adhered to the stylet, the stylet's bending and tip displacement from an unbent position is calculated using a cantilever beam deflection model, as represented in Equation 2.2 [29]. In this model, y is the tip displacement of the stylet, F is the applied force at the tip, E is the elastic modulus of the stylet, I is the moment of inertia about the stylet's neutral axis, x is the position along the length of the rod with origin at the deflecting end, and L is the length of the stylet.

$$y = \frac{F}{6EI}\left(-x^3 + 3L^2x - 2L^3\right) \tag{2.2}$$

The device is placed at the base of the stylet for maximum strain, as shown in Figure 2.9. Placing the sensor at the base end of the stylet also limits contact with brain tissue; the device is expected to remain outside the brain during a neurosurgical procedure (Figure 2.6).

The sensor consists of four strain gauges. When the device is wrapped around the stylet, one pair of strain gauges covers one quadrant of the stylet's circumference. Another pair of strain gauges is placed on a quadrant translated 90 degrees from the other quadrant. This placement of strain gauges allows two axes of movement to be tracked simultaneously, which are represented as x and y in Figure 2.6. Each pair of strain gauges consist of two strain gauges, which track strain along two different sections of the stylet. Electrode contact pads utilize four-terminal sensing and are oriented perpendicular to the length of the stylet for eliminating connector delamination.

The system block diagram is shown in Figure 2.7. The present setup uses source-meter circuitry, where flexible heat-seal connectors connect the device's electrode pads to a custom printed circuit board (PCB) with corresponding metal pads. The custom PCB connects to a current source and microcontroller analog inputs (Atmel SAM3X8E). Exponential moving averaging on the microcontroller processor is used to reduce high frequency and summing noise. The processed data is sent to a PC serial monitor for tracking and storage.
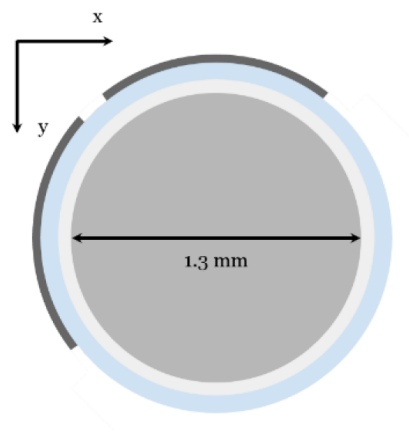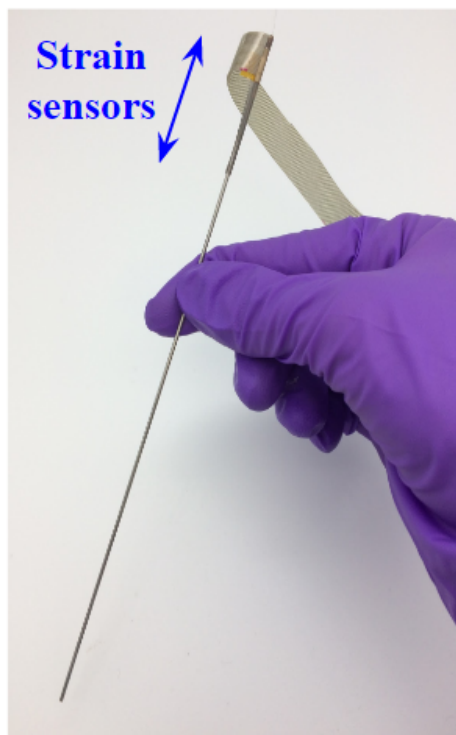
(a)   (b)

Figure 2.6: (a) Cross-section of the device / stylet. (b) Device adhered to the base of the stylet.

```
┌──────────────────┐     ┌──────────────────┐     ┌──────────────────┐
│  Strain gauge +  │─────│ Flexible connector│─────│  Source/measure  │
│  adhesive stack  │     │                  │     │    circuitry     │
└──────────────────┘     └──────────────────┘     └──────────────────┘
         │                                                  │
┌──────────────────┐                             ┌──────────────────┐
│ Navigation stylet│                             │        PC        │
└──────────────────┘                             └──────────────────┘
```
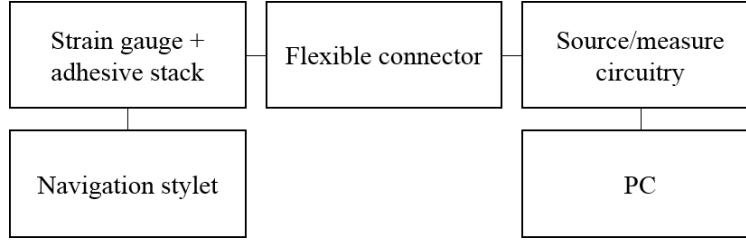
Figure 2.7: System block diagram.

The stylet tip displacement is determined by using the gauge factor of the device and the change in resistance with applied strain as shown in Equations 2.3, 2.4, and 2.5 [29]. ΔR is the measured change in resistance, R_b is the strain gauge's base resistance, GF is the gauge factor of the device, E is the stylet's elastic modulus, and z is the section modulus of the stylet.

$$y = -\frac{Fl^3}{3EI} \tag{2.3}$$

$$-\frac{3yEI}{l^3} = F = \frac{E\epsilon z}{l} \tag{2.4}$$

$$\frac{Fl}{Ez} = \epsilon = \frac{\Delta R}{R_b \cdot GF} \tag{2.5}$$

To simulate y displacement at each x location along the stylet, the cantilever beam model was placed into Matlab. A setup was built to measure the experimental displacement of the stylet when a force is applied at the tip, as shown in Figure 2.9. Simulation results compared to actual results are shown in Figure 2.10.
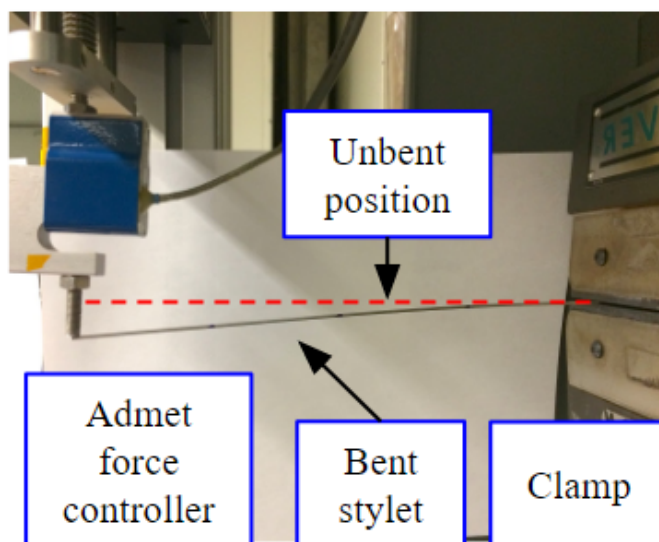
Figure 2.8: Cantilever beam model verification: setup for applying varying force at the stylet tip while the stylet base is clamped.
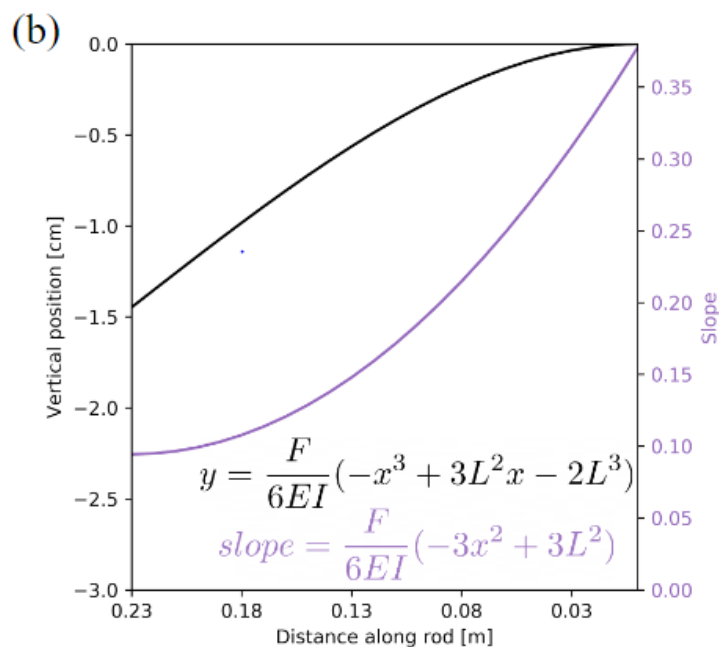
Figure 2.9: Cantilever beam model verification: simulated stylet location and slope with 0.1 N applied at stylet tip.
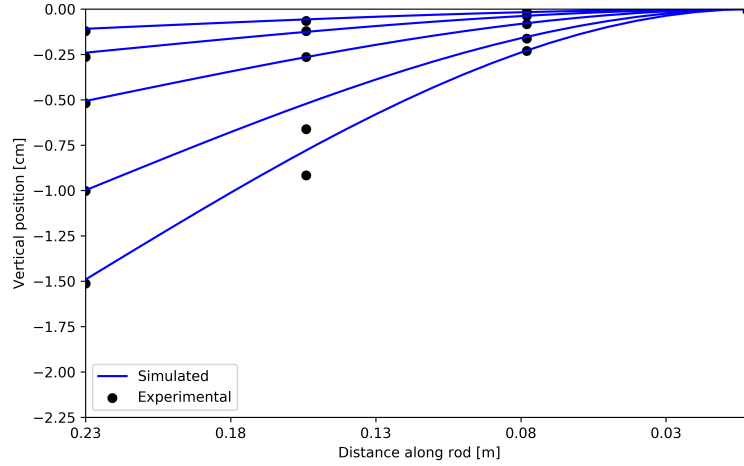
Figure 2.10: Cantilever beam model verification: simulated vs. experimental rod location with various tip displacement (1, 2.5, 5, 10, 15 mm).

The strain gauges were adhered to the stylet to determine the response to stylet tip displacements in two directions. The measurement setup and characterization is shown in Figure 2.8. One end of the stylet was clamped to a manual press. The other end of the stylet is displaced by various amounts using a force testing system (Admet eXpert 5600). A source-meter unit (Agilent B2901A) is used to source current and measure changes in voltage of the individual strain gauges.

Noise characterization was conducted to reduce the noise floor of the sensor. Because the desired tip displacement to noise level ratio (SNR) of the device was relatively low when measuring with a Keithley source/measure unit, it was necessary to use averaging and optimize the sampling rate. The normalized resistance of the strain sensor over time at various sampling rates is shown in Figure 2.11a. The corresponding standard deviation at each sampling rate is shown in Figure 2.11b. The standard deviation with respect to average window using simple moving averaging is shown in Figure 2.12. As expected, there is a decrease in noise when the average window is increased from 0 to 100 samples. With a simple moving average, the limit of detection is 1.1 mm stylet tip displacement.

When the sensor is connected to the analog inputs of a microcontroller instead of a source/measure unit, the noise floor is an order of magnitude higher. Therefore, it is necessary to utilize other aver-

aging techniques to achieve the same noise floor when using benchtop tools. When using a simple moving average, it is necessary to average over nearly 1000 samples at 100 kHz to achieve the same noise floor of 0.014. However, the effective sampling rate is 100 Hz, which is still greater than the maximum benchtop sampling rate.

Using an exponential moving average with a smoothing factor of 0.2, older observations are discounted less fast. This type of average also reduces the summing noise error found by using a simple moving average. It was found that this average reduces noise from poor contact connections. At an effective sampling rate of 30 Hz, the noise level is 0.0043 V at rest, which corresponds to ~200 μm tip displacement. This noise floor is an order of magnitude less than that when using a simple moving average, and allows the limit of detection to be less than the required 1 mm tip displacement limit of detection.
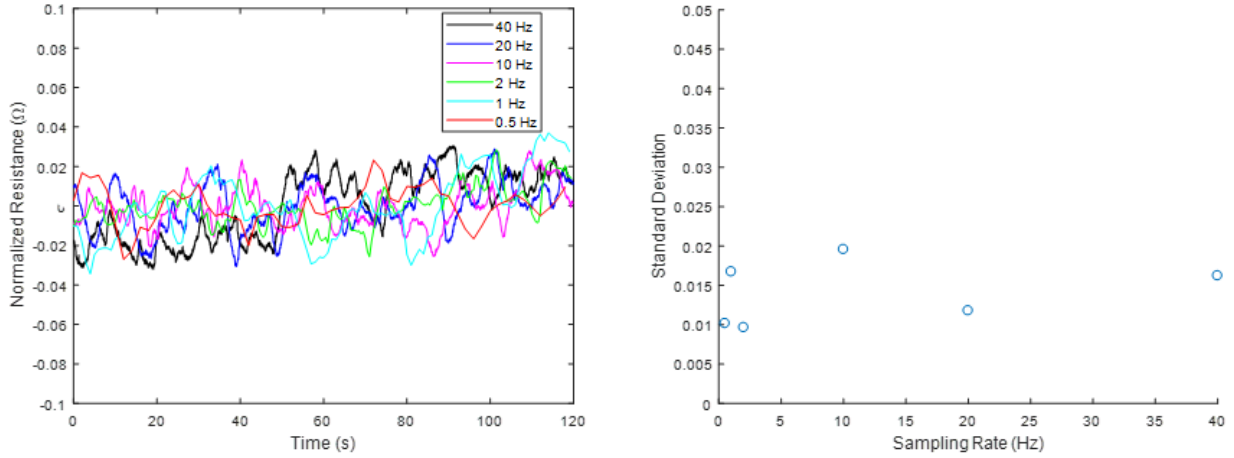
Figure 2.11: Noise floor characterization. (a) Normalized base resistance of the strain sensor at rest. (b) Standard deviation at various sampling rates.
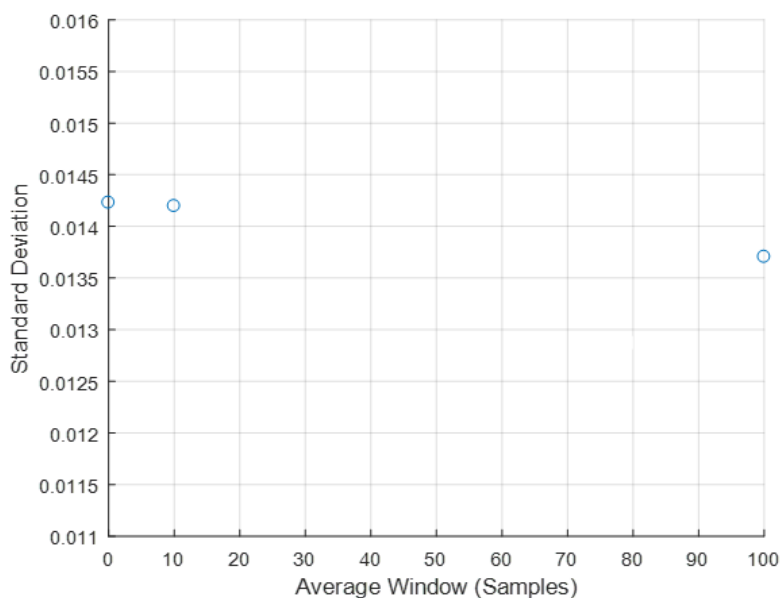
Figure 2.12: Simple Moving Average.

To eliminate drift and decrease contract manufacturing cost, a copper strain gauge on polyimide was also explored. Polyimide is a polymer commonly used in flexible printed circuit boards and as a thermal or electric insulation layer. As polyimide films are flexible but not stretchable, the higher tensile stiffness allows for easier handling during fabrication processes and more uniform bending.

Contract manufacturing exploration was performed. Companies that provide fast turn-around time are able to pattern copper traces on polyimide film. Typically, this companies have relatively thick trace limitations. Companies with longer turn-key time are able to pattern higher resistance metal on polyimide film. A comparison of vendor capabilities with the work performed in this chapter is shown in Table 2.3.

Company	PCB Minions	All-Flex	Prototype
Metal Material	Copper	Inconel 600	Silver/gold
Minimum Trace Width (μm)	100	127	**~20**
Minimum Trace Thickness (μm)	12	12.7	**0.06**
Metal Resistance (mΩ/square)	0.6	78.4	$\sim$ **400**
Substrate Material	Polyimide	-	Varies
Substrate Thickness	**25.4 μm**	130	Varies
Cost	**~\$300**	\$8.50 for 500	N/A
Turn-key Time	5 business days	5 weeks	**2 days**

Table 2.3: Vendor comparison for strain gauge sensor
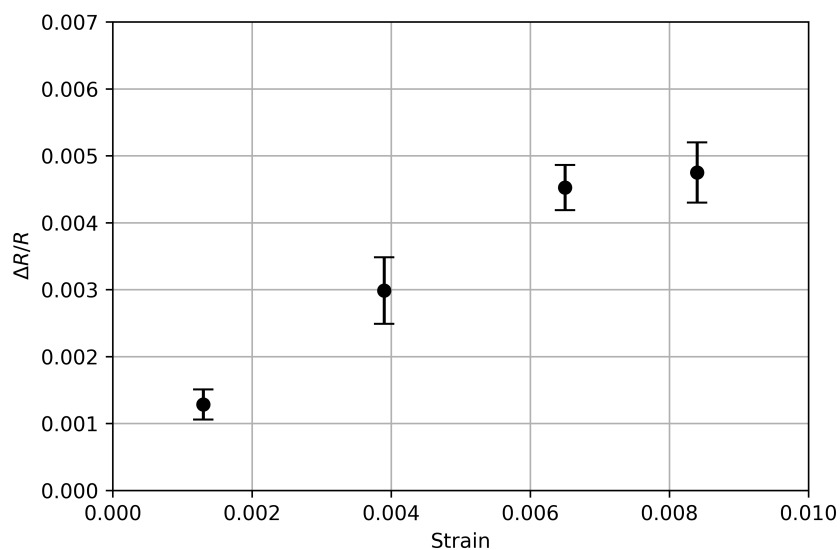
Figure 2.13: Copper strain gauge on polyimide responds linearly over 1 to 7 millistrain with a gauge factor of 0.624.

2.2.3 System Integration

The first prototype consisted of strain gauges connected to a microcontroller breakout board. The voltage across each strain gauge is measured using the analog inputs of a microcontroller. The programmable microcontroller used in this project is Cypress PSoC 5LP, which has analog multiplexers and a 12-bit SAR ADC on board. The heat seal connectors allow the analog nodes to be connected to the PSoC 5LP pins on a custom PCB (Figure 2.14).
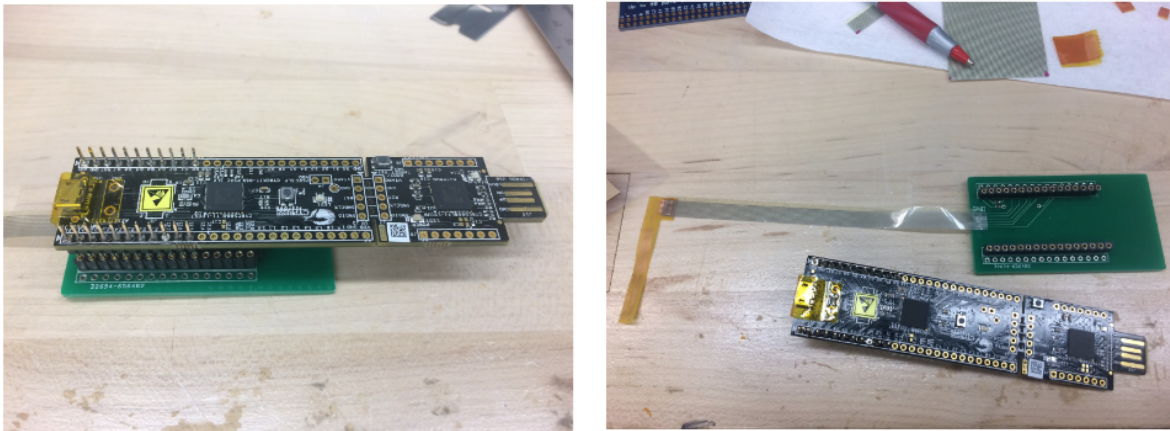
Figure 2.14: Strain gauge sensor connected to PSoC 5LP custom breakout board.

Because of the low signal to noise ratio, a custom source-meter circuit was designed. A programmable current source (LT3092, Analog Devices) is used to provide current. The current is set by the ratio of two resistor values. By taking into account the base resistance of the strain gauges and expected swing values, the current source is designed to provide 250 μA of current. A four input sigma-delta ADC IC was used to measure the change in voltage across each strain gauge (ADS1015, Texas Instruments). As the stylet bends and the strain gauge resistance modulates, the ADC tracks the change in voltage, and thus, resistance of the strain gauges. The ADC communicates with external data collection and storage via an I2C bus. The schematics for each circuit section are shown in Figures 2.15 and 2.16.

The custom PCB is shown in Figure 2.17. On the left-hand side of the PCB, exposed copper electrode pads provide a connection input for the strain gauges. The pads correspond to the heat

seal connector used (Elform). The PCB's inputs include power and ground pins and the PCB's outputs include the I2C communication channels - clock and data lines. Test points allow for debugging of the PCB. Altium's CircuitMaker software was used to design the PCB and PCB Minions was used to fabricate the PCB.
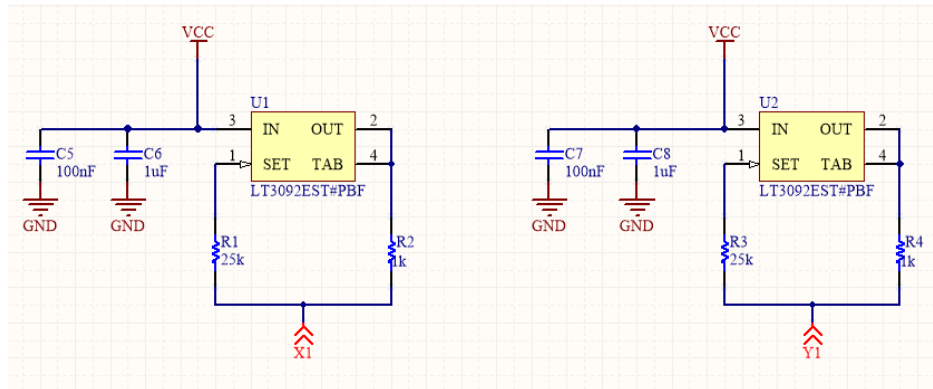
Figure 2.15: Current source schematic.
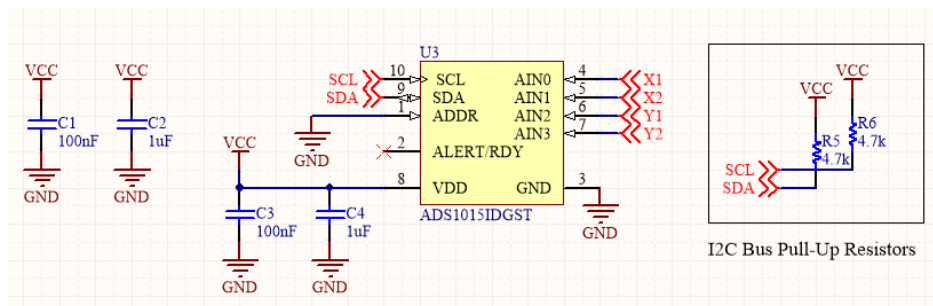
Figure 2.16: ADC and peripherals schematic.
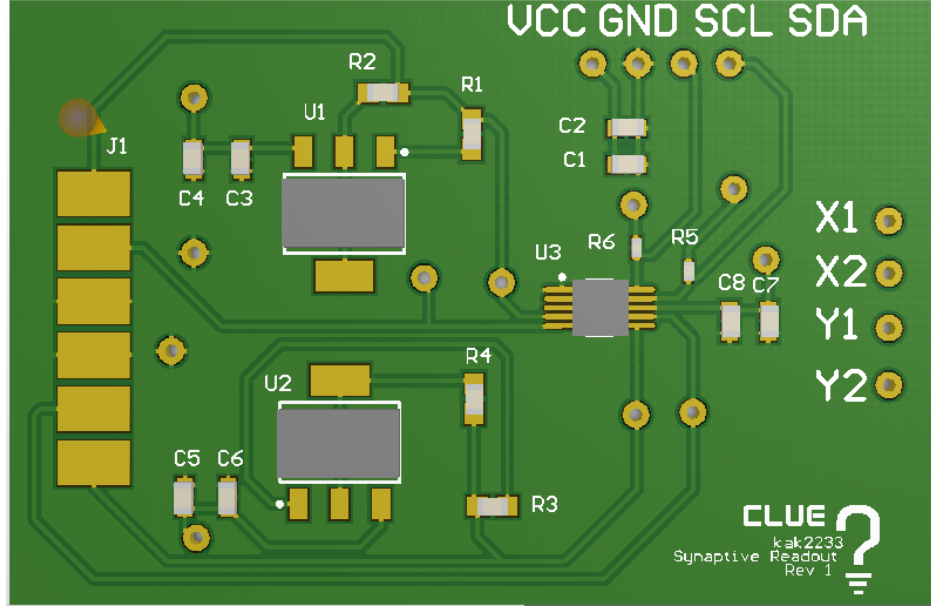
Figure 2.17: Source-meter circuit PCB.

2.3 Results

To determine the gauge factor of the device, bending induced strain was applied to the strain sensors. Acrylic arcs of various radii were manufactured and the strain gauges were bent over the circumference of the arcs. The strain sensor's response to strain and corresponding tip displacement is shown in Figure 2.18. The normalized change in resistance with response to strain is shown. The range of applied strain corresponds to tip displacement from a neutral position from 3 - 11 mm.

The applied strain can be calculated using Equation 2.6, where T is the total device thickness and r is the bending radius.

$$\epsilon = \frac{T}{2r} \tag{2.6}$$

The stylet tip displacement can be estimated by knowing the gauge factor of the device and the change in resistance with applied strain as shown in Equations 2.3, 2.4, and 2.5. The strain gauges were adhered to the stylet to determine the response to stylet tip displacements in two directions. The measurement setup is the same as that used for the rod bending characterization.

With a noise floor of 4.3 mV and corresponding noise displacement of 250 μm, the minimum
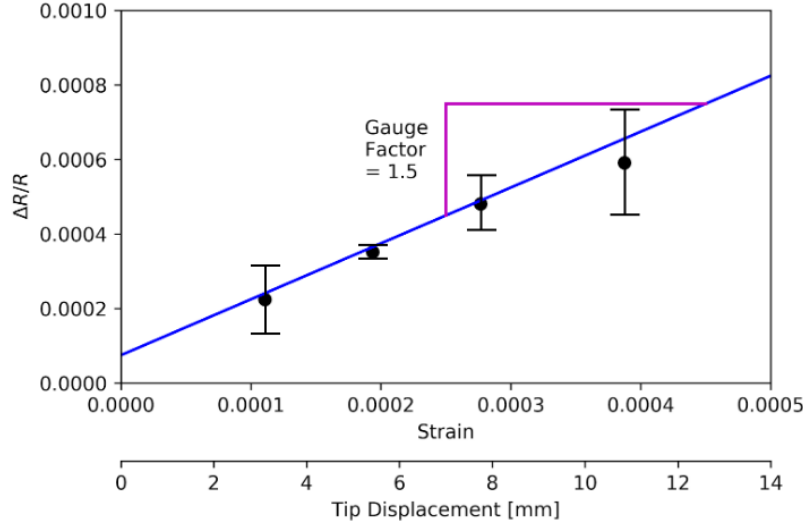
Figure 2.18: The gauge factor of the silver strain gauge on PDMS and the corresponding change in resistance with respect to strain / stylus tip displacement.

detectable tip displacement in both axes is 750 μm. When wrapped around and adhered to the stylet, the strain gauges display linear behavior between 2 and 10 mm of tip displacement and have a gauge factor of 1.5 under tension; this is comparable to 2.3 when the strain gauge is strained on a planar surface. The sensor therefore provides linear behavior similar to state-of-the-art sensors while being able to track the bending of a thin neurosurgery stylet. Neurosurgery research has shown that ventricular catheter placement has errors ranging from 5.7 - 9.6 mm [11]. The device presented in this work with tip displacement tracking of 1 - 11 mm compares well to the error ranges present in the field.

The fabricated device is able to track two orthogonal directions. As shown in Figure 2.19, tip displacement in the vertical direction leads to an increase in resistance response in the y direction but not the x direction. The combination of the x and y strain gauge outputs can be used to monitor tip displacement with two degrees of freedom.

To correlate the strain gauges' change in resistance to the stylet's tip displacement, one end of the rod was secured with a manual press and the sensor was attached to the near end of the secured end, as shown in Figure 2.8. This placement leads to the larger concavity when the rod is bent, as
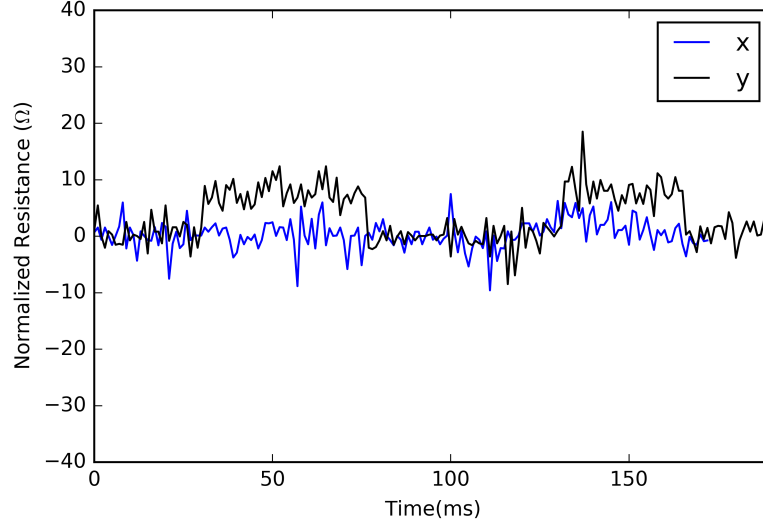
Figure 2.19: Tip displacement in the y direction showing no signal in the x direction.

shown in Figure 2.8. An Admet force testing system was used to apply various amounts of force at the stylet tip while the strain gauges were connected to a source/measure unit (Agilent B2900A).

When wrapped around and adhered to the stylet, the strain gauges display linear behavior between 2 and 10 mm of tip displacement and have a gauge factor of 1.5 under tension; this is comparable to 2.3 when the strain gauge is strained on a planar surface. The sensor therefore provides linear behavior similar to state of the art sensors while being able to track the bending of a thin neurosurgery stylet. At the limit of detection of 1 mm, the signal to noise ratio is 2.64.

Compared to the fabricated device, the copper-on-polyimide device purchased had a lower gauge factor. With 101.6 μm strain gauge trace width on 25.4 μm thick polyimide purchased from PCB Minions, the gauge factor of the device was found to be 0.624.

2.4 Conclusion and Outlook

For the first time, the tip of a 1.3 mm diameter neurosurgery navigation stylet can be tracked with on-board strain sensors. The device presented can track tip deflection between 1 and 11 mm in two directions. The placement of the device at the base of the stylet does not interfere with existing

navigation techniques as the device would not come into contact with brain tissue. The device is also conformal so that the user's ability to hold the stylet is not compromised. An optimum flexible adhesive stack was determined for PDMS / metal stylet adhesion.

The strain sensor device and system design presented in this chapter will enable neurosurgery companies to augment their existing navigation tools to aid neurosurgeons to reduce tissue damage and streamline catheter placement. Because of the millimeter limit of detection required, the adhesive characterization and signal processing presented were necessary components to the success of the system.

Regarding future vendor fabrication and device implementation, sensor placement and consistency will be a key aspect to producing uniform results when using the strain sensor. Alignment marks on the design and rod can help vendors place and align the sensor onto the rod.

In the future, we plan to integrate a microcontroller for data readout and collection and a Bluetooth Low Energy (BLE) module on a flex PCB circuit with a battery power supply for real-time wireless data transmission during surgical procedures. Future testing of this system will include surgical testing to analyze the stylet's movement through a brain tissue simulator model and tip tracking with more than 2 degrees of freedom. Our proposed system would seamlessly integrate with existing surgical navigation systems and can facilitate improved navigation procedures.

Chapter 3

Electronic Skin for Robotics[1]

3.1 Motivation

Sensors for robotics have enabled personable human interactions with robots, improved factory throughput, and advances in robotic techniques. Various commercial and industrial robotic applications that use sensors include human gesture recognition, robot movement tracking, and monitoring hard-to-access environments. Typically, the sensors embedded in robotic structures are rigid. Their rigidity often allows high durability and manufacturability. Example sensors and systems are shown in Figure 3.1.

Two specific drawbacks of using rigid sensors for robotics are (1) the inability to sense around bent or edge areas and (2) having a low dynamic range. To enable sensor adaptability over a broad range of robotic structures and increase available information and sensitivity for robotic learning techniques, it is necessary to develop flexible robust sensors.

The mechanical compliance and sensitivity of flexible sensors have enabled improved haptic feedback and object manipulation. Many flexible sensors have been demonstrated for tactile applications [32–37]. These sensors are often relatively thick at 0.3 - 1 mm; their bending radius is therefore limited. For a bending angle greater than 45 degrees, we propose using thin flexible

---

(a) Taiker Robot [30].

(b) TDK Robot Sensor Solutions [31].
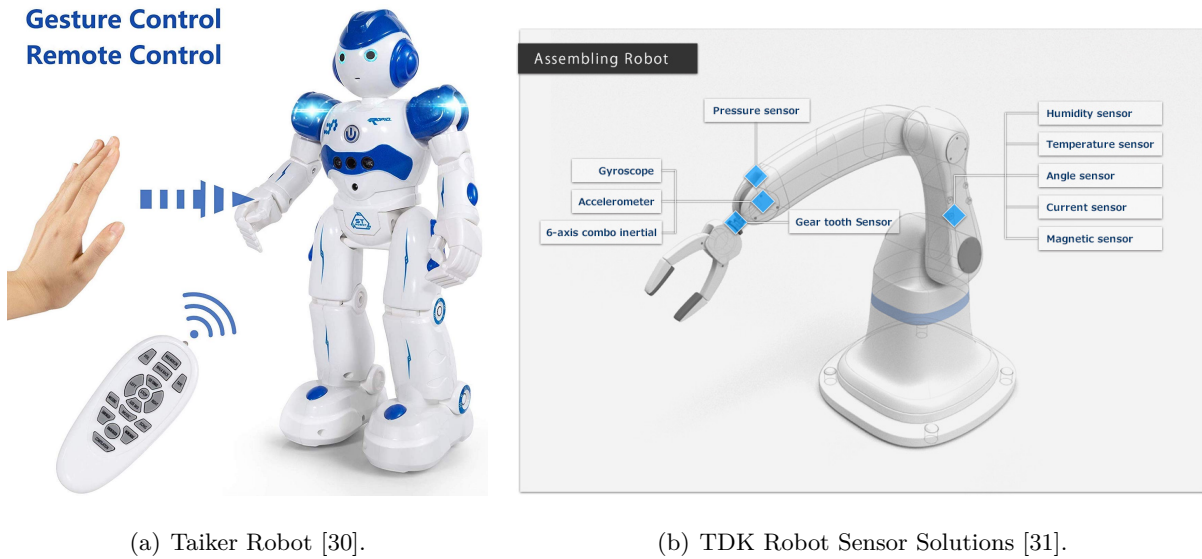
Figure 3.1: Commercially and industrially available robots.

materials as the substrate layer and thin-film metals as the sensing layer. This choice of materials allows for active sensing areas to be bent and placed on edge and high curvature robotic structures. The sensors presented in this chapter have thin piezoelectric polymer films or silicone layers as the substrate layers and thin-film metals as the sensing layer.

Combining multiple tactile sensing modes into one device has also been extensively explored [33, 38–41]. Someya et al. (2004) set the foundation for electronic skin with a large-area, flexible pressure sensor matrix with organic field-effect transistors [38]. Nawrocki et al. (2016) continues work in Someya's group demonstrated 300 nm thick biocompatible electronic skin with tactile sensors [39]. Work from Zhenan Bao's and John Roger's groups has demonstrated highly sensitive resistive pressure sensors [40] and strain gauges [33]. The goal of the work presented in this chapter is to enable a robot to sense relative and absolute pressure by augmenting robotic grasping with piezoelectric and strain sensing modes. The key feature of the presented sensors is the ability to place the sensors on varying robotic structures so that they do not necessarily need to be embedded when the robotic hand is manufactured; this augmentation will allow for more rapid robotic grasping testing and development.

The two robotic applications explored in this chapter are grasping and imaging. Robotic grasp-

ing consists of enabling a robot to pick up objects in its surrounding environment. From perception to planning to control, there are many aspects of robotic grasping that are currently being developed in the robotics field. There are several existing methods of robotic grasping. One method is planning-based grasping, where the object geometry is known beforehand and stable grasps are calculated using various algorithms. Planning-based grasping relies on simulating an object's geometry and is unable to take into account any perturbation to a static object. Another method uses vision and tactile feedback to more accurately execute a grasp. For example, stiff sensors can be placed on the front pads of robotic fingers for additional tactile information [42]. With closed-loop post-execution grasp adjustment procedures to estimate grasp stability, a support vector machine classifier has been demonstrated to distinguish stable and unstable grasps across classes of tested objects with a success rate of 81% [43]. The goal of the work presented in this chapter is to integrate sensors with existing tactile feedback grasping techniques to further improve the accuracy of the technique.

The second robotic application explored in this chapter is object imaging. An object's properties, including size and shape, are typically identified using vision. The object's material, texture, weight, and temperature are usually not needed for a robot to grasp the object. For example, Amazon warehouses augment sorting completed by human workers by having a robotic system sort objects using vision and pick up objects using vacuum technology. In non-warehouse environments, such as future Smart Home environments, an object's properties will be of increasing importance to robotic grasping techniques. Instead of implementing many cameras around a Smart Home room, our goal is to use sensors integrated onto a robot's surface to augment current robotic grasping techniques. Our secondary goal is to minimize the number and different types of sensors needed to successfully grasp an object with unknown properties a priori. The novel work presented in this chapter includes a capacitance object proximity sensor that is used as a sweep sensor to determine an object's shape using inverse problem mathematical techniques.

Within these two robotic application spaces, the fabrication processes, characterization, and integration of three types of relevant sensors are presented. In Section 2.2, a large-area flexible

piezoelectric sensor is presented using a metal electrode capacitor structure with PVDF film. The sensor is able to detect an object's time of touch on curved edges with high sensitivity and reliability. In Section 2.3, a thin-film flexible strain sensor, similar to that presented in Chapter 1, is discussed. The sensor detects an object's applied force on a robotic structure. In Section 2.4, the successful integration of the piezoelectric sensor and strain sensor is demonstrated, which allows for relative and absolute movement to be measured simultaneously. In Section 2.5, a thin-film fringing field capacitance sensor is designed to measure object proximity and time of touch. The capacitance sensor is also presented as a solution to determining object shape without requiring vision. Capacitance sweep data is used to reconstruct an object's surface profile.

3.2 Piezoelectric Sensor

Piezoelectric sensors transform mechanical stress and physical displacement into electric charge. In this work, piezoelectric sensors were designed to target large curved or edge regions on the OpenHand Model O and BarrettHand. The fabricated devices on both robotic hands are shown in Figure 3.2. The designed sensors provide time of contact detection and slip detection.

PVDF is a piezoelectric polymer used for relative movement tactile sensing [44–53]. PVDF was chosen as the substrate layer for its high d33 characteristic, inherent dipole moment, and film form factor. A metal-PVDF-metal capacitor can measure the charge generated in the PVDF when physically displaced. Several devices have been shown to use photolithographic processes to pattern micrometer-sized features of metal over large area PVDF [54, 55]. With electrodes placed in specific areas on the PVDF film, as shown in Figure 3.2, object localization can also be accomplished.

<center>(a)　　　　　　　　　　　　　　　　(b)</center>
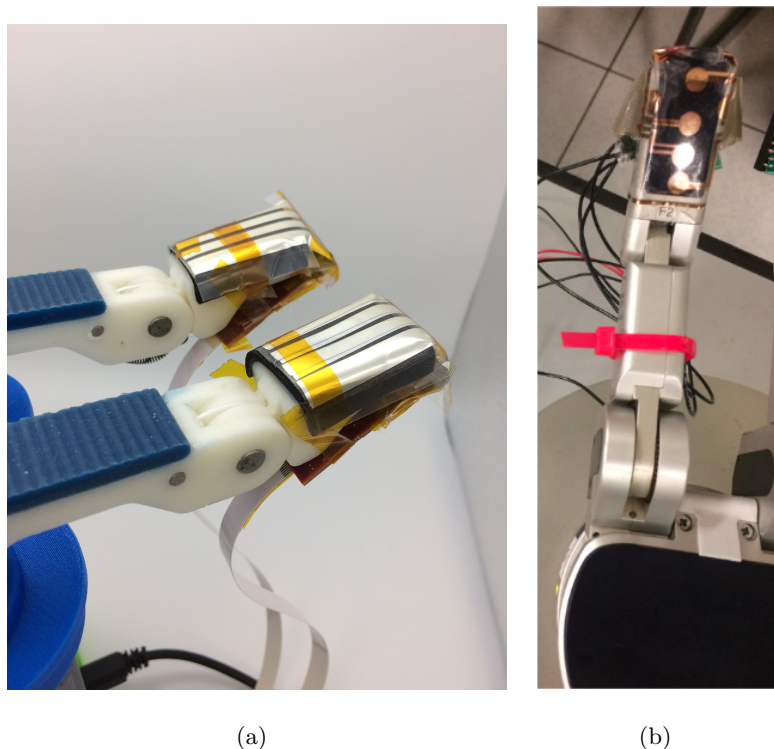
Figure 3.2: Prototype: flexible PVDF sensors placed on the OpenHand and BarrettHand.

The PVDF film used is a 52 μm-thick film from Measurement Specialties (TE Connectivity, USA). First, the film and a glass carrier wafer are cleaned by sonication in isopropyl alcohol. The film is temporarily attached to the glass using DI water. Then, aligned 100 nm-thick silver electrodes are deposited onto both sides of the film using shadow masks and thermal evaporation. For time of contact sensing, large electrodes were used: 4 cm x 0.5 cm and 4 cm x 0.25 cm.

The electrodes were connected to a custom charge readout printed circuit board (PCB) using heat seal flexible connectors, as shown in Figure 3.3. A circuit topology consisting of a charge amplifier, non-inverting amplifier, and single-pole low pass RC filter was used to convert generated charge to a conditioned and amplified voltage signal [56]. A typical impulse response is shown in Figure 3.4. When an object hits and displaces the PVDF film, a positive response is demonstrated (V_p). If the object were to remain in contact with the film, the charge dissipates. However, when the object is pulled back in an impulse fashion, a negative response can be seen (V_n). Each individual

sensor signal is multiplexed, fed through the signal conditioning circuitry, and converted using an analog-to-digital converter.

(a) (b)
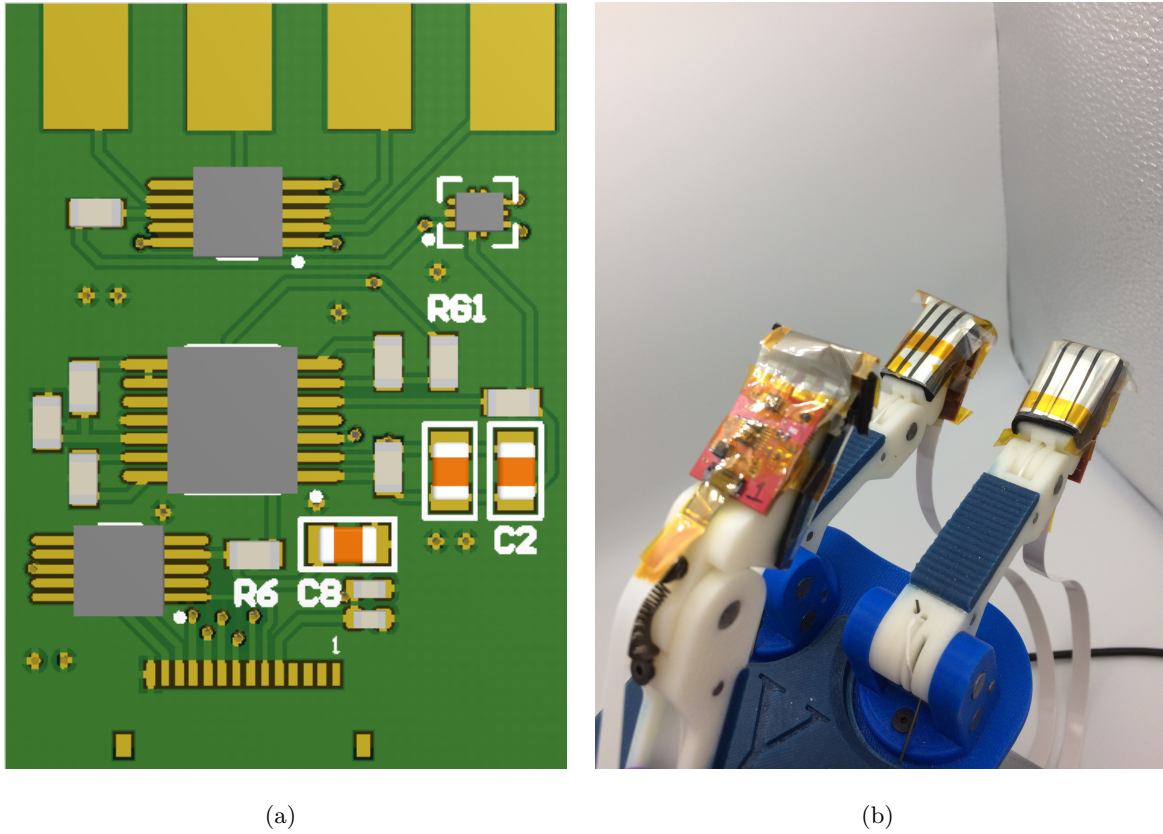
Figure 3.3: (a) Custom PCB based on [56] with heat seal connection pads and signal conditioning circuitry. (b) PVDF sensors connected to PCBs with heat seal connectors on the OpenHand.

To characterize the piezoelectric sensor, an Admet force testing machine (eXpert 5600, ADMET Inc.) was used to provide various controlled amounts of force to the sensor. The voltage amplitude is not necessary information for this particular application; however, the amplitude dependence on applied force - or distance of displacement - is shown in Figure 3.5 and can be used to correlate relative amounts of applied force.
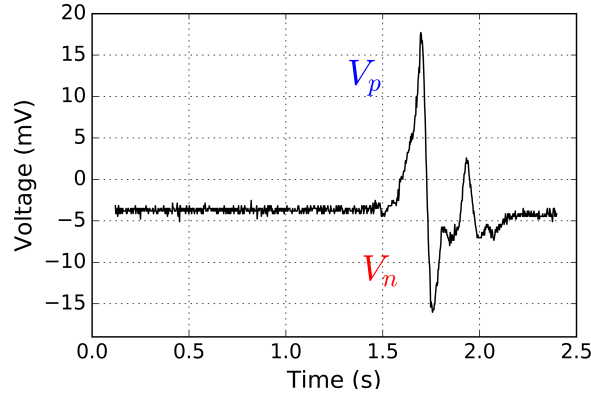
Figure 3.4: PVDF response to an impulse force.
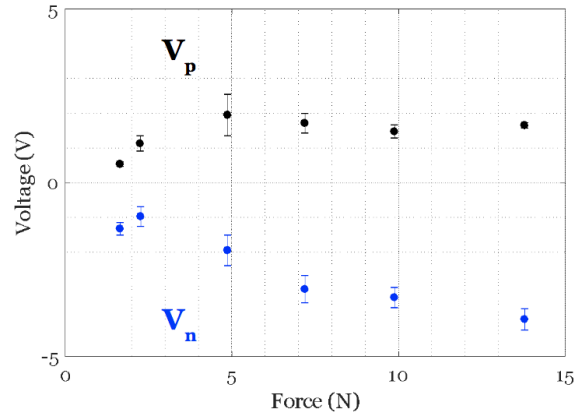
Figure 3.5: PVDF maximum response to varying amounts of force.

Because the piezoelectric sensor output corresponds to the amount of physical displacement of the piezoelectric film and robotic structures are typically hard, compliant layers were tested to increase the sensitivity of the device. Various compliant layers were tested (Table 3.1). Polyurethane open-cell foam with a high pressure-to-25%-compression was found to increase the device sensitivity the greatest; with 0.5 N of applied force, the voltage output was 6.7 times greater than the non-compliant backings (Figure 3.6).

Foam	Compliant Layer	Cell Type	Thickness (mm)	Pressure to Compress 25% (psi)
1	Polyurethane Foam	Open	0.734	45
2	Silicone Foam	Closed	0.810	10
3	Neoprene Foam	Closed	1.59	7
4	Silicone Foam	Open	1.59	3

Table 3.1: Tested foam characteristics.
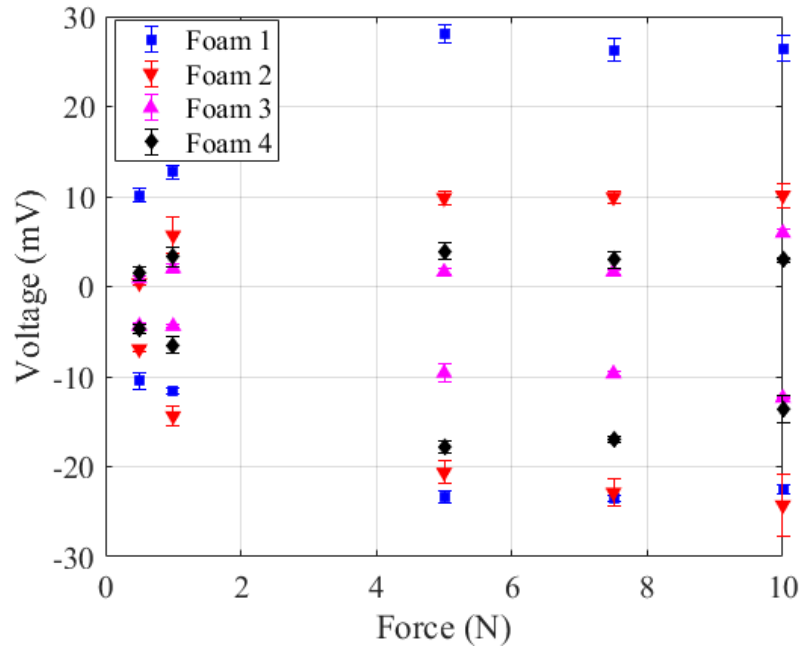
Figure 3.6: Positive and negative peaks of PVDF sensor voltage output for various foams. Foams listed correspond to those in Table 3.1.

The sensor-circuit integration presented here sets the example for how the flexible sensors in this thesis are integrated with small form factor PCBs. For connecting metal deposited on polymers, heat seal connectors are used for maximum bending. For connecting each sensor's PCB to a central read-out PCB, ZIF cables are used because of the need to isolate and stabilize long distances of wire.

3.3 Strain Gauges

Strain gauges on soft elastomers have been designed for monitoring bending in wearable electronic skin applications [34, 35, 57–59]. Typical body parts that are of interest include knee and elbow bending, wrist movement, and organ contraction. In addition to bending, strain sensors have been used as pressure sensors using capacitive sensing modes independent of strain sensing modes as well as material structural change [36, 60]. Common flexible strain gauge materials include thin film metals and piezoelectric semiconductor materials. When high gauge factors are needed, piezoelectric integrated with transistor arrays can be used [37, 61, 62].

For strain gauges implemented in scalable robotic designs, specific scalable processes are required and the material and fabrication choices need to be tailored to existing vendors and fabrication facilities. Thin film metal was chosen for this project because of its linear properties and ease of fabrication. After fabrication, the strain gauges were tested to correlate an object's applied force on the sensor with changes in sensor's resistance.

3.3.1 Methods

The strain gauge design is serpentine structured to provide for a maximum base resistance in a small surface area and a relatively small square compared to robotic structures for applied force object localization. For example, a silver trace width of 60 μm, trace pitch of 120 μm and total length of 10 mm leads to a base resistance of 8.6 kΩ. The strain gauge also has large contact pads for stable bonding to a heat seal flexible connector, as shown in Figure 3.7.
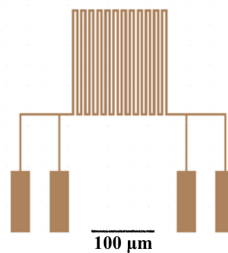
Figure 3.7: Strain gauge design.

The process flow is similar to that presented in Chapter 1 (Figure 2.3). A glass carrier wafer is cleaned and silanized. PDMS is spin-coated on the wafer, parylene is deposited as an adhesion layer, and metal is deposited using e-beam evaporation and patterned using photolithography.

(a) Arcs of varying radii.   (b) Strain gauge strained on arc.
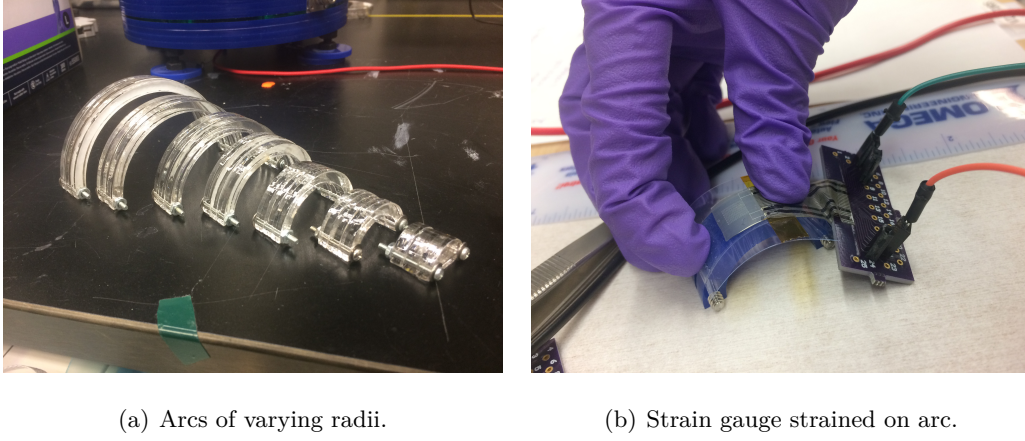
Figure 3.8: Strain gauge characterization setup.

3.3.2   Results

To calculate the gauge factor of the strain gauge sensor, the sensor is peeled off the carrier wafer and placed onto double stick tape on a thin plastic layer. The layered stack is then placed on acrylic arcs of various radii, as shown in Figure 3.8(b). The gauge factor of the device is found using Equations 3.1 and 3.2. Applied force of an object edge will bend the sensor; this bending is then measured by the change in resistance of the strain gauge. The gauge factor of strain gauge was calculated to be 2.83.

$$GaugeFactor = \epsilon \frac{\Delta R}{R} \tag{3.1}$$

$$\epsilon = \frac{t}{2r} \tag{3.2}$$

where ΔR is the change in resistance from applied strain, R is the base resistance of the strain gauge, t is the thickness of the entire device (including metal, substrate material, and plastic backing), and r is the bending radius that provides strain to the device.

3.4   Piezoelectric and Strain Sensor Integration

Measuring two sensing modes simultaneously was explored. For applied strain and time of touch, the strain sensor and piezoelectric sensor can be integrated into one material layer and two patterned metal layers. This integration would allow for a robot to determine when an object touches and how much pressure the object places on the robot simultaneously with minimal sensor fabrication steps.

3.4.1   Design

The strain gauge is patterned on one side of the PVDF film. The strain gauge is also used as one electrode for the piezoelectric sensor. The second electrode for the piezoelectric sensor is placed on the other side of the PVDF film. The design is shown in Figure 3.9. The strain gauge has a trace width of 20 μm and metal thicknesses of 40 nm / 120 nm of Cr / Au. To fabricate this device, metalized poled PVDF film was purchased (Precision Acoustics, UK). The strain gauge and electrode was patterned by patterning both layers within the same fabrication step (Figure 3.10). First, photoresist is spin-coated and baked on one side of the PVDF film. The same process is then completed for the other side of the film. Then, each side is exposed sequentially. The developing and etching steps use wet processes so both sides are developed simultaneously (AZ300MIF, Integrated Micro Materials) and etched simultaneously (Gold TFA, Transene).

Bottom electrode on back layer of PVDF

Strain gauge on top layer of PVDF

250μm
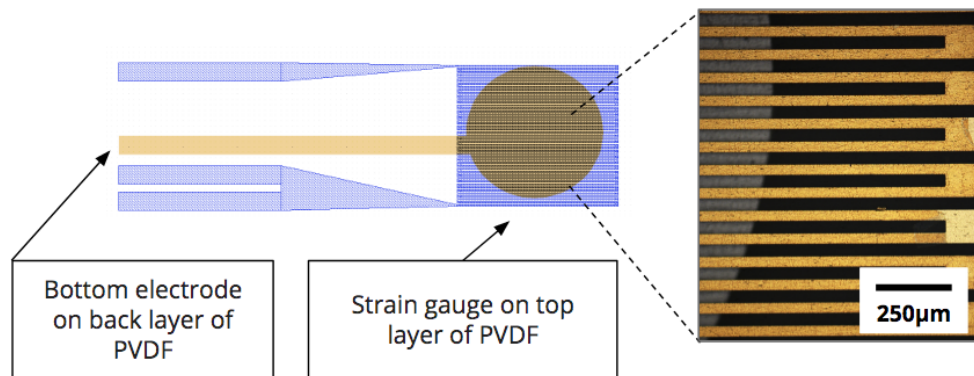
Figure 3.9: Integrated strain gauge and piezoelectric sensor.
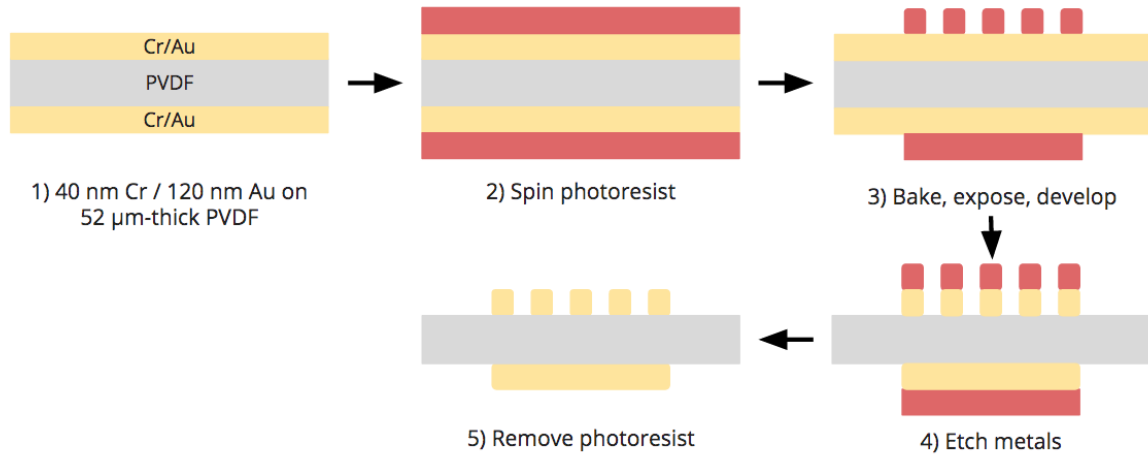
Figure 3.10: Integrated strain gauge and piezoelectric sensor process flow.

3.4.2 Characterization

The integrated sensor was characterized using methods presented in earlier sections: a force testing machine was used to apply force and the sensor was bent over arcs of various radii to provide strain. The voltage response of the piezoelectric sensor using the strain gauge as one of the electrodes is shown in Figure 3.11. The sensor behavior mimics that of the piezoelectric sensor with two circular electrodes (Section 3.2). Because the PVDF film is stiffer than PDMS, the linearity of the strain sensor is higher than the strain gauge patterned on PDMS. The trade-off of the sensor is its gauge factor, which is 1.24. This means that more bending is needed to provide the same amount of strain compared to the strain sensor fabricated on the PDMS substrate. The gauge factor characterization results are shown in Figure 3.12.
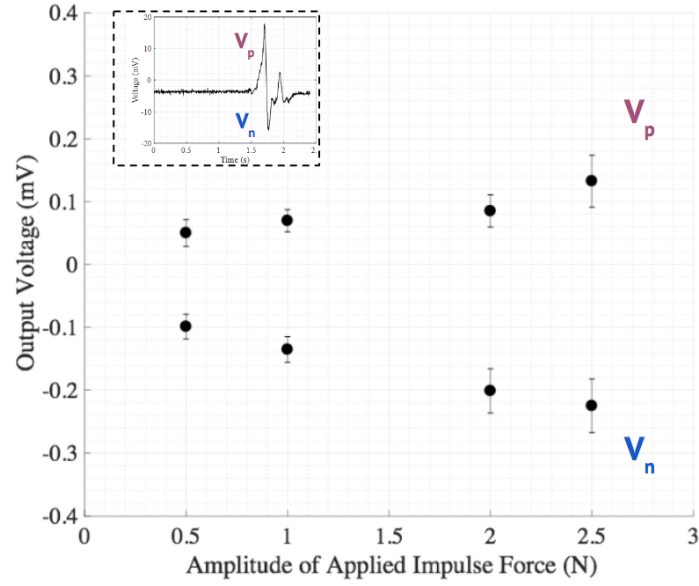
Figure 3.11: The voltage response of the piezoelectric sensor with respect to applied force using the integrated strain gauge and piezoelectric sensor design.
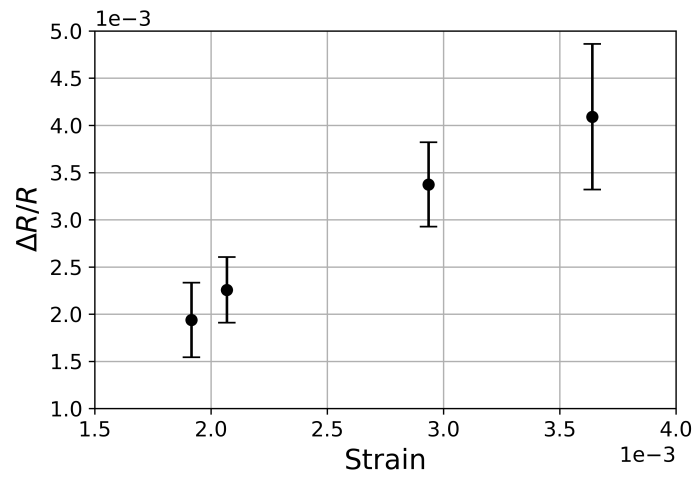
Figure 3.12: Strain gauge on PVDF has a gauge factor of 1.24.

3.5 Capacitive Proximity Sensing

Capacitive sensing can be used to measure an object's distance, or proximity, to the sensor. This sensing mode is widely present in smartphone touch screens and tablet stylus technology. In this mode, finger or stylus proximity is used for localization and touch on/off measurements.

For applications where the object proximity is needed more than a few millimeters above a flat plane, capacitive sensing can also be used. In this case, changes in the fringing electric field are measured. For example, when an object whose dielectric constant is greater than air moves in relation to metal electrodes, measuring the change in the fringing field, or capacitance of the entire system, provides information on how close the object is relative to the sensor. Various designs and systems of proximity sensing using flexible substrates have been demonstrated [**14**, **15**, **16**, **17**, 63–67]. Non-flexible capacitive proximity sensors have also been demonstrated [**13**, 68, 69]. For this type of of proximity sensing, other possible sensing methods include using ultrasound and time of flight measurements [68, 70–72].

For robotics, capacitive sensors have been demonstrated for collecting grasping information. Tavakoli et al. (2017) has shown soft matter capacitive sensors for pre-touch robotic grasping information. Conductive objects were sensed by monitoring changes in electric field while non-conductive objects were sensed using deforming capacitive electrodes [73]. Xia et al. (2018) demonstrated a capacitive sensing electrode matrix on a PCB to track vertical and lateral motion. The system is also able to perform surface profile recognition of metallic objects [74]. Finally, Ding et al. (2018) demonstrated object proximity detection using capacitive sensors and object material detection with off-the-shelf time of flight sensors [75].

In addition to determining an object's proximity to a robot, tomographic techniques combined with robotic structures would allow for an object's shape to be determined without requiring robotic vision techniques. Capacitance tomography is a common technique for object shape reconstruction and identification in oil/gas and medical industries [76–78]. In addition to advances in capacitive systems, many algorithms have been devised to optimize the reconstruction of an object's shape with capacitance data [79–83]. Within each tomographic system there is an forward or inverse

problem being solved; where a forward problem uses an object's characteristics to determine its effects on a system whereas an inverse problem uses generated data to determine what object caused the data.

There have been previous demonstrations of using capacitive sensors for surface profile detection in robotic environments [84–86]. Campi et al. (2016) demonstrated a 4 by 4 capacitor sensor matrix that classified object surface profiles using a support vector machine (SVM) algorithm up to 20 cm away with over 90% accuracy. Runtime matrix reconfiguration was implemented using switch arrays. A subsequent evaluation calculated SVM classification accuracy with various algorithm parameters of 74.67 - 90.33 %. Physically, the sensor matrix is quite large; the goal of the following work is to reduce the size of the sensor but maintain the same ability to sweep past an object to detect an object's surface profile.

Within this context, a capacitive sensor was designed and used to sweep past objects to determine the object's shape. The goal of designing such a sensor and system is to enable a robot to determine an unknown object's shape in an unknown environment without requiring vision. In this section, the capacitive sensor's design is discussed, the solutions to the inverse problem are presented, and experimental results are presented.

3.5.1 Methods

The first proof-of-concept object proximity capacitance sensor designed is shown in Figure 3.13. Silver was thermally evaporated through a shadow mask onto a layer of PDMS. The ground loop is left floating and the signal loop is connected to a capacitance-to-voltage circuit. The relation between capacitance and object distance is shown in Figure 3.14.

For the remainder of the section, a rigid metal capacitive proximity sensor on PCB is used for characterization and experiments. The second use case of the capacitance sensor is determining an object's shape using a combination of inverse problems and tomography. As mentioned previously, electric field tomography has been used to predict the placement of liquid or solid and typically requires sensors concentrically surrounding the object [76–78]. Capacitance sensors have also been

used to detect object proximity and object material [**14**, **15**, **16**, **17**, 63–72, 87]. These types of sensor configurations are useful if the object is a movable target while the sensor is stabilized. In robotics, a single or plane of sensors would be placed on a moving robotic structure.
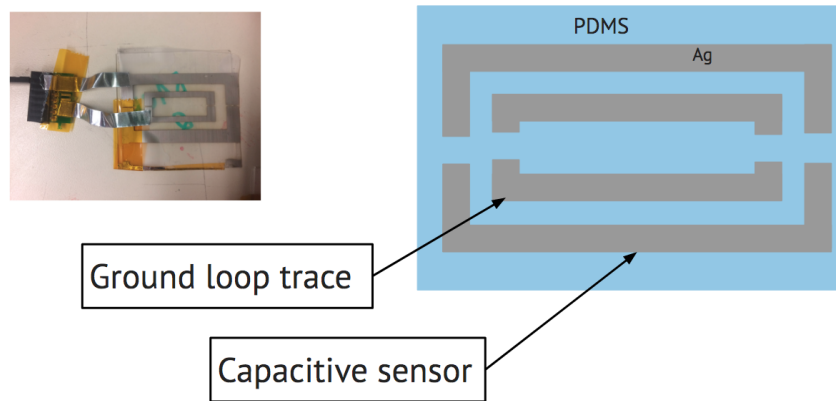
Figure 3.13: Prototype capacitance sensor design.
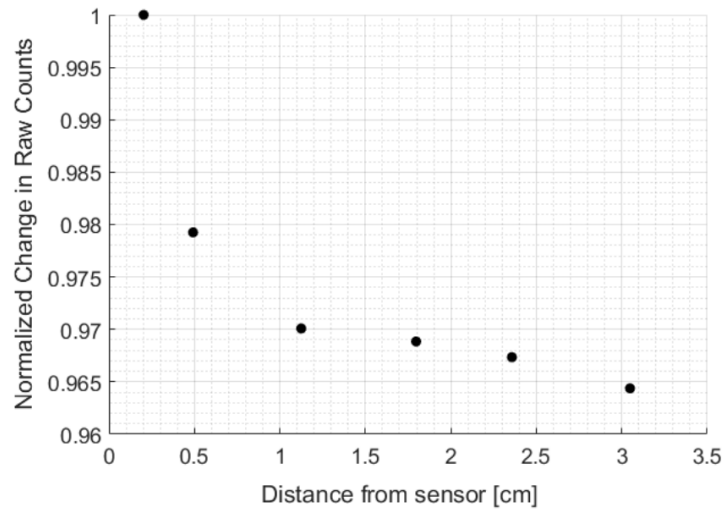
Figure 3.14: Decrease in capacitance with increasing distance between the sensor and object.

The forward problem is to compute an object's capacitance when swept past a capacitive sensor when the object's shape is known. The inverse problem is to reconstruct an object's shape given its capacitance data from sweeping a capacitance sensor past the object. Solutions to both the forward and inverse problem are conducted to verify the accuracy of the inverse problem solver.

Then, the reconstruction results are compared to a classifier's results to compare compute time, accuracy, and success rate.

The forward problem is solved by using the system shown in Figure 3.16. A two-electrode capacitance sensor was used. The sensor consists of copper electrodes on a custom PCB with a capacitance to digital converter (FDC1004, Texas Instruments) and peripheral components. The capacitance to digital converter custom PCB is shown in Figure 3.15.

(a) Block diagram.   (b) PCB.
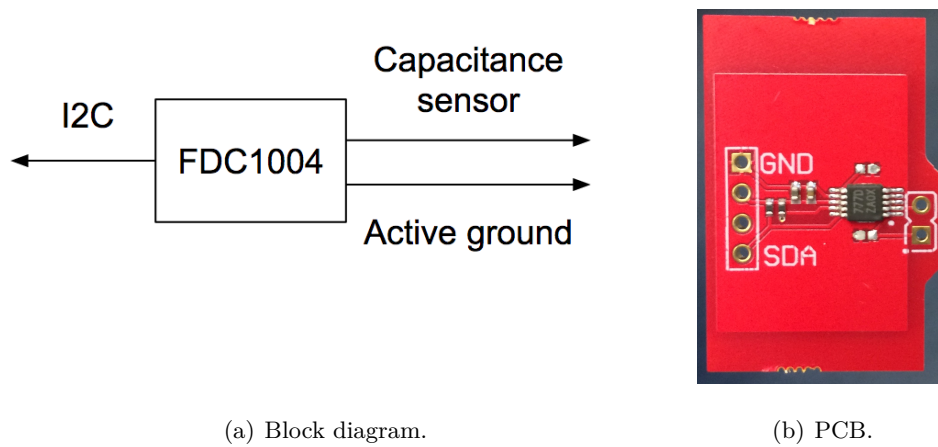
Figure 3.15: Custom PCB for capacitance to digital conversion.

One electrode is connected to the sense node and the other electrode is connected to an active ground node. To set up the forward problem, the shape of the object is known as function, S. This function is the input to a numerical solver, which then calculates the capacitance of the object using Maxwell's equations. The numerical solver's capacitance output is then compared to the capacitance data from the sensor found by sweeping the sensor past the object (Figure 3.16). An example sweep result is shown in Figure 3.19.
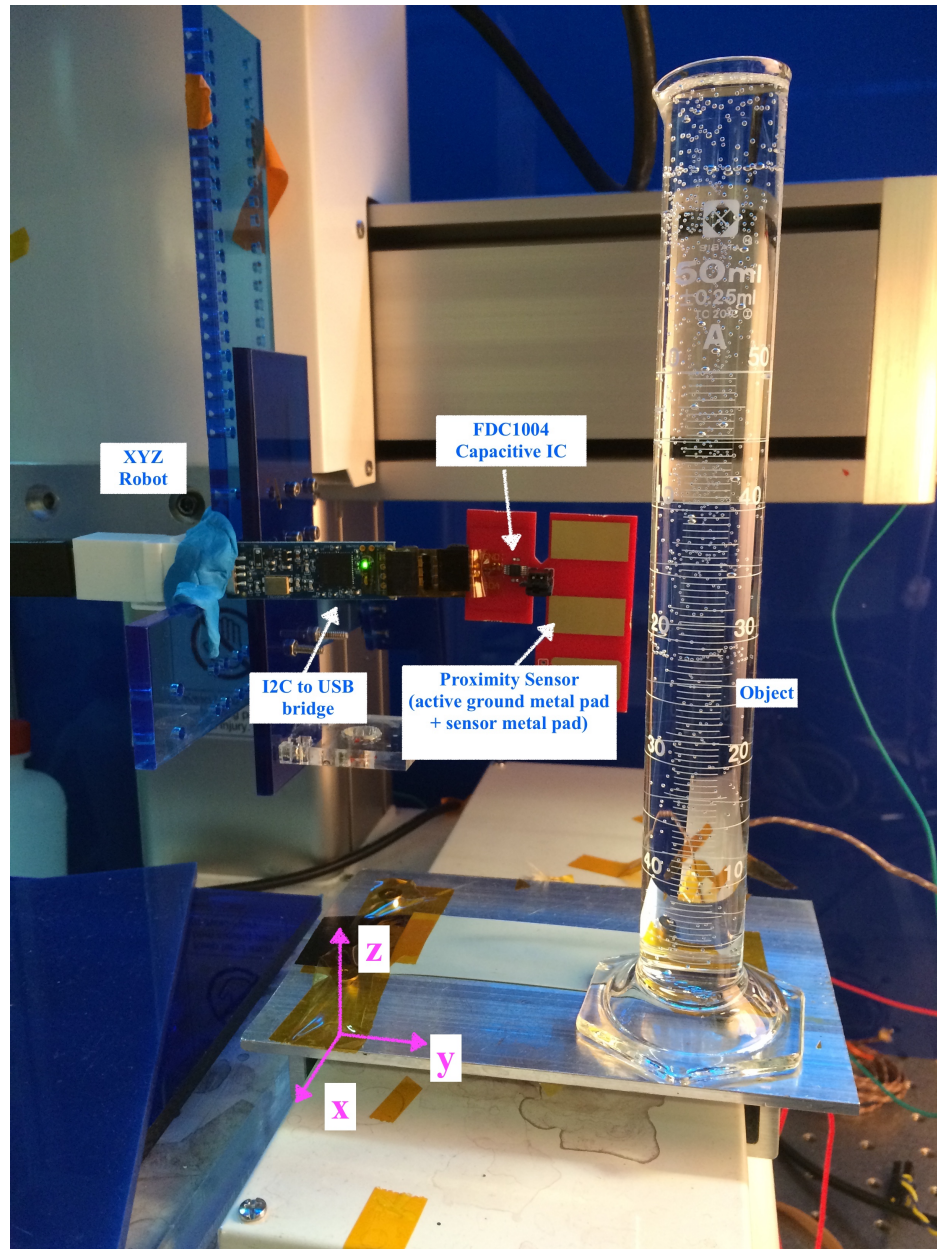
Figure 3.16: Capacitance proximity setup.
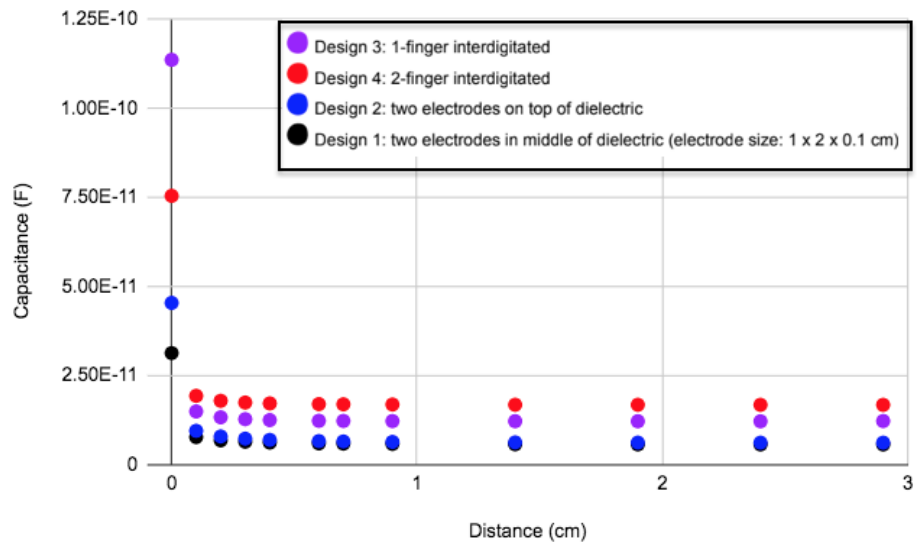
Figure 3.17: COMSOL simulation results for various sensor designs.
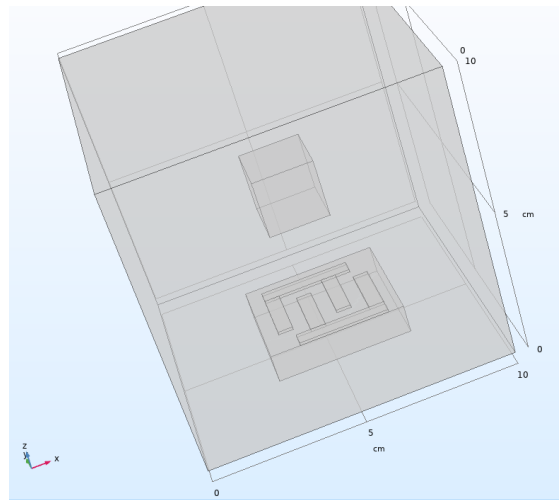
Figure 3.18: Screenshot of COMSOL simulation of two interdigitated finger design. Credit: Vikrant Kumar.
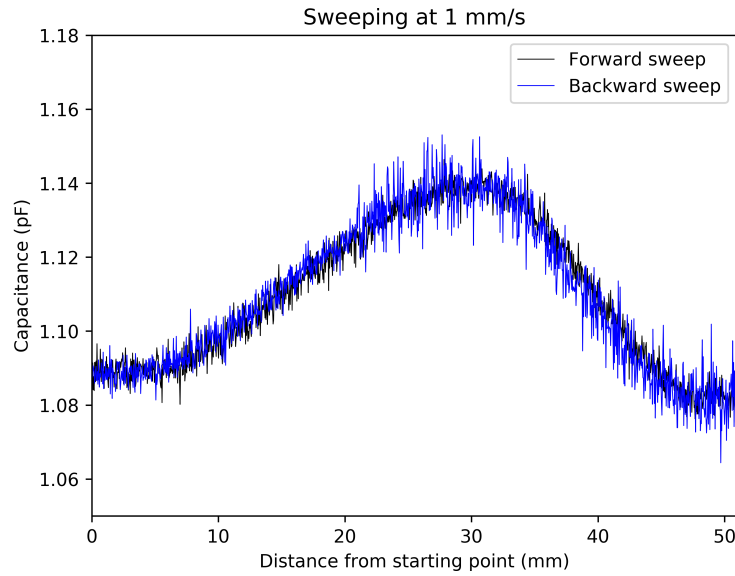
Figure 3.19: Capacitance data from sweeping the sensor past the object in both directions at a normal distance of 30 mm.

To optimize the sensor design without adding too much complexity, various sensor configurations were simulated using COMSOL to optimize the fringing electric field. The simulation results are shown in Figure 3.17. The sensor design chosen for the remainder of the sweep experiments consists of two interdigitated fingers, as shown in Figure 3.18. The interdigitated finger proximity sensor PCB is shown in Figure 3.20. The revised sensor was swept past various objects of similar shape. Object dimensions are listed in Table 3.2.

Given the capacitance measured when sweeping the sensor past an object, inverse tomography techniques, such as reconstruction, can be used to determine the object's shape that caused the

Object	Dimension	Material
Cylinder	1" diameter × 2" height	hollow plastic jar
Cylinder	1" diameter × 2" height	water-filled plastic jar
Cylinder	1.5" diameter × 1" height	hollow tin can

Table 3.2: Objects for capacitive proximity sweeping experiment.
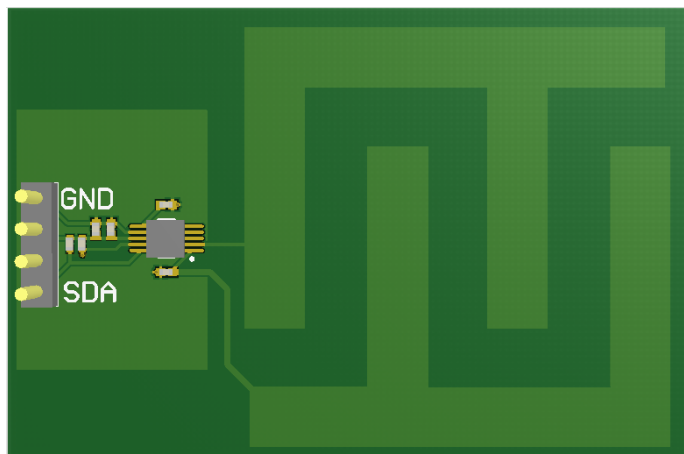
Figure 3.20: Custom PCB with interdigitated capacitive proximity sensor used for sweep experiment. Length of PCB is 5.6 cm.
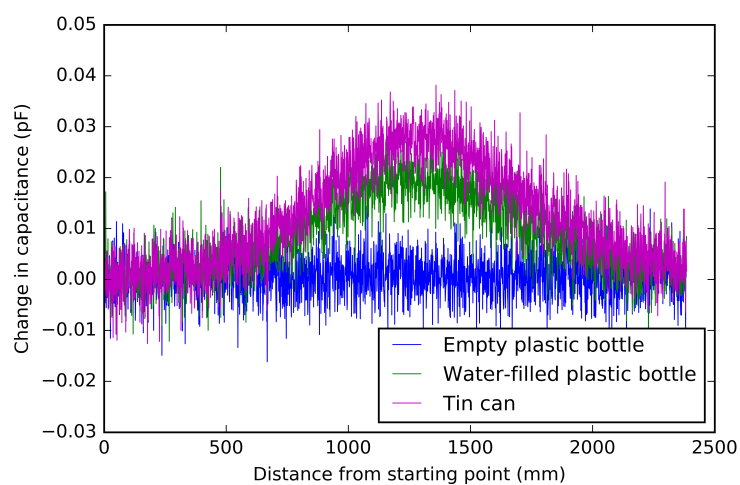
Figure 3.21: Normalized capacitance data from sweeping the sensor past three various objects at a normal distance of 20 mm.

capacitive response. The mathematical model used for reconstruction is that introduced in [88]. By linearizing the inverse problem and solving the linear equations of basis functions and data points from the capacitance sensor when sweeping past an object, the object shape can be reconstructed. The aim of this exploratory experiment was to develop a method that takes less computational power and is faster than previously developed methods that use classifier techniques [84, 85].

3.5.2   Conclusion

This chapter combines fabrication techniques developed in Chapter 1 and small form-factor custom PCBs to enable multi-modal robotic sensing. The goal of integrating tactile sensing with robotic tasks is to determine the strengths and limitations of flexible sensors with rigid robots. One important lesson learned from these experiments is that a thin but compliant layer provides higher sensitivity for pressure-based sensing. Another lesson was learned by following the evolution of object detection from pressure sensing to non-contact capacitive sensing to non-contact optical sensing. The latter sensing solution provides higher resolution and more robust sensing.

The combination of piezoelectric and strain sensing modes allows a robot to sense time of touch and an object's applied force simultaneously. As presented in this chapter, it was found that the piezoelectric sensor's response did not suffer from having a high resistance strain gauge as one of the electrode pads. However, the sensitivity and durability of the strain gauge on a PVDF substrate worsened. Because this combination of sensing modes was motivated by previous work with actuated robotic fingers, a path of exploration is to combine higher sensitivity modes (piezoelectric and capacitive sensing modes) for underactuated robotic fingers. Applied pressure sensing is not needed to successfully grasp objects using underactuated hands; the combination of piezoelectric and capacitive sensing modes allows for object proximity and time of touch to be measured. This way, the durability of a soft elastomer or strained metal trace does not need to be main limiting feature of a tactile sensing solution.

Lastly, using a capacitance sensor for object tomography opens new avenues for object detection in unknown environments. With the combination of a time-of-flight sensor instead of a capacitive

sensor and ultrasound sensor, robotic hands can transform into low power, fast, and low cost grippers. A future task that is most exciting about integrating tactile sensing with robotic structures is to apply classification techniques to train tactile data for object recognition.

The end goal of the tactile sensor exploration performed within these experiments is to augment existing robotic grasping techniques. If these similarly designed sensors are to be commercially available on industrial Smart Home robots, for example, there would be a need to reduce the cost of fabrication by incorporating either large-area metal patterning or CMOS technology. The main advantage of integrating flexible tactile sensors onto a rigid robotic structure is that the complexity of the active circuitry is minimal compared to other solutions presented in the field. Several interesting projects that are past the scope of this thesis include flexible sensors for slip detection, texture detection, and kHz or faster sensor readout.

Chapter 4

Flexible Electrode Array for Stimulating Electric Fish Electroreceptors[1]

4.1 Motivation

In this chapter, a flexible stimulation array, as opposed to a flexible sensor, is explored. The main distinction between a stimulation and sensory array is that the stimulation's absolute value and direct addressing component is critical to uniformly and quickly stimulate desired areas. Typically, sensor arrays are used to compare time lapses, or relative changes, of electrical activity.

The specific motivation for designing a flexible stimulation array stems from the need for neuroscientists to control the sensory inputs to animals so that the mapping between external commands and neural circuits can be better understood. The Sawtell group at Columbia University's Zuckerman Institute Mind Behavior and Body Institute studies active sensory processing in electric fish. Previous work has been done to study how motor signals influence sensor processing [89–91]. In order to understand the first stage of sensory processing in the electric fish brain, an improved

---

[1]Based on C. Yu, C.K. McGinn, K. Perks, S. M. Thompson, N. Sawtell, and I. Kymissis, *Dense Conformal Electrode Array for Electric Fish Electroreceptor Stimulation*, Advanced Materials Technologies, *In Preparation.*

method is needed to drive individual electroreceptors along the fish's skin in a natural setting. An image of the fish under study is shown in Figure 4.1.
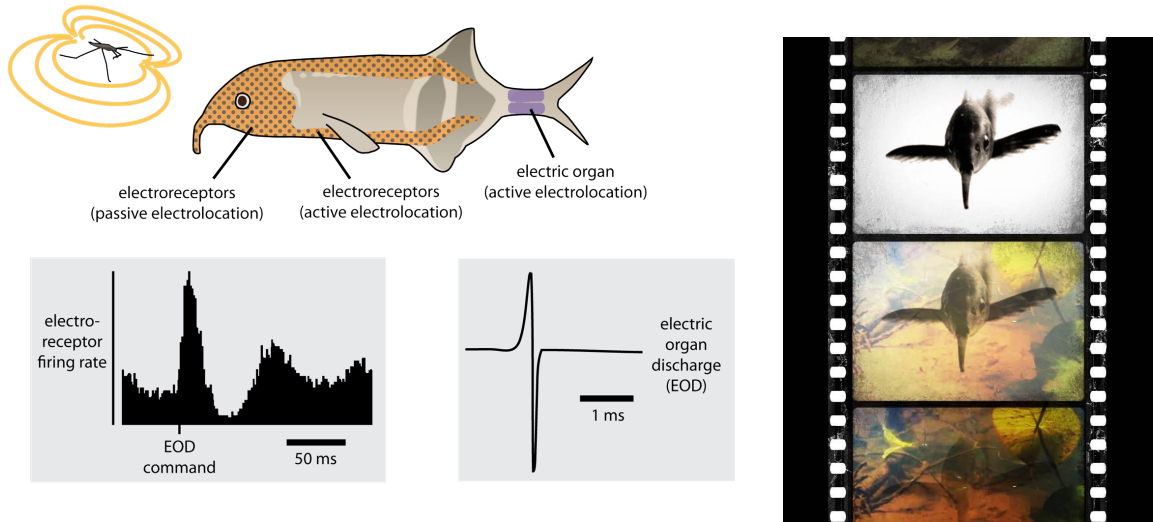
(a) The electric organ generates a brief pulse of electricity known as an electric organ discharge (EOD). Receptors sense voltage across the skin.

(b) Negative images in mormyrid fish.

Figure 4.1: The electrosensory system of mormyrid fish. Taken from [92].

Weakly electric fish, specifically *Gnathonemus petersii*, have two naturally occurring features that allow for a promising outlook on the sensory consequences of motor commands: relatively large electroreceptors that measure changes in electric field, and hypertrophied cerebellum that make it easier to generate experiments to predict sensory consequences of motor commands. The goal of this project is to fabricate an electrode array that mimics the size and pattern of the electroreceptors using microfabrication techniques so that the correlation between the electrode stimulations and motor commands can be studied. The measurement of motor commands in the fish's brain is already well established.

The electroreceptors of *Gnathonemus petersii* are about 100 microns in diameter and follow a 1 mm hexagonal spacing pattern. The fish's surface is curved, relatively rough, and has a high surface energy. These properties provided design specifications for the electrode array.

The general layer stack of the electrode array is based on previous demonstrations of flexible elec-

trode arrays [93–95]. In particular, Jeong et al. (2016) demonstrated improvements in impedance stability, stretchability, and water absorption rate by using a parylene-caulked polydimethylsiloxane (PDMS) substrate for neural electrodes [93]. Meacham et al. (2007) demonstrated two rows of gold electrodes with a PDMS substrate and a PDMS encapsulation layer. An aluminum mask was used to etch the PDMS encapsulation layer [94]. Viventi at al. (2011) demonstrated an actively multiplexed, highly-dense electrode array for mapping in vivo brain activity using flexible silicon electronic technology [95]. The characteristics adopted from these various designs include parylene-caulked PDMS, an aluminum metal mask to etch parylene, and the exploration of electrode metals. In addition to array fabrication optimization, it is critical that the array is stable and weakly bonded to the surface when placed on the electric fish. Stable surface modifications for silicone and polymer materials were investigated to optimize surface interfaces between arrays and biological tissues [96].

Lastly, a driving circuit was designed to enable system usability and the ability to independently control the timing and amplitude of the current provided at each electroreceptor on the fish's skin. The electrode array and system presented below combine the advantages of fabricating metal electrodes on thin silicone membranes and chemical surface modifications to successfully investigate the encoding of electroreceptor-driven time-dependent action potentials in the first central processing stage of mormyrid fish *Gnathonemus petersii*.

4.2 Methods

4.2.1 Fabrication

Electroreceptor stimulation is provided by an electrode array whose flexible substrate conforms to the curvature of the mormyrid fish's skin. Polydimethylsiloxane (PDMS) is used as the substrate of the array because it is flexible at low thicknesses but physically robust so that the arary can be used for multiple recording sessions. The array of electrodes consists of a hexagonal pattern containing 99 square chrome/gold electrodes with a side length of 250 μm and diagonal spacing of 1 mm. This pattern was designed to be evenly distributed across the electroreceptor area with

a higher spatial frequency than the electroreceptors to achieve isolated stimulation of individual receptors, as shown in Figure 4.2 and Figure 4.5.
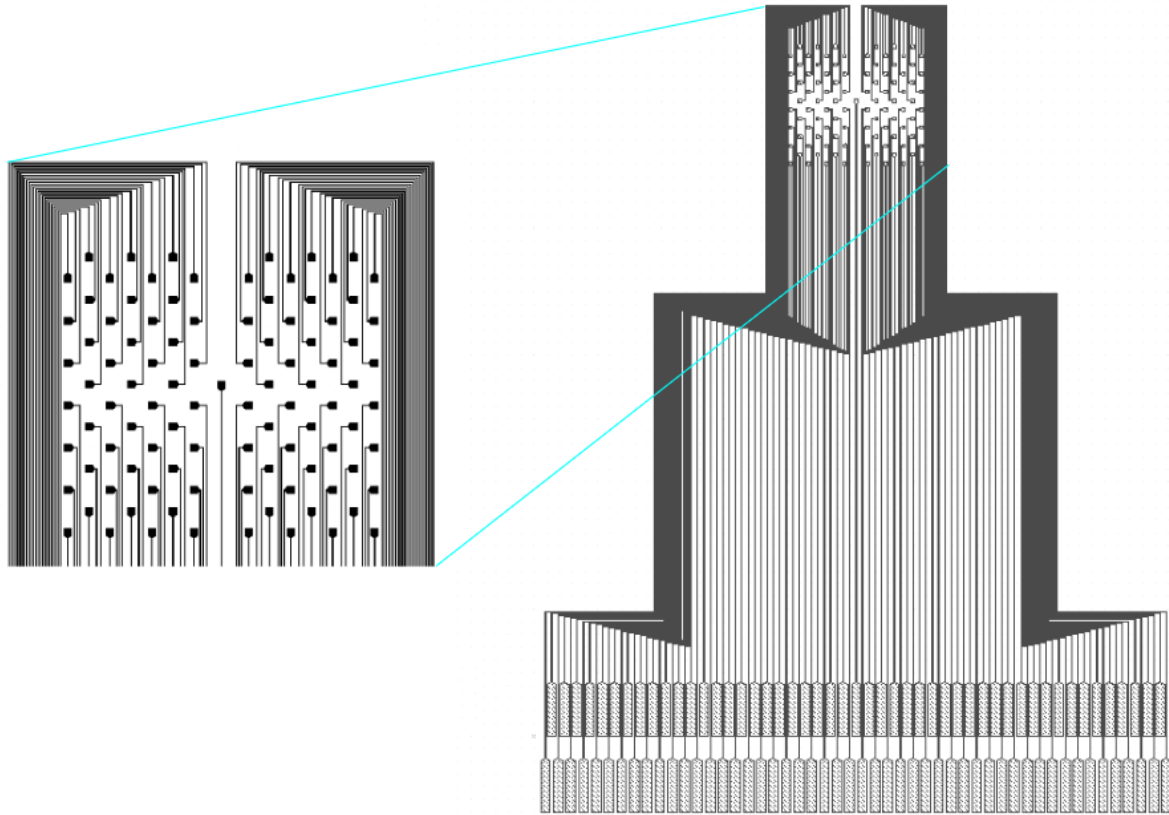
Figure 4.2: Electrode array design.

The fabrication process flow is shown in Figure 4.3. For ease of handling during the fabrication process, a 100 mm diameter glass wafer is used as the carrier wafer. The glass is first cleaned by sonication in 10% Micro 90, acetone, then isopropyl alcohol. The surface is then silanized with trichloro(1H,1H,2H,2H-perfluorooctyl)silane by vacuum vaporization to ensure easy removal of the PDMS during post-processing. PDMS (10:1) is mixed, dessicated, then spun onto the glass substrate at 900 rpm for 45 seconds. The spin-coated PDMS is desiccated again to ensure that air bubbles have been removed before high vacuum evaporation. The PDMS is then cured in an oven at 125°C for 20 minutes. 3 μm of parylene-C is chemically vapor deposited on top of the
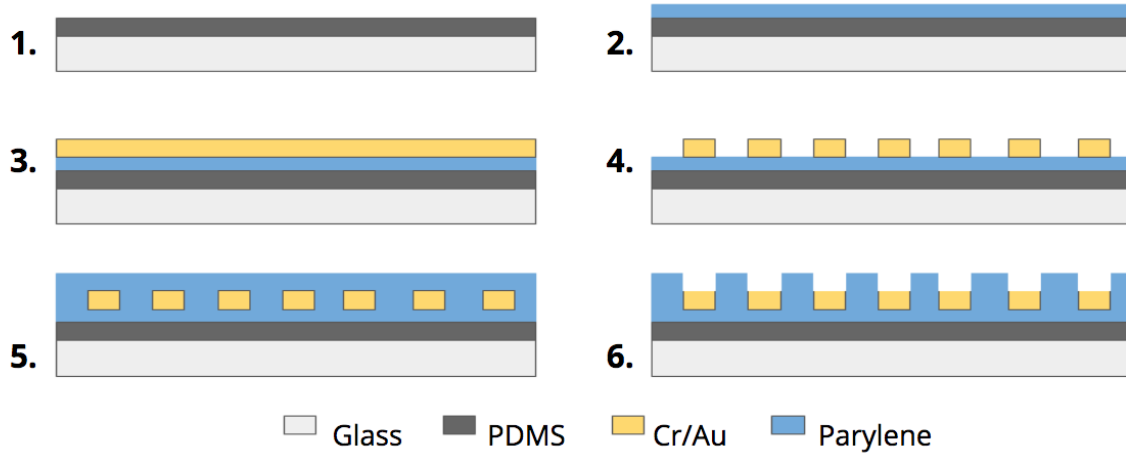
Figure 4.3: Fabrication process flow.

PDMS to promote metal adhesion. Chrome (40 nm) / gold (120 nm) is then deposited by e-beam evaporation. The metal layers are photolithographically patterned using S1811 photoresist to the desired electrode pattern before developing (AZ300MIF, IMM)) and wet etching (Gold Etch TFA and Chromium Etchant Type A, Transene). After the photoresist has been stripped, a second 3 μm-thick parylene-C layer is deposited to encapsulate the electrode traces. Aluminum (100 nm) is thermally evaporated and photolithographically patterned to act as an etch mask before oxygen-etching the parylene-C encapsulation layer. The parylene encapsulation layer patterned on the metal electrodes is shown in Figure 4.4.

Finally, the electrode array connection pads are heat sealed (Elform, NV) to a printed circuit board before the electrode array is peeled from the glass substrate. The complete electrode array placed on the fish can be seen in Figure 4.6.
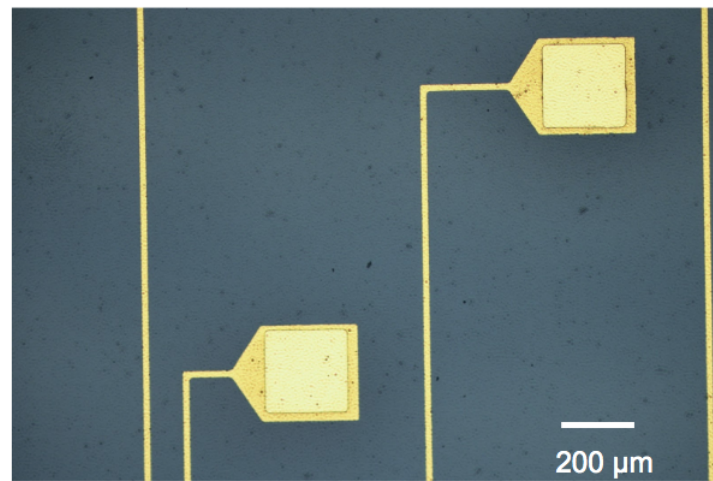
Figure 4.4: Parylene encapuslation layer on metal electrodes.

Figure 4.6: Zoomed out view of the electrode array placed on the fish. The neurophysiological recording setup can be seen on the left.
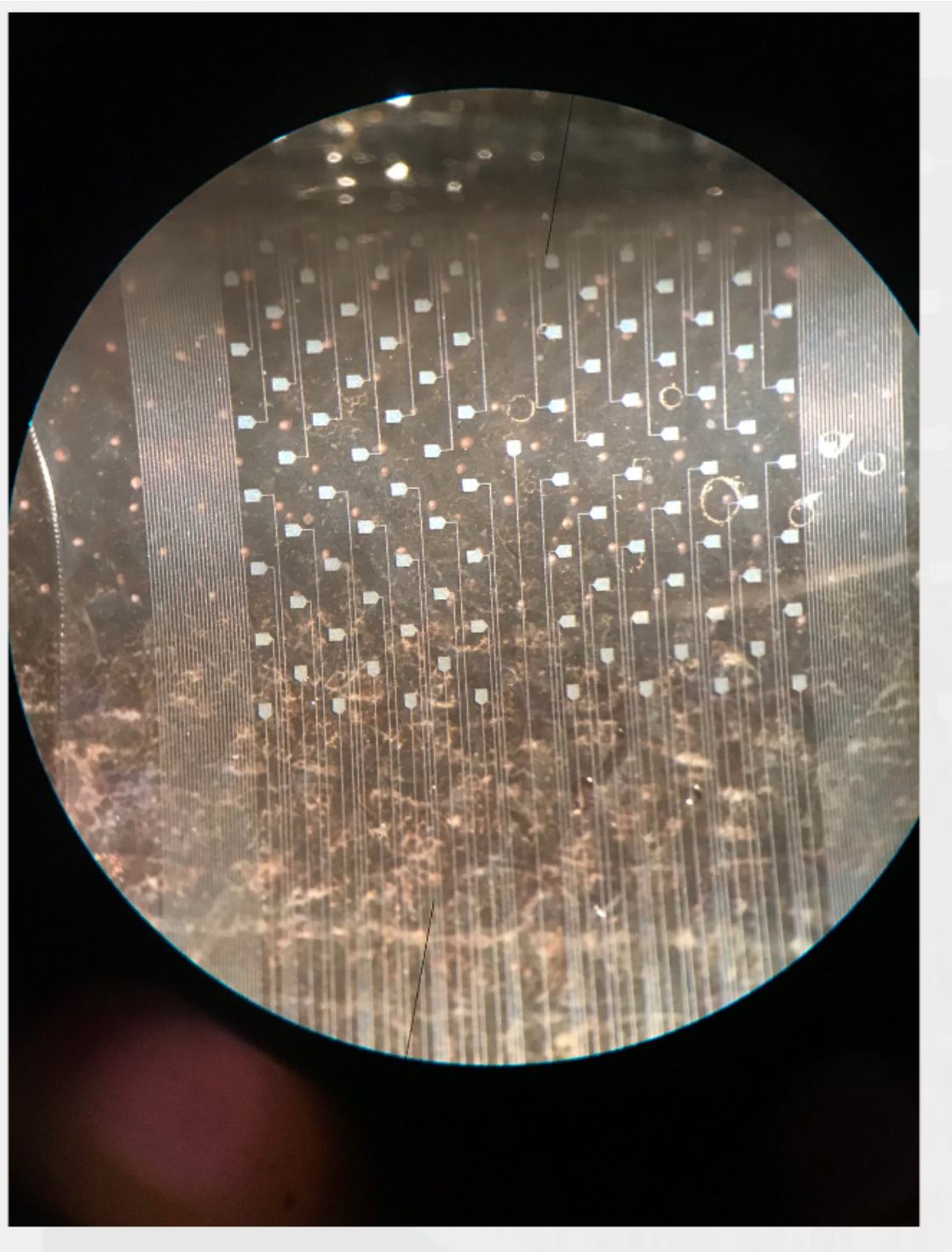
Figure 4.5: Electrode array on fish. The electroreceptor pattern is visible beneath the array.

4.2.2 Surface characterization and modification

To have weak bonding between the array and the fish skin, contact angle measurements were performed on mormyrid fish skin, parylene, and thin-film gold on parylene/PDMS to calculate the surface energy of each surface. The surface energy is calculated using the Owens/Wendt theory, which is a two parameter model. A solid's surface energy is comprised of a dispersive and polar component (Good's equation and Young's equation) [97]. The dispersive component contains van der Waals and other non-site specific interactions between a solid and a liquid. The polar component contains dipole-dipole, dipole-induced dipole, hydrogen bonding, and other site-specific interactions between a solid and a liquid. By using two or more liquids that have known dispersive and polar components to conduct contact angle measurements, the dispersive and polar components of the solid in question can be found. The equation governing this theory is shown in Equation 4.1.

$$\frac{\sigma_L(\cos\theta_i + 1)}{2} = \sqrt{\sigma_S^P}\sqrt{\sigma_L^P} + \sqrt{\sigma_S^D}\sqrt{\sigma_L^D} \tag{4.1}$$

where σ_L is the total surface energy of the liquid, θ_i is the contact angle of the liquid when placed on the solid, σ_S^P is the solid's polar surface energy component, σ_L^P is the liquid's polar surface energy component, σ_S^D is the solid's dispersive surface energy component, and σ_L^D is the liquid's dispersive surface energy component. The liquids used for contact angle measurements were DI water and diiodomethane. Diiodomethane is a non-polar liquid, such that $\sigma_L^P = 0$ and $\sigma_S^D = \frac{\sigma_L(\cos\theta + 1)^2}{4}$. An example contact angle measurement on the fish's skin is shown in Figure 4.7.

As shown in Figure 4.8, the measured surface energy of the fish skin was found to be 81 ± 2 mN/m. The measured surface energy of parylene was lower at 41 ± 1 mN/m. The contact angles measured and respective sum of dispersive and polar surface energies calculated using the Owens / Wendt theory. The polar and dispersive surface energy components measured for various surfaces can be found in Appendix C.

When testing the device prototype, the array was found to easily slip off of the fish's skin. Because the placement of the array must stay constant throughout the neurophysiology experiment, it was necessary to improve the chemical interface between the array and fish's skin. To better match the surface energy of the fish skin, surface treatment was performed on the electrode array.
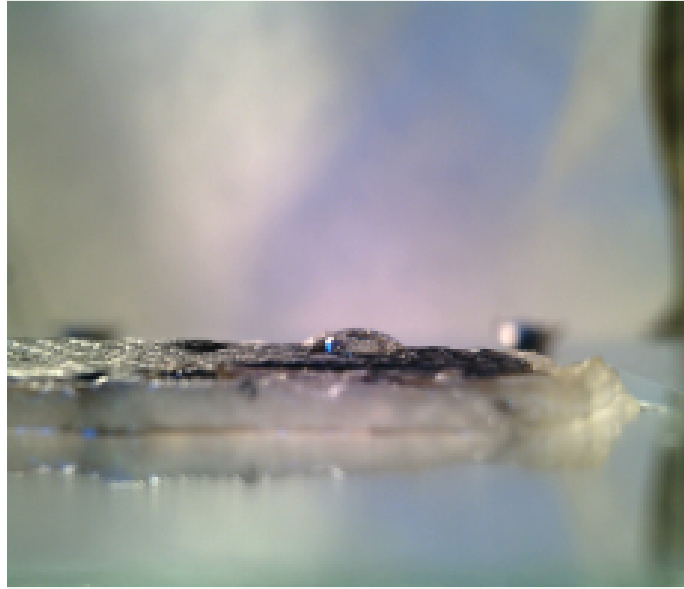
Figure 4.7: An example contact angle measurement setup - diiodomethane on *Gnathonemus petersii* skin.

The focus was to change the surface energy of the parylene since parylene is the top layer of the majority of the array. Results demonstrate that exposing the surface to UV/ozone then spin-coating the surface with 2-Hydroxyethyl-methacrylate (HEMA) altered the surface energy to match that of the fish. HEMA was chosen for its hydrophilic bonds and low toxicity [98].

4.2.3 Current characterization

Another important characteristic of the array was its ability to supply constant current that spreads a few microns in water from the array electrode to the fish electroreceptor. To model the current drop off and spread throughout the water, a constant current was supplied between a platinum wire and thin film metal electrodes of platinum, gold, and aluminum. The wire and electrodes were placed in the water used for mormyrid fish neurophysiological experiments (conductivity of 71 μS). The voltage between these electrodes and the wire was then measured at various distances, as shown in Figure 4.9. The metal electrodes have the same thickness and substrate material (Parylene C
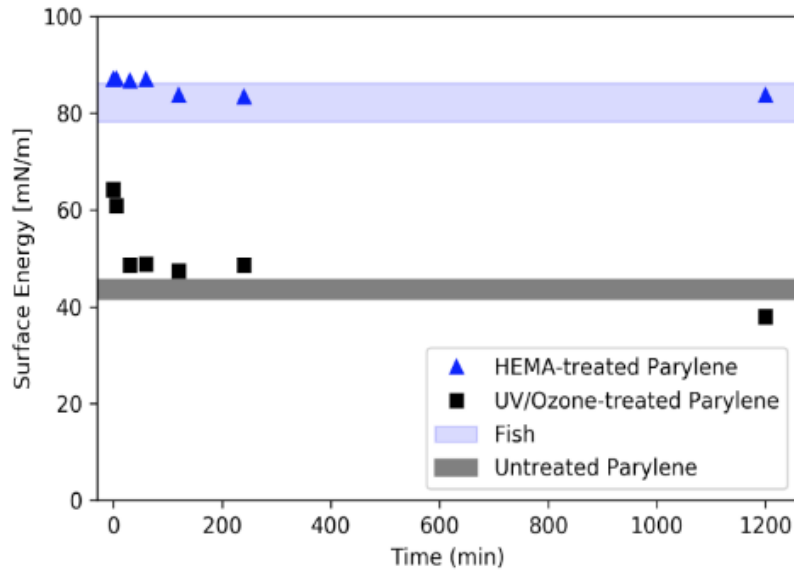
Figure 4.8: Changes in surface energy of the electrode array with HEMA treatment compared to UV/ozone treatment over time. The HEMA treatment increases the surface energy of the electrode array to match that of the fish's skin.

on PDMS) as the metal used in the electrode array but differ in size. This change was made for ease of testing. As expected, the measured resistance of the water in this experiment decreases nonlinearly with distance due to secondary material and electronic effects.

Surface leakage was also measured to determine if any surface or interlayer current spread was occurring. To measure surface leakage, the electrodes were connected using heat seal connectors and the custom heat seal connector connection PCB. The electrode array was placed in a bath of ionized water with conductivity similar to that used during fish local field potential measurements. A source/measure unit was used to source current to one electrode. Then, the current of surrounding electrodes was measured using another meter. A thin platinum wire was used as the ground connection of the source/measure unit and was placed in the water bath, as done in fish experiments.
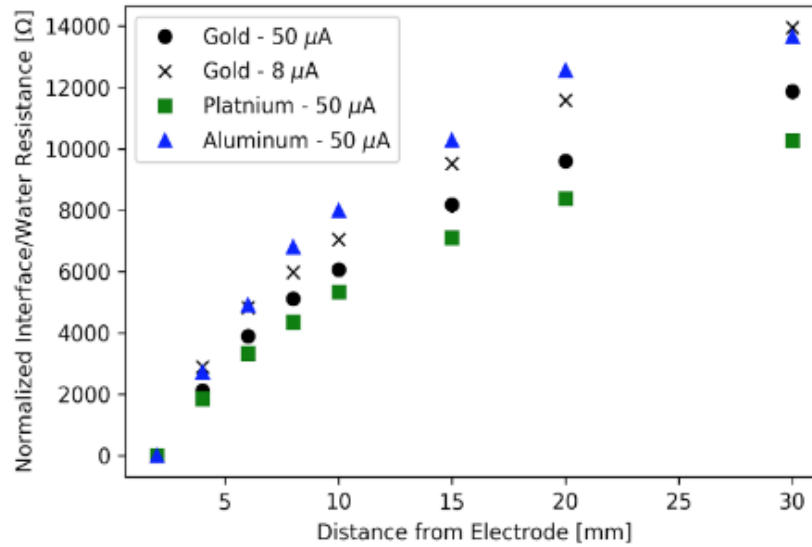
Figure 4.9: Current drop-off with increasing distance from the array electrode.

4.2.4   Electronics

Electronics were designed so that the electrode array could be actively multiplexed for single electroreceptor stimulation. The electrode array was connected to a PCB that contains multiplexers and driving electronics needed to drive various levels of current to all 96 electrodes. Constant current is sourced using a stimulus isolation unit (ISO-Flex, A.M.P.I., Israel).

One multiplexer is used to choose a section of the array. Each section contains a group of 16 electrodes. Each section then has a multiplexer to choose which of the sixteen electrodes was chosen. Each section has 16 electrode connections. The multiplexer used (Texas Instruments, CD74HC4067) has low ON resistance, fast switching speed, and low OFF leakage current. The current source is connected to the input of the section multiplexer. Addressing the section multiplexer directs current to one of the seven electrode multiplexers. The addressed electrode multiplexers then direct current to an individual electrode on the array.

Two custom printed circuit boards were designed. The first connects the array's heat seal connectors to the multiplexer circuit. The second contains the multiplexer circuit and receives addressing information from the Arduino microcontroller. A switch-based circuit was also used to

ensure that no current or floating current was provided to the OFF electrodes.
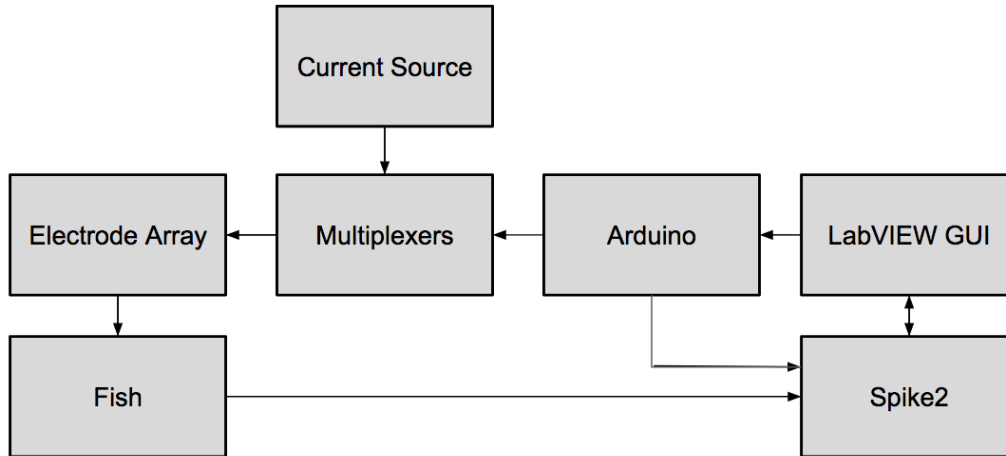
Figure 4.10: System Block Diagram

4.2.5 System

The block diagram of the system is shown in Figure 4.10. There were two system components that allowed for viable neurophysiological data collection: user ease of use and stimulation/measurement synchronization. A simple user interface is critical in this system due to the complexity of the electronic system and need for measurement repeatability. LabVIEW was chosen to control the system then because it can easily be programmed to provide a straightforward user interface. The interface, shown in Figure 4.11, displays a spatially accurate map of the electrodes so that the user can turn each one ON by clicking the corresponding button. The LabVIEW file recognizes which electrode has been selected and transmits electrode information to an Arduino Metro Mini, which controls the multiplexer network used to send current to the chosen electrode. When the button is unselected, the Arduino will receive a code that indicates no electrode is selected and the current will no longer flow to the electrode array. This ON/OFF capability was necessary as varying the time that an electrode was ON was desired.

In order to synchronize the timing of the electrode stimulus and the neurophysiological recordings, time markers were designed in each part of the system and synchronized post-data collection.
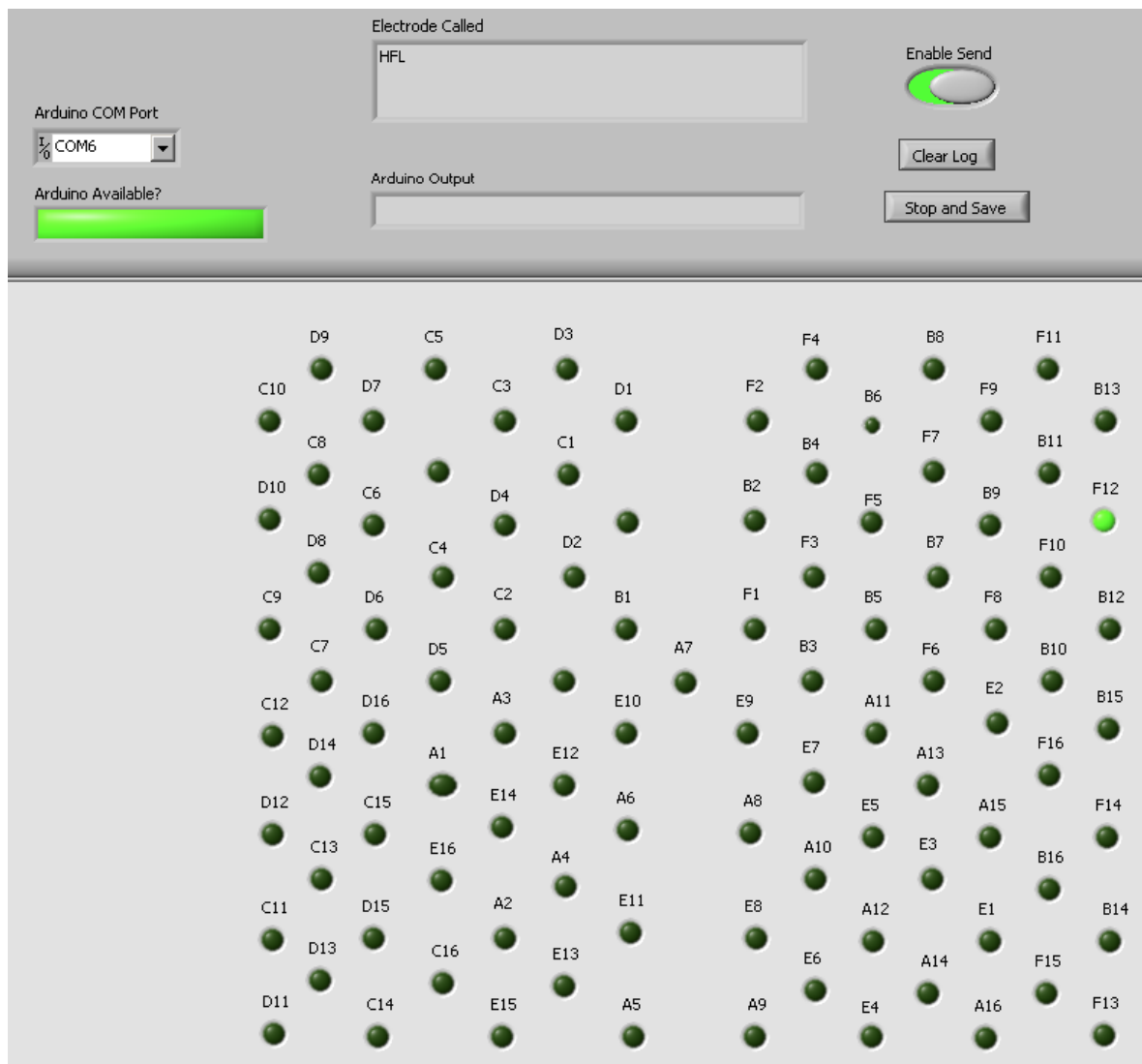
Figure 4.11: LabVIEW UI.

The neurophysiological recordings were acquired using the software Spike2 (CED, England). A digital marker channel was used to set time stamps for the neurophysiological recordings. For synchronizing these time stamps with the electrode stimuli, the Arduino used to control the multiplexer network also provided a byte of digital outputs enumerating the electrode location to the digital marker channel in Spike2 when the electrode was turned ON.

4.3 Results and Discussion

To verify the array's ability to stimulate localized areas on the electric fish's skin, the array was placed on the dorsal area of the fish. While individual electrodes are supplied with current at varying times, the local field potential (LFP) in the electrosensory lobe corresponding to the stimulated electroreceptors was measured.
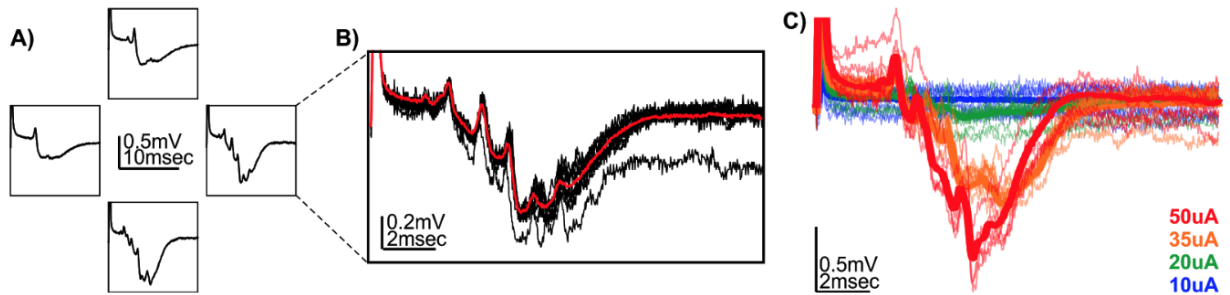
Figure 4.12: Neurophysiology recordings - the local field potential (LFP) in the electrosensory lobe corresponding to the stimulated electroceptors. The measured LFP when an individual electrode (represented as the square box in (A)) is stimulated is shown. In (C), the response to varying amounts of current is shown.

The LFP recordings in-vivo demonstrate that the activation of different terminal sites on the electronic array could drive differential, repeatable activation in a single set of neurons 4.12A,B. As seen in response to individual stimulus presentations, the device has not introduced any additional electronic noise to the LFP recordings beyond what is expected given LFP recordings obtained by previous stimulation paradigms.

Additionally, the system was able to reliably transmit changes in current amplitude through the system by demonstrating that different amplitude commands at the current source (SIU) resulted in different LFP responses to the activation of the same terminal site 4.12C. Therefore, the flexible electronic system developed here has met the criteria needed to begin applying it to the testing of important neuroscience hypotheses with electrophysiology experiments in weakly electric fish.

The next step in determining the encoding of electroreceptor-driven time-dependent action potentials in the first central processing stage of mormyrid fish is to run extensive experiments with the electrode array. Beyond the capacity of the electrode array presented in this chapter, stimulating more than one electrode at a time would allow the scope of the electric stimulation to be greatly expanded. A redesign of the circuitry or the use of an active matrix would allow for this capability.

The biggest hurdle of the system was connecting the various components over long distances; for example, wiring the multiplexer PCB to the microcontroller circuitry. A experiment redo is underway to improve these connections to have stable wiring.

Chapter 5

Plant Spike: A Low-Cost, Low-Power Beacon for Smart City Soil Health Monitoring[1]

5.1 Introduction

The final project presented in this thesis focuses on features that would allow for flexible electronics to be more widely implemented: low power, small form factor, and wireless. The case study for this project consists of designing an IoT node that allows for transmitting sensor data for soil health monitoring.

Urban soils have significant potential to improve urban resilience and climate adaptation through water storage, flood mitigation and carbon sequestration. Urban soils can also advance urban sustainability through the facilitation of temperature regulation and air quality improvements, remediation of brownfield sites, and provision of recreational greenspace. Viewed from the wider perspective of the future of the urban biosphere, there are massive gains to be had from better use

---

[1]Based on C. Yu, K. Kam, Z. Cui, Y. Xu, D. Steingart, M. Gorlatova, P. Culligan, and I. Kymissis, *Plant Spike: A Low Cost, BLE-Enabled Beacon with On-Board Sensors for Smart City Soil Health*, IEEE Internet of Things Journal, *Under review*.

and management of urban soils. For this to happen, significant advances in our understanding of how local conditions and different management practices impact the health of urban soils, and thus the ecosystem services that they provide, are needed. Prior investigations into factors influencing urban soil ecosystem health have primarily involved manual sampling of soils followed by laboratory analysis [99] or labor-intensive site-based measurements [100]. Given the complexity and variety of urban soil systems, and the multiple indicators associated with urban soil health, practices such as intrusive sampling, laboratory testing, and labor-intensive site measurements are unlikely to be effective in generating the knowledge needed to better manage our urban soil systems.

To measure various soil health indicators of tree pits in an urban area, we propose a system that uses a small form-factor printed circuit board (PCB) that transmits sensor data via Bluetooth Low Energy (BLE). Previous BLE sensor solutions integrated on PCBs focus on optimizing the PCB size, power consumption, or functionalities for wearables [101–103]. For example, EcoBT is a miniature wireless sensor node with an on-board accelerometer that uses Bluetooth Low Energy (BLE) for direct communication with a BLE-enabled smart-device [101]. By eliminating the need for protocol bridging between smart devices and a wireless sensor network, EcoBT enables the development of wireless sensor network applications without large changes in hardware design. EcoBT also uses the on-board accelerometer for power saving threshold detection. Another wireless sensing platform, Wristband Vital, is a low-cost wearable multi-sensor using Arduino programming and communicates via BLE with nearby base stations [102]. Wristband Vital uses a burst-mode based variable-rate sensor sampling scheme and low duty cycle to reduce current consumption by its Bluetooth module. EcoBT and Wristband Vital each have a key drawback for Smart City soil health monitoring: high power consumption for multi-year use and a large 3D form factor that disrupts natural soil processes, respectively.

The key advantages of our proposed telemetry solution, Plant Spike, include low-cost (less than $10 for a fully-assembled thin PCB with PCB-integrated sensors and a BLE module) and low-power (two year lifetime with a 400 mAh battery). Plant Spike's low cost is enabled by using a single-chip microcontroller as well as using the PCB as the capacitance sensor. Plant Spike's low

power consumption is enabled by using BLE, which has low peak and ultra-low idle mode power consumption with minimal complexity. Dynamic sensor data is sent through the BLE beacon's universally unique identifier (UUID) fields to further reduce power consumption. Temperature, light, and custom moisture sensors are incorporated on the Plant Spike board to help quantify soil health. The Plant Spike module is shown in Figure 5.1. These modules create a cohesive network that enables seamless data collection through the use of a BLE client. Plant Spike is shown in an example urban tree and soil pit (Figure 5.2).

The main contributions of this project are as follows: (1) To our knowledge, Plant Spike is the first sensor network to incorporate BLE transmit-only connectivity in conjunction with moisture, temperature, and luminance sensors on a small form-factor PCB. (2) We have implemented Plant Spike in a laboratory-based urban soil test bed as well as various locations around New York City, and tested the system by collecting data on urban soil health (3) Our urban soil testbed can be used to calibrate future Plant Spike modules. This testbed features a commercial resistance temperature detector (RTD) sensor and a moisture sensor with a lab furnace to simulate the climatic conditions of New York City that influence soil health.

Bluetooth Low Energy (BLE) allows for low-power and low-cost IoT devices by having ultra-low peak and idle mode power consumption with minimal complexity electronics. Smart Home and other personal area networks using BLE have been presented and can be altered for specific applications [104–108]. In some use cases, BLE devices are reporting sensor readings to a high energy device such as a smartphone [109]. In these cases, two way communication is not always required.

In this work, we demonstrate a significant reduction in the power consumption of such one-way sensor devices by adapting an advertising-only approach to data communication. This approach is achieved by inheriting the power profile normally associated with beacons and applying it to sensor network systems.

Combining a BLE-enabled beacon communication protocol, a small form factor node, the collection of data from multiple sensors by a microcontroller, and low price-point components and
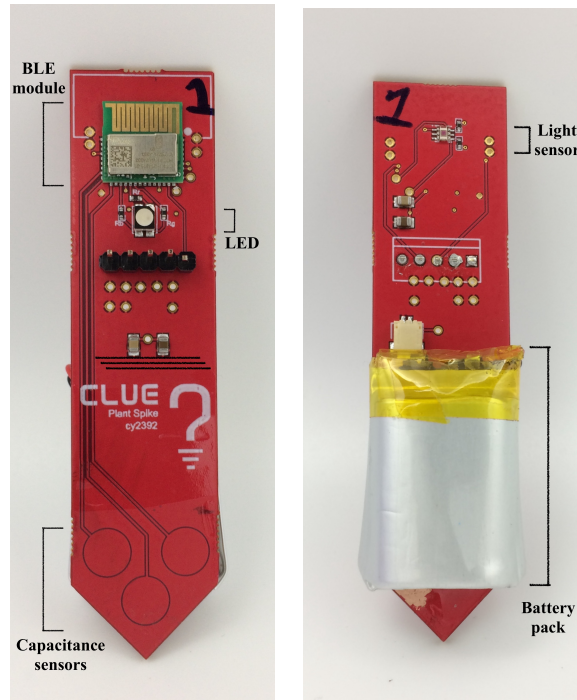
(a) PCB front.   (b) PCB back.

Figure 5.1: Plant Spike custom PCB design with BLE module.

fabrication techniques, we demonstrate a device useful for low-cost low-power sensor node for IoT smart sensing systems. The goal of integrating low-cost sensors with a reprogrammable Bluetooth module is to allow the widespread use of this design for IoT applications.

5.2 System Architecture

5.2.1 Dynamic Transmit-Only Sensor

The system we developed is a variant of an architecture with transmit-only sensors. Because there is no need to reprogram the system once the sensors have been designed and implemented, there is no need for the IoT system to also act as a BLE receiver. The potential of such systems to save power and costs has been noted previously [110]. Transmit-only systems have been studied under a variety of assumptions, including for dense network deployments [111], different network

Figure 5.2: NYC urban soil pit with Plant Spike in soil.

architectures [112], and ultra-wide-band physical links [113]. Transmit-only architectures form the basis for a range of physical layer technologies, including ultra-wide-band communications [113] and backscatter techniques [114]. Within this project, we develop a practical realization of this idea that does not require new communication hardware, software, or protocols.

In this sense, our system is a beacon that transmits dynamic sensor data instead of just an ID. Beacons are an integral part of different wireless connectivity solutions, including BLE and WiFi. There has been much research on improving the security of beacon contents demonstrating the further usability of beacons in IoT applications. Although beacon ID manipulations can be a part of a beacon hijacking or spoofing attack [115, 116], the use of randomized dynamic beacon IDs has been proposed for stopping third parties from using wireless station information for providing localization services [117].

To the best of our knowledge, the use of beacon UUID fields to carry dynamic sensor data to reduce BLE energy consumption has not been proposed before. This beacon manipulation can coexist well with traditional beacon-based systems. To traditional systems that expect the full UUID field to be used to transmit the beacon ID, our systems messages look like different transient beacons coming and going.

Our system uses 4 bytes (32 bits) to represent the device ID. While this is substantially smaller than the full 128-bit BLE beacon UUID space, it is comparable to other commonly used identifiers, including 48-bit Medium Access Control (MAC) addresses used in IEEE 802 WiFi and Ethernet network technologies, and 29-bit device identifiers used in extended-format Controller Area Network CAN2.0B communications. We believe the 2^{32} identifier space available to be sufficiently rich to avoid identifier collisions.

5.2.2 Use of BLE

Our platform uses Bluetooth Low Energy (BLE) as its wireless communication protocol. BLE has several communication and power consumption advantages over previous Bluetooth standards. There are three features in particular that make BLE advantageous for sensor beacons: fewer

channels that advertise, streamlined advertisements, and streamlined security options.

BLE operates in the 2.4 GHz ISM band. While classic Bluetooth uses 79 channels, BLE uses only 40. Three channels (channels 37, 38, 39) are used as advertisement channels to discover devices, initiate connections, and broadcast data. The other 37 channels (channels 0 - 36) are used as data channels once devices are connected [118]. The advertisement channels are separated by a few MHz so that all three channels are less likely to be blocked at the same time. BLE has a star topology; a master can simultaneously connect with several slaves while a slave can only connect to one master. Once a master and slave are connected, a time division multiple access scheme is used to communicate. The devices communicate using an acknowledged stop and wait protocol so that BLE is inherently duty-cycled [105]. Timing BLE channels by encoding information in the interarrival time between BLE advertisements can also be used to increase energy efficiency [119].

Communication via BLE is also optimized by streamlining the content of the advertisements. By setting a unique 128-bit universally unique identifier (UUID) to a custom service, the central device will only search for devices with that UUID. Master devices find clients faster and use less power doing so. Also, compared with Bluetooth 4.1 LE, Bluetooth 4.2 has a link layer payload, of 251 bytes, which is almost 10 times larger. This large payload allows for efficient IPv6 communication over BLE. For sensor IoT devices, a larger payload also allows for the rapid uploading of sensor data from the device to a gateway device.

The Internet Protocol Support Profile (IPSP) enables IPv6-enabled Bluetooth masters and slaves to discover each other using the BLE Generic Attribute Profile (GATT) and establish a link-layer connection [120]. BLE link layer security supports encryption and authentication by using the Cipher Block Chaining-Message Authentication Code algorithm and 128-bit AES block cipher [105]. With this encryption system and BLEs dual-mode capability, data sent from the sensor beacon to the gateway device is secure. BLE-enabled beacons are one-way transmitter broadcasting devices that use the Bluetooth Low Energy communication protocol to transmit their identifiers to nearby BLE-enabled master devices. Typically, BLE beacons transmit physical location, push notifications, or messages to receivers at points of interest such as stores or bus stops. Multiple

BLE beacons in an area can be used as an indoor positioning system for smartphones [106].

BLE has a high level of power efficiency, allowing for battery powered devices. The two main parameters to extend battery life include the advertising interval and the transmittance power, which corresponds to the device's transmit range. The typical range of a beacon is between centimeters and tens of meters [121]. If the output power of the beacon is set to 10 dBm, a range of several hundreds of meters is possible, which is applicable for Smart Manufacturing settings. For Smart Home applications, a range of tens of meters allows for the output power of a beacon to be less than 4 dBm. Other factors that set the beacon range include the sensitivity of the radio receiver, objects in the surrounding environment, and antenna performance.

The beacons also conserve power by sleeping for the majority of the time and waking up to only broadcast information. If the sleep duration is set for longer than one second, the difference in duty cycle for various sizes of the data packets becomes negligible. In general, a longer sleep interval decreases the mean duty cycle; this in turn significantly decreases the power consumption of both transmitting and receiving devices by operating in sleep mode instead of transmission mode for more time [122]. Several papers demonstrate the viability of using BLE-enabled battery powered beacons for an extended period of time [108, 123–126].

5.3 System Design

We combine the BLE beacon model with active on-board sensor data to achieve a low-power low-cost IoT node. The BLE-enabled beacon broadcasts data in periodic packets every one second in this system. By using the Generic Access Profile (GAP) layer to broadcast the data, the beacon is able to send data to any Bluetooth connected device that is configured to receive packets. When the user steps into range of the BLE device, the Bluetooth-connected device receives the transmitted packets, as shown in Figure 5.3(a). While the mobile app is open and listening for the data, the data is displayed and stored. The only packets that are sent in this setup are the UUID that identifies the beacon and the sensor data packets that are included in the UUID. This means that the total number of bytes is 16 bytes. The sequence of transmitted bytes are shown in Figure 5.3(b).
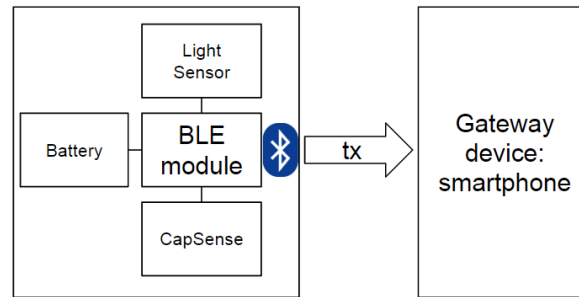
(a) Block diagram showing a BLE module in transmit-only mode sending dynamic sensor data to a gateway device.
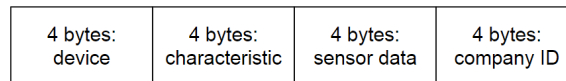
(b) Bytes configuration in the 128-bit UUID. Data is placed between the characteristic byte and company ID byte.

Figure 5.3: Plant Spike system and communication configuration.

Compared to other BLE-enabled IoT systems, Plant Spike has an overall competitive edge with regards to cost, lifetime, size, and ease of use. Table 5.1 references various devices. Compared to other Smart City and wearable applications, Plant Spike has a flattened form factor with the sensors and BLE module only a few millimeters thick on the surface of a standard PCB. The form factor of Plant Spike was chosen so that the moisture sensor can be placed into urban soils while the BLE module is above ground. The PCB size can be reduced by eliminating empty board space; however, the size enables visibility for users that walk up to the implanted system. Compared to miniature BLE platforms, Plant Spike has the same sensing capabilities but is able to be powered on a battery with a third of the power capacity.

We combine the BLE beacon model with active on-board sensor data to achieve a low-power low-cost IoT node. The BLE-enabled beacon broadcasts data in periodic packets every one second in this system. By using the Generic Access Profile (GAP) layer to broadcast the data, the beacon is able to send data to any Bluetooth connected device that is configured to receive packets. The

Table 5.1: Benchmark Table

	Plant Spike	**EcoBT [101]**	**Wristband Vital [102]**	**Smart Cities [127]**
Microcontroller	Cypress PSoC4 BLE	TI CC2540	Atmel ATMega328p	Microchip PIC24F16KA102
Advertisement Current (mA)	15.6	19.6	-	11.3
Deep Sleep Current (μA)	1.3	0.4	0.1	32
Sensors	light, temperature, moisture/capacitive	accelerometer	light, temperature, humidity, pressure, accelerometer/gyroscope	temperature, humidity, and CO_2
Sleep Interval	5 s	0.6 ms - 20 s	-	34 s
Battery	500 mAh	2 AAA	150 mAh	3 AAA
Lifetime (days)	700+	-	4+	-
Wireless Connectivity	BLE	BLE	BLE	ISM
Size (mm)	$20 \times 80 \times 4.05$	8×8	$35 \times 30 \times 11$	$\sim 40 \times 30 \times 15$

only packets that are sent in this setup are the UUID that identifies the beacon and the sensor data packets that are included in the UUID. This means that the total number of bytes is 16 bytes. While the user's mobile application is open and listening for the data, the data is displayed and stored on the mobile or tablet device.

Sensors are placed close to the microcontroller on a printed circuit board (PCB). Sensors that typically have analog outputs (e.g. temperature sensors) are connected to the analog-to-digital inputs. Sensors that typically have digital outputs (e.g. light sensors) are connected to I2C, SPI, or UART-configured digital input pins. Sensor data is only collected by the microcontroller when the microcontroller transmits via BLE. The full PCB design is shown in Figure 5.4.

Figure 5.4: Plant Spike - Generation 1.

5.3.1 Communication

The microcontroller unit used is the Programmable System on Chip (PSoC) 4 BLE from Cypress Semiconductor (CY8C4247LQI-BL483). PSoC4 BLE has a small form factor of 7 mm x 7 mm, general purpose input/output pins that can be used as analog or digital pins, and BLE radio. PSoC4 BLE has a Bluetooth Smart, radio and subsystem (BLESS) that contains a physical layer and link layer with an embedded AES-128 security engine. Because the physical layer is already compliant with Bluetooth Specification 4.1, all that is externally needed is an antenna for packet transmission. The RF transceiver contains an integrated balun to drive a 50 Ω antenna. A higher cost option that does not require antenna and peripheral design is to use the corresponding BLE module by Cypress Semiconductor (CYBLE-214015-01).

When the microcontroller is not transmitting dynamic sensor data, various functions are placed

into sleep or deep sleep mode. The deep sleep mode runs with 1.3 μA while the active mode runs with $\sim$ 10 mA. With a sleep interval of five seconds, Plant Spike is estimated to run on a lithium packet battery for 2 years. Additional battery power consumption modeling is presented below.

5.3.2 Sensor Design

In addition to vegetation water uptake rates, air humidity, light exposure, and exposed surface area affect the evaporation and drying rate of soil. For this reason, a capacitance sensor was designed to measure air humidity as well as soil moisture, a light sensor was chosen to measure the soil's exposure to light, and a temperature sensor was used to measure ambient temperature above the soil.

5.3.2.1 Temperature

The temperature of the air surrounding a soil system is calculated by measuring the temperature of the Cypress PSoC4 BLE microcontroller chip die. An on-chip analog-to-digital sequencer is used to read out the measurement by sampling the voltage output of an on-chip API. The accuracy is 1°C for an operating range of -40 to 85°C [128].

5.3.2.2 Light

Light is measured using Texas Instruments OPT3001, an ambient light sensor. The sensor's measurement range is from 0.01 lux to 83,865.6 lux and the responsivity of the sensor is about 100 ms. The output interface is an I2C connection, which is provided by the microcontroller. The supply range fits within the microcontroller's voltage range and pulls about 1.8 μA of current while operating. OPT3001 also has a small form factor of 2.0 mm by 2.0 mm by 0.65 mm.

5.3.2.3 Soil Moisture

Previous demonstrations of PCB-based soil moisture sensors use a hygrometer that measures the change in capacitance of a material using either a thin-film semiconductor substrate between two electrodes or MEMs topology [129, 130]. To reduce the complexity and cost of the moisture sensor,

Plant Spike measures the capacitance of metal electrodes on the PCB. In our design, the copper that is used for the PCB traces is shaped into circular electrodes and connected to the micro-controller's analog pins. We used Cypress's CapSense technology, which consists of a capacitive sensing algorithm [131]. Although CapSense is most commonly used for capacitive buttons on home appliances and industrial machinery, we have calibrated the copper metal electrodes to precisely measure the relative humidity and soil moisture of the surrounding environment. The electrodes are placed at the base of the board so that the moisture of the soil can be measured without having to insert the entire board in the soil, which would block the light sensor and the antenna.

5.4 Urban Ecosystem Testbed

In New York City, common types of urban soils include modified and engineered soils located within bioswales and tree pits. These urban soil systems are located in openings within city sidewalks and are important to the retention of stormwater runoff and the removal of silt and pollution from runoff water [132]. The performance of these urban soils is heavily dependent on the soil's health, including moisture content and temperature. Currently, soil health monitoring has to be conducted manually. Since there have been more 3000 bioswales and tree pits introduced over the past five years into three of the New York City boroughs alone, the scale of manual monitoring required to understand and quantify soil bioswale and tree pit soil health is not feasible [133]. Plant Spike would replace the need for manual monitoring.

To calibrate Plant Spike's sensors for use in urban soils, a sensor testbed was realized. The purpose of the testbed is to study samples of urban soils in a laboratory environment and to compare the laboratory soil measurements to that of Plant Spike's. The necessity of this setup is required as many of Plant Spike's on-board sensors need to be calibrated in a controlled environment. The physical testbed is shown in Figure 5.5. The main part of the soil container consists of a 15 x 10 x 6 cm acrylic box with holes laser cut into the bottom to allow water drainage. To calibrate Plant Spike's on-board sensors, a commercial moisture sensor and resistance thermometer are placed in the urban soil sample. In addition to measuring room temperature, a Yamata DX600 furnace was

used to simulate large temperature fluctuations. To test Plant Spike's BLE connectivity, a BLE wireless receiver dongle is connected to a dedicated computer to collect and store all measured data.

5.4.1 RTD Sensor Testbed

The temperature sensor included in the programmable microcontroller was calibrated with a resistance temperature detector (RTD). The RTD chosen is platinum that has a resistance of 100 Ω at 0°C [134] and a resistance variation of 0.385 $\frac{\Omega}{°C}$. The RTD and Plant Spike were placed in a programmable oven and refrigerator. The RTD output is measured using a resistance-to-digital
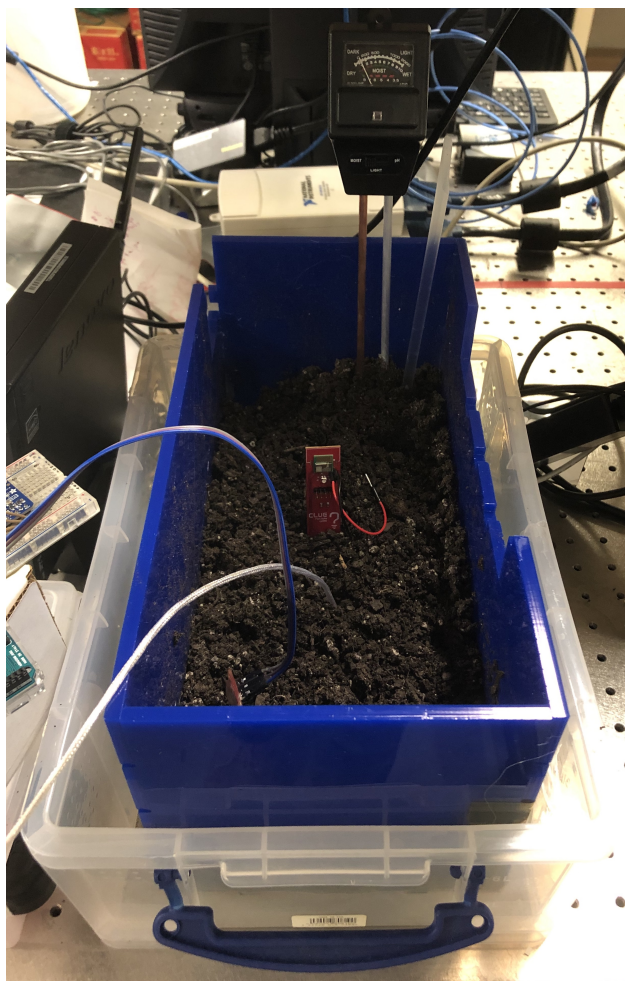
Figure 5.5: Indoor testbed with Plant Spike placed in soil.
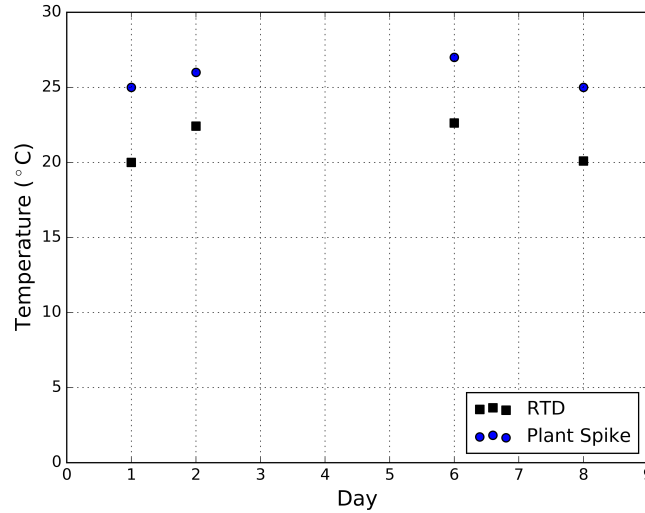
Figure 5.6: Temperature measurements comparing the RTD and Plant Spike thermometer values.

converter and the Plant Spike BLE transmitted temperature is recorded using a BLE client module.

The RTD sensor was also placed directly above the soil's surface at the same distance that the Plant Spike temperature sensor was placed above the soil's surface in order to compare the absolute temperature values. Because of on-board generated heat, the temperature sensor was found to be ~5 ° higher than that measured by the RTD (Figure 5.6).

5.4.2 Light Sensor Testbed

Various light conditions were measured and are shown in Figure 5.7. The location and directionality of the light sensor were taken into account. Under full sunlight conditions, the backside of the PCB, where the light sensor is located, was directed towards the sun when there was no cloud cover. The light intensity in this condition reached the full-scale luminance value of the sensor at 83865.6 lux. In New York City, trees, specifically on the south sidewalk of west-to-east streets have buildings shadowing the tree and tree pits throughout the day. The illuminance of a building's shadow with full sun is about an order of magnitude less than that of full sun. For overcast (90% cloud cover) conditions, the illuminance is less than the reflections of direct sunlight off of buildings in building shadow areas. For thorough characterization, indoor light conditions were also measured. Lastly,
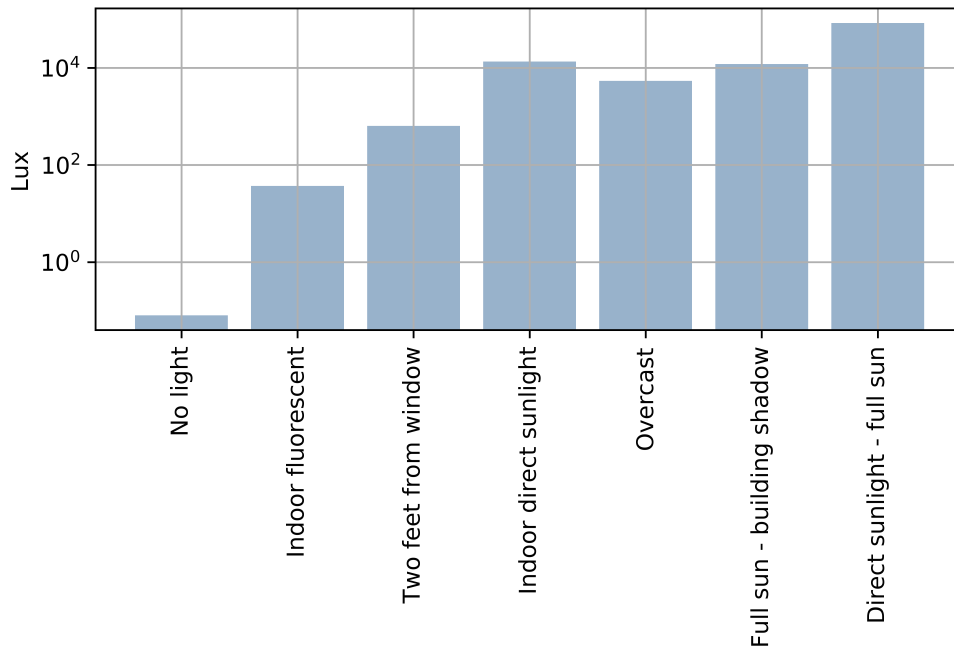
Figure 5.7: Lux for various light conditions.

covering the light sensor was found to be 0.03 lux, which is the dark condition of the sensor.

5.4.3 Humidity Testbed

The capacitance sensors used in this device can be of dual purpose depending on the placement of the sensors. For above soil measurements, the insulated copper pads can be used to measure ambient relative humidity. The humidity of air was increased by evaporating a specific amount of water in an enclosed area. The change in capacitance of one copper pad relative to relative humidity is shown in Figure 5.8. As the data shows, the higher moisture content of the air leads to a larger capacitance read by the insulated copper pads. To translate this change in capacitance to a value for moisture content, a humidity sensor was used to calibrate the relative humidity with the output capacitance of the on-board copper pads.

When the copper pads are embedded in the soil, they can be used to measure water, or soil moisture, content. The capacitance change from dry to wet soil is shown in Table II. The Plant Spike's on-board capacitance moisture sensor as well as an off-the-shelf moisture sensor (SparkFun
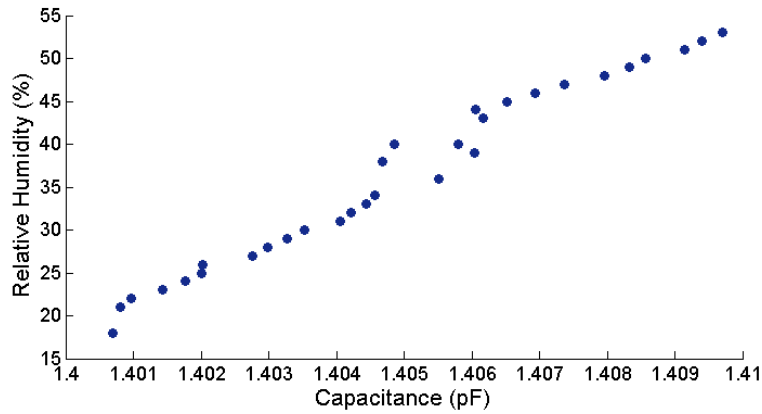
Figure 5.8: Capacitance in relation to relative humidity.

Table 5.2: Normalized capacitance for various soil moisture conditions.

Condition	Plant Spike	SEN-13322
Immediately after watering	0.99	0.94
2 days after watering	0.95	0.62
1 week after watering	0.84	0.51
Dry	0.68	0.06

SEN-13322) were placed in soil. Both sensor outputs were normalized to their maximum respective values. This normalization is important as it allowed us to compare the moisture readings on a similar scale. The normalized moisture data was collected from soil in the indoor testbed in 4 different states: just watered with 1 liter of tap water for 450 cm^3 of soil, 2 days after watering, 1 week after watering, and purely dry soil.

As seen from Table II, both columns of normalized moisture data show a downward trend. This result is expected as water drains and evaporates out of the testbed over time until the soil returns to a dry state. Thus, when applied to field measurements, values approaching a normalized moisture value of 1.00 correspond to fully saturated wet soil.

5.5 System Implementation

To verify the effectiveness of Plant Spike's ability to monitor tree pit soil health, Plant Spike was placed in tree pits throughout New York City's Morningside Heights neighborhood. Figure 5.14 shows the location of the implanted tree pits in the Morningside Heights community.

Tree pits in New York City have two primary configurations: guarded and unguarded. Guarded tree pits have fencing that surrounds the recessed soil pit that prevents humans and small animals from stepping on and contaminating the tree pit soil. Unguarded tree pits do not have the protection of the fencing and thus are more prone to soil compaction and contamination, which damages the tree and by extension the tree pits ability to deal with stormwater. Examples of New York City tree pits are shown in Figure 5.9.

(a) Unguarded tree pit.   (b) Guarded tree pit.

Figure 5.9: Examples of NYC tree pits.
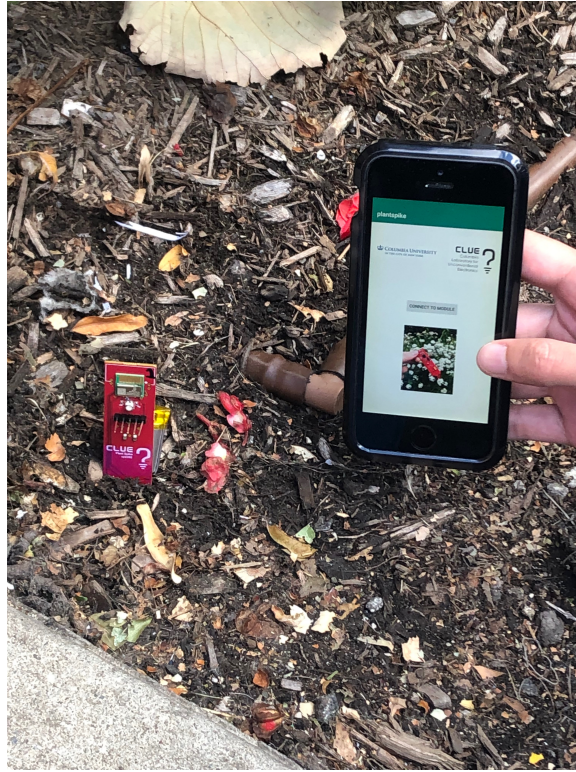
Figure 5.10: Smartphone application to connect to Plant Spike module via BLE.

Aside from type differences, tree pits also come in many sizes. These sizes range from 0.9 m^2 to 4.6 m^2. A study by [100] explored the influence of tree guards, area and size, ground cover vegetation, and mulch in the tree pit on tree pit soil infiltration rates as an indicator of soil health. The results of the study showed that infiltration rates in guarded tree pits with large areas were higher than rates measured on other tree pit types. To come to this conclusion, researchers used in-field infiltrometer measurements, which were difficult and labor intensive to perform [135][136]. As Plant Spike is a smaller, cheaper, and easier to use than an infiltrometer, the successful implementation of these modules in the field helps demonstrate that Plant Spike can be used effectively to characterize tree pit health. The data for these measurements can be found in the results and analysis section of this chapter.

After placing the Plant Spike two millimeters into soil, the sensor data was collected. A smartphone app was developed to receive and display the data. Although data processing still needs to

be performed in a lab, designing the smartphone app provides a future path for integrating Plant Spike into a connected smart city application. Figure 5.10 shows the smartphone app with an implanted Pant Spike module. In the long term, we hope to monitor urban soil health over longer periods of time that capture varying weather and other environmental conditions. Plant Spike has demonstrated a long battery life in a laboratory setting, and with the continued development of the sensing and weatherproofing capabilities we are seeking to implement a long term study in the near future.

5.6 Results

5.6.1 BLE

The current consumption of two-way communication is shown in Figure 5.11. Because the connecting stage of the communication process consumes almost twice the amount of current as the
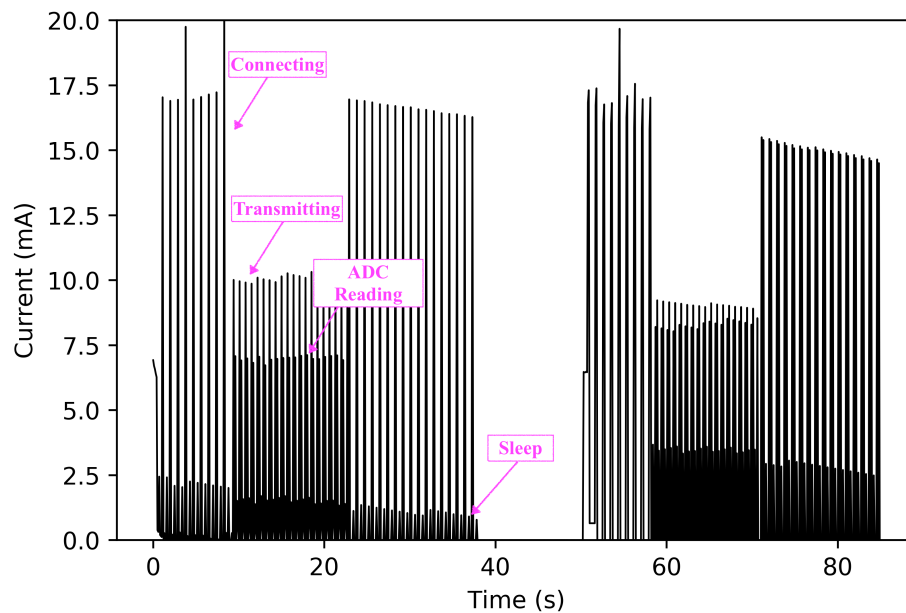
Figure 5.11: Experimentally measured two-way communication current consumption using CYBLE-214015-01. Plant Spike only consumes the power needed for transmitting and reading sensor values (as shown between 10 and 20 seconds).

transmitting stage, the power consumption of a transmit-only sensor reduces significantly. To obtain the current consumption of the device, the BLE module was programmed to connect to a BLE client and transmit sensor data values once connected. A source/measure unit is used to supply voltage to the BLE module while measuring the current flow through the device.

As shown in Figure 5.11, a typical BLE current cycle consumes about 17.5 mA during the connecting phase and 10 mA during the data transmission phase. When the module is in its connecting state, it is advertising its identification information and waiting for a connection with a master client device. Once connected, the module is programmed to transmit dynamic sensor data within the UUID. Transmission consumes less power than the connecting state. Before each transmission, sensor data values are collected and stored from the ADC output, I2C bus, and capacitance readings. Throughout the connecting and transmission state, the BLE module is programmed to sleep.

For one-way transmission, the BLE module is programmed to only transmit its UUID with dynamic sensor values stored within the UUID. The BLE client parses the UUID to identify and store the sensor values. In this case, the BLE module turns on for 1 ms to collect data and transmit; then it sleeps for 4999 ms.

To determine the operating range of Plant Spike's wireless BLE connectivity, a portable laptop using a Cypress Semiconductor CY5670 CySmart USB Dongle was set up as a BLE client. Once connected, the Plant Spike module was moved away from the BLE client while the client-side received signal strength indicator (RSSI) was measured. Figure 5.12 shows the relationship between RSSI and Plant Spike's distance away from the client. Between 0 - 25cm the RSSI value drops rapidly and then hits a steady value of -90 dBm as the distance increases. This plot shows that BLE client devices that want to connect to Plant Spike should be kept with 25 - 50 cm of Plant Spike's antenna. This distance is reasonable for a researcher or city resident standing by the Plant Spike and tree pit to collect sensor data.
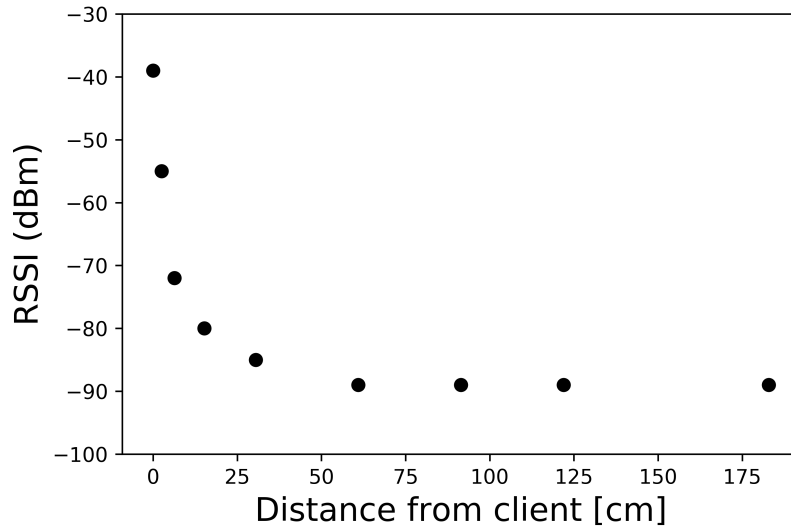
Figure 5.12: RSSI vs distance between the receiver and Plant Spike.

5.6.2 Battery Analysis

To verify the health of Plant Spike's battery after many months of data collection, a battery discharge curve was generated. To develop the discharge model, Plant Spike's 3.7 V, 500 mAh lithium ion polymer battery, manufactured by TinyCircuits, was tested on a Neware CT-4008-5V10mA-164-U Battery Testing System. To simulate the battery load current draw of a BLE module transmitting wireless packets, the battery was discharged at 1 mA for 60 seconds followed by 10 mA for 1 second. This protocol corresponds to one cycle of discharging. To completely discharge the battery. the process took 25681 cycles. The purpose of this protocol is to model the pulse discharge in a simulated application. The battery was fully charged to 4.2 V at the beginning, and experienced 25681 cycles to hit 3 V, which is assumed as fully discharged. The discharging curve reflected the expected Nernstian Behavior, and the Coulombic efficiency is 100%, which suggests that the battery is in good condition after field testing. The battery discharge curve and test setup are shown in Figure 5.13(b).

It is clear from the battery testing that sleep modes are necessary to reduce the average power consumption and lifetime of the device in addition to being a transmit-only sensor. When the

(a) Battery test setup.
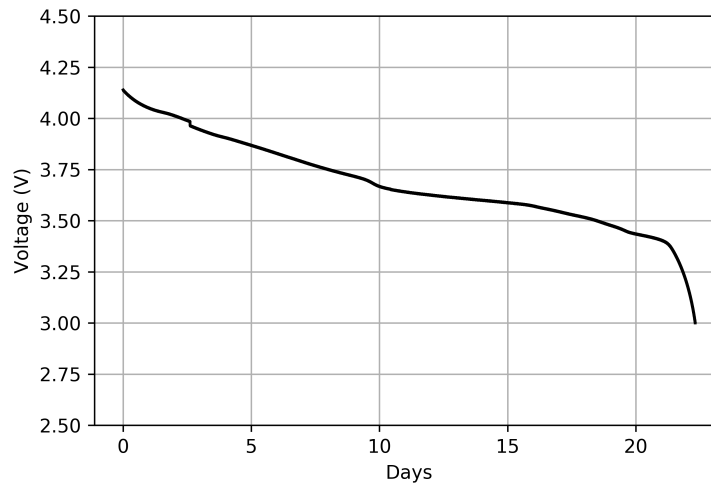
(b) Battery discharge over time. Discharge cycle was 10 mA for 1 second and 1 mA for 60 seconds. This "sleep" current consumption is an order of magnitude higher than that of our system.

Figure 5.13: Battery health verification.

microcontroller is placed into deep sleep mode (1 μA) between transmissions instead of sleep mode (1 mA), the discharge length is extended to over 2 years.

The battery voltage discharge plot provides a model that can be utilized to estimate the current

lifetime of the Plant Spike module under test. Plant Spike's on-board ADC can digitize and acquire the battery's voltage and compare it to the discharge model to determine how many cycles Plant Spike has been running and approximate the remaining battery life of the sensors. This analysis will be implemented in future versions of Plant Spike's smartphone app along with the other sensor values of interest.

5.6.3 Field Data Analysis

Plant Spike modules were placed in four tree pits around New York City's Morningside Heights neighborhood. The data shown in Figure 5.15 represents 40 seconds of temperature data to confirm the outdoor field measurements. The lines labeled 1-4 correspond to the locations displayed in Figure 5.14. The data shows that locations 2 and 3 have lower light levels as the tree pits were covered with a building's shadow. The tree pit in location 4 was in direct sunlight while the tree pit in location 1 was partly covered by the tree's leaves' shadows. Location 1's light level fluctuations were caused by leaves blowing in the wind.

Figure 5.14: Locations of measured tree pits near Columbia University's Morningside Campus.
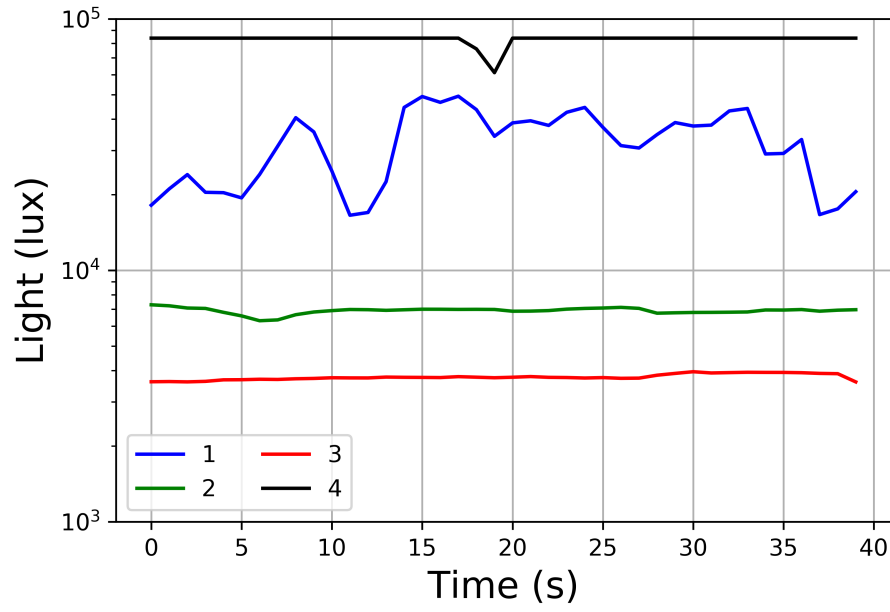
Figure 5.15: Fluctuating light at tested locations.

Table 5.3: Temperature and Soil Moisture Measurements at Tree Pit Locations

Location	Temperature (°C)	Soil Moisture	Type
1	20	0.988	Unguarded
2	19	0.980	Guarded
3	16	0.553	Guarded
4	19	0.678	Unguarded

Temperature and moisture were also measured at each tree pit location and is displayed in Table III. Comparing the temperatures between all 4 spots, location 3 had the lowest temperature by far. There are various factors in tree pits that create temperatures differences. These factors include: the amount of shade from neighboring buildings and trees and the wind speed through the street.

Locations 1 and 2 had the highest soil moisture. These locations did not have large trees to prevent precipitation from ponding on the soil surface, and thus were thus less efficient in their water drainage performance. The data collected from the four tree pits demonstrate the information that can be obtained on soil health using light, temperature, and moisture measurements.

5.6.4 Cost and Scalability

The reason for using a small footprint, low-cost BLE module and sensors is to provide a scalable device for Smart City IoT implementations. The first design of the PCB used a custom antenna network to reduce the overall cost. For quick prototypes, a BLE module replaced the custom BLE peripheral circuit. Cost comparisons per 1000 manufactured is shown in Table IV.

The cost per unit is less than 10 United States dollars. This is significantly cheaper than standard infiltrometer measurements in terms of labor cost, material cost, and overall size cost. By connecting on-board sensors to a microcontroller chip instead of a microcontroller development board and using part of the PCB as the capacitance sensor, Plant Spike is also less costly than previously demonstrated tree and soil monitoring IoT systems [137, 138]. The overall goal of Plant Spike is to scale Plant Spike implementations to many locations around New York City, where soil health is of interest and where data can be easily collected using a BLE client device. Plant Spike's low cost make it an attractive option for municipal maintenance teams and even for everyday citizens interested in checking on their neighborhood tree pits.

Table 5.4: Plant Spike component, assembly, and total cost (per 1000) as of 2019.

Component	Plant Spike (Custom BLE Peripherals)	Plant Spike (BLE Module)
PSoC4 BLE	1.35	9.66
Light Sensor (OPT3001)	1.14	1.14
Peripherals	0.543	0.103
CR2032 Battery	0.62	0.62
PCB	0.90	1.14
Assembly	4.85	2.52
Total ($)	**9.403**	**15.183**

5.7   Conclusion and Future Work

For the first time, a low-cost low-power IoT soil health sensor has been developed and implemented in various locations in New York City. The soil health sensor can monitor various characteristics of the soil such as moisture, light intensity, and temperature to monitor and diagnosis the health of urban soils. In addition to monitoring soil health, Plant Spike is a BLE-enabled IoT system that seamlessly integrates on-board sensors with minimal additional connections needed. By implementing the system, we realized a network of BLE-connected low-power sensors can be placed in urban soils locations, such as bioswales and tree pits, and left for up to two years before replacement with no damage to the battery. The sensors can be accessed with a smartphone app for ease of use. This data will provide new information regarding soil quality in urban settings, including measurements for the concentration of contaminants such as animal and chemical waste and the severity of soil compaction. The next generation of Plant Spike will incorporate improved long-term weather resistance, increased on-board memory, and a higher sampling and polling rate for data acquisition and transmission. Additionally, we plan to integrate Plant Spike into a wider variety of tree pits and green spaces to monitor water infiltration capacity, pH level, dissolved oxygen content, and other various issues intrinsic to urban soil health. Currently, we plan to incorporate Plant Spike sensors

into 40 additional tree pits around various New York City communities. Data will be collected from these tree pits once every week using an improved version of the custom smartphone app.

To our knowledge, Plant Spike is the first sensor node that sends only dynamic sensor values to a BLE-enabled device using the BLE Beacon model. It has a low cost of goods value that is less than $10 and all communication and sensor components are on a small form-factor PCB. The first use-case for Plant Spike was to monitor various house-plants. By monitoring many house-plants at once, we will develop a Plant Spike network to test the viability of Smart Home environmental monitoring. The sleep-wake duty cycle of the microcontroller transmission will be tuned for optimal user experience and low power consumption. The next use-cases include placing Plant Spike in bioswales and outdoor gardens to monitor outdoor environment conditions. We believe that Plant Spike can be easily altered to measure environmental conditions other than temperature, light, and moisture. Several complementary Smart City applications include water, air quality, and sewer monitoring. These sensor networks have yet to be implemented and Plant Spike can serve as a platform for the design of low-cost and low-power IoT sensor nodes.

As part of NSF's EAGER SitS: Signaling the Health Of Tree-pit Soil (SHOTS) grant (Award Number 1841615), we are actively developing a second generation of Plant Spike that measures soil pH and dissolved oxygen content.

Chapter 6

Conclusion and Future Work

The work of this thesis focuses on the development of flexible hybrid electronic devices. With device fabrication and characterization completed, future work includes utilizing each device to gather information on the complex system it is a part of. Whether that complex system is robotic grasping in unknown environments or sensory processing in the brain, each sensor is available to obtain rich sets of data.

The projects completed followed similar paths: project specification, device design, fabrication optimization, electronics design, integration trouble-shooting, and testing. The ultimate goal of the projects presented in this thesis is to design functional devices that leverage flexible technologies to improve the practices of techniques in other fields. Along the way, optimal fabrication methods were determined and the exploration of commercially viability was performed. Several highlights include patterning flexible devices with thin films on top and bottom sides using simultaneous wet developing and etching, combining inverse tomography with capacitive proximity sensing, and designing a BLE node with a cost of <\$15.

There exists a great need to develop robust sensors for robotic applications as well as reliable stimulation setups for neurophysiological research. For wireless solutions of each application, low power consumption is necessary, which was explored by designing a low-power Bluetooth-connected IoT node. Eliminating the noise generated from moving wires in robotics as well as the long wires needed to isolate electronics from the stimulation array would greatly improve future data collection.

The biggest setbacks were the turnaround times for device testing. Fast device fabrication was achieved with efficient device design and process flow choices; however, system turn-around, including debugging of hardware, always proved to be the bottleneck of the process. Benchtop hardware is more robust and reliable than custom PCBs; however, it is necessary to seamlessly integrate small-form factor PCBs for a working system. Miniaturizing sensors-on-PCBs is explored in the project presented in Appendix B.

Interesting future projects would focus on developing circuitry for low-power sensory systems that include the flexible and miniature devices developed in this thesis. Another area of interest is high bandwidth wireless transmission of small nodes. When low sampling rates are needed, as presented in Chapter 4, low-power nodes already commercialized are sufficient. For audio or other high sampling rate devices, small form factor wireless systems need to be developed. Lastly, the greatest need in flexible electronics is the development of flexible electrodes and connectors that connect soft substrates to flexible, but stiff, boards.

Part II

Appendices

Appendix A

ITO Electrode Array

This appendix presents the use of an ITO electrode array for neuronal recordings. The electrode array is placed on the bottom of a GRIN lens for simultaneous optical and electrical recordings. The array will be integrated with existing microscopy technology developed by a multidisciplinary Odor Plume Neurophotonics (OPeN) team (NSF Award Number: 1926676) [139–142].

The device requirements include 25 μm spacing for single neuron recordings, transparency at the wavelength of the laser used for optical recording (920 nm), and a surface area of a $\sim 200\mu$m diameter circle to measure at the center section of the GRIN lens.

A.1   Device and System

ITO was used as the electrode material. At a thickness of 75 nm and with a light source of wavelength 920 nm, ITO is 85% transparent [143]. Parylene was used as the substrate layer because of its optical transparency and relatively high user durability at a thickness of 5 μm. The device design is shown in Figure A.1. The electrodes are 12 μm squares and spaced hexagonally 34 μm apart. The electrodes cover a $\sim 200\mu$m diameter circle and the entire device, including electrodes and contact pads, is a 9 mm by 9 mm square.

For fabrication, a carrier glass slide (5 $\times$ 5 cm) is solvent cleaned with sonication and silanized for easy post-process peel-off (trichloro(1H,1H,2H,2H-perfluorooctyl)silane). 5 μm of parylene is
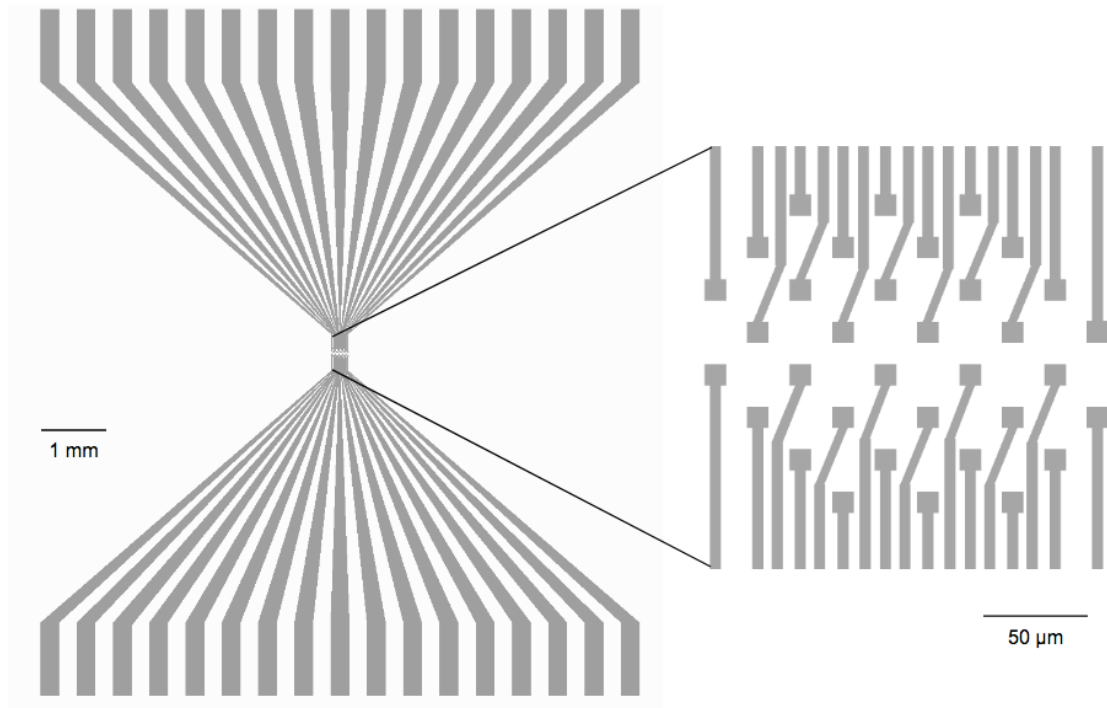
Figure A.1: ITO electrode array design.

chemical vapor deposited onto the glass. Then, 75 nm of ITO is sputtered onto the parylene layer. To pattern the ITO thin film, direct-write photolithography was used:

- Spin-coat S1805 - 500/3000 rpm for 30 seconds

- Soft-bake for 1 minute at 120°C

- Heidelberg DWL direct write

- Post-exposure bake for 1 minute at 100°C

- Develop in AZ300MIF for 50 seconds

- Hard bake for 1 minute at 120°C

The ITO was etched in an ICP RIE chlorine etcher. The photoresist is stripped using a heated bath of AZ400T. A second layer of parylene was deposited onto the device to encapsulate the traces.

This parylene layer was patterned using the aforementioned process: an aluminum mask and a RIE oxygen etch.

The fabricated device is shown in Figure A.2. The electrode array is adhered to the GRIN lens using UV-curable epoxy is shown in Figure A.3 (NOA68, Norland). Heat seal connectors are used to connect to the array's connection pads to a custom PCB that integrates with an existing optical microscopy setup. The system model is shown in Figure A.4.

The custom PCB design is shown in Figures A.5(a) and A.5(b) and the pictures of the system is shown in Figures A.5(c) and A.5(d). Each electrode is connected to an input of a headstage channel amplifier breakout board (RHD2000, Intan Technologies).
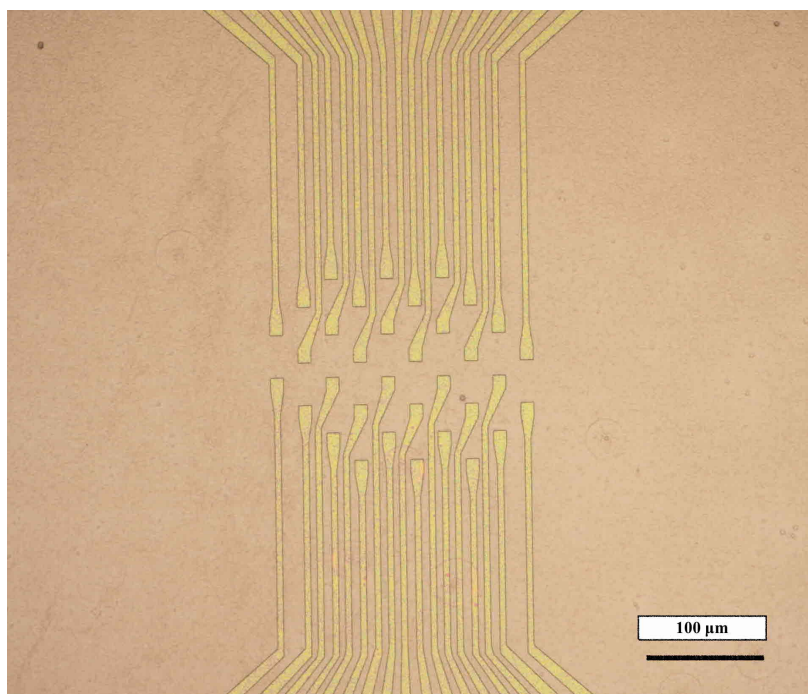
Figure A.2: Fabricated ITO electrode array on parylene.
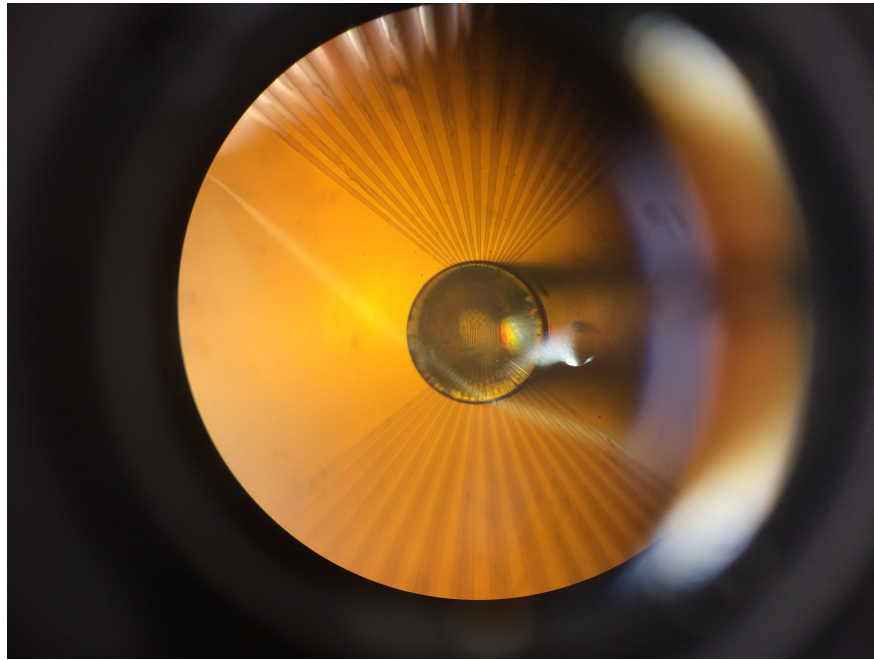
Figure A.3: ITO electrode array adhered to the bottom face of a GRIN lens.
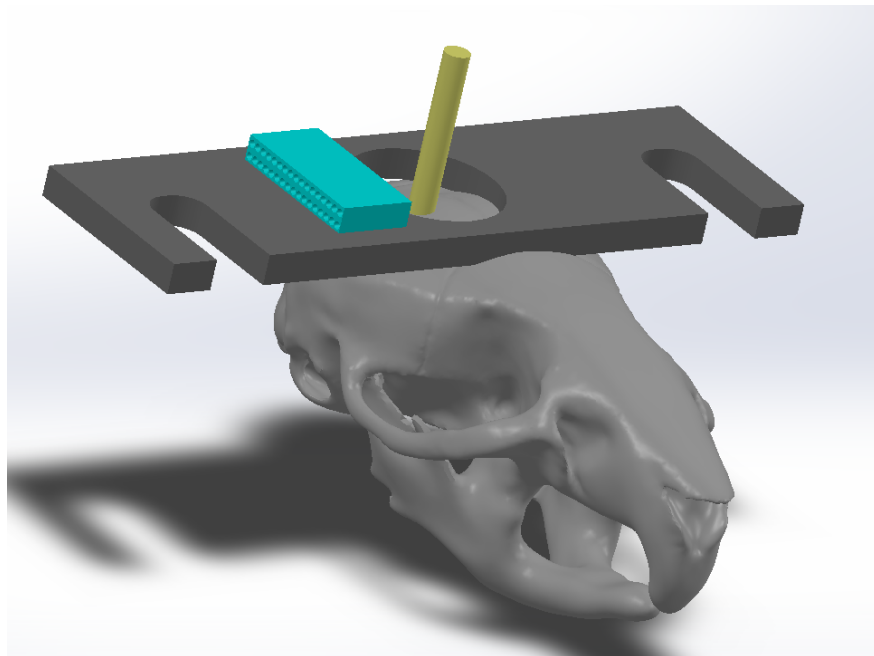
Figure A.4: Solidworks system model - image courtesy of Connor McCullough.
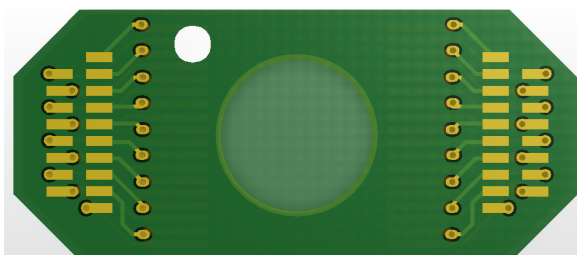
(a) Top of custom PCB with footprint for Omnetics connector.
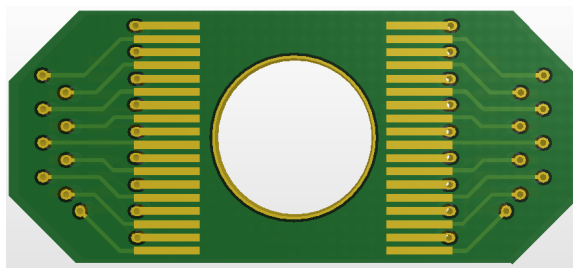
(b) Bottom of custom PCB with footprint for heat seal connection pads.
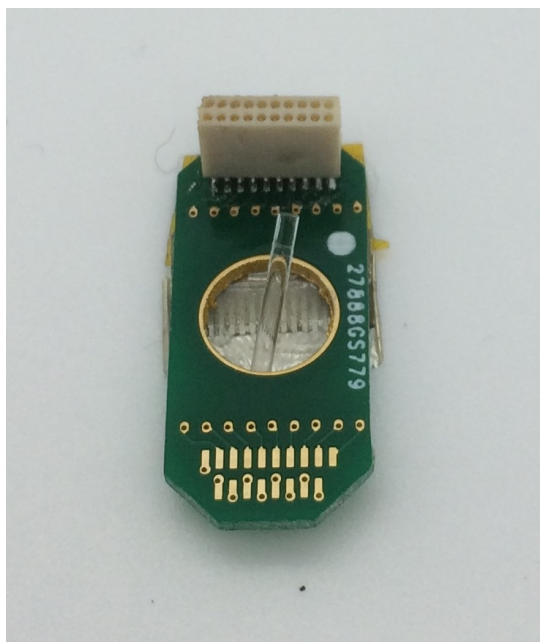
(c) Custom PCB with one Omnetics connector and array attached to GRIN lens and bottom of PCB - bird-view.
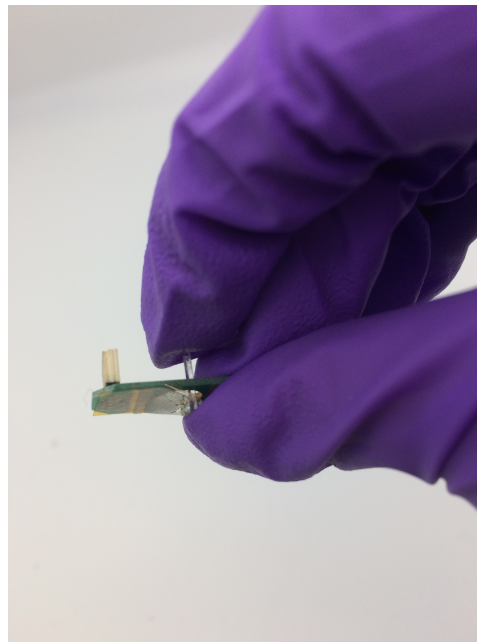
(d) Custom PCB with one Omnetics connector and array attached to GRIN lens and bottom of PCB - side-view.

Figure A.5: Custom PCB integration with electrode array and GRIN lens.

A.2 Future Tasks

There are several future tasks to produce a robust electrode array and system integration. The first task is to add alignment marks on the electrode array pattern to enable easier alignment, placement, and adhesion of the electrode array onto the bottom of the GRIN lens. Connor McCullough (University of Colorado Boulder, University of Colorado Anschutz) will be designing a setup to enable precise alignment. The second task is to elongate the traces between the electrodes and connection pads so that there is minimal addition of material inside the brain. Longer traces will enable the heat seal connector to be short and be external to the brain. Vikrant Kumar has redone the design and fabricated new samples.

Appendix B

Soundscape

Flexible and miniature electronic devices can help develop understanding on how animals behave in natural situations and how sensory information is processed in the brain. Typically, heavy large rigid electronic devices are used on head-fixed animals [144, 145]. This type of experiment has illuminated our knowledge on neuronal circuits; however, the mouse's natural behavior as well as sensory stimulus is limited.

A field of interest in neuroscience is to study how the nervous system distinguishes between external events and self-generated movements. The Sawtell Lab has studied the licking behavior of head-fixed mice [146]. The device presented in this appendix has simultaneous high frequency sampling of sound covering the hearing range of mice with detailed characterization of behavioral responses to external sounds. Behavior is measured using a 9-axis inertial sensor for head movement and a camera for pinna movement. Components are placed on a flexible printed circuit board with minimized weight and surface area to allow for studies of an array of natural behaviors in freely-moving mice.

B.1   System Design

To allow for naturally behaving mice, the device is required to be smaller than the surface area of the mouse's skull and be lighter than 3 grams. To measure mice vocalizations as well as surrounding

noises, a high cut-off frequency microphone with a small footprint was chosen (SPU0410LR5H-QB, Knowles). SPU0410LR5H-QB is omnidirectional, low current (120 μA), has good sensitivity up to 80 kHz, and a flat frequency response up to 10 kHz. The size and weight of the microphone also satisfies the system requirements at 3.76 mm $\times$ 3.00 mm $\times$ 1.10 mm and grams, respectively. Because the microphone has a bottom port, it is placed on the backside of the custom PCB.

To track the mouse's movement in relation to sound, a 9-axis tracking device was used to track the mouse's head movement and a camera was used to track the mouse's pinna movement. The mouse's head movement was captured by a 9-axis accelerometer, gyroscope, and magnetometer device (ICM-20948, TDK InvenSense). The 9-axis sensor is low power at 2.5 mW and has a small footprint at 3 mm x 3 mm. To track the mouse's pinna movement, an image sensor integrated with Raspberry Pi is used (Sony IMX219).

Both the microphone and 9-axis sensor are placed on the flex PCB with a miniature connector as shown in Figure B.1(a) and B.1(b) (A79609-001, Omnetics). The Omnetics connector corresponds with a pre-wired mate connector (A79605-001, Omnetics). PCB fabrication and assembly was performed by Macrofab or PCB Minions.
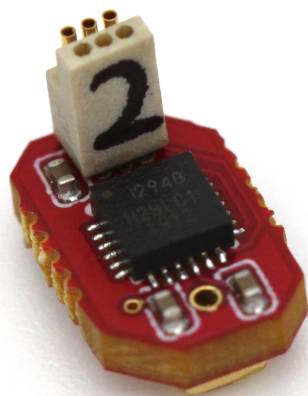
(a) 9-axis device and connector.
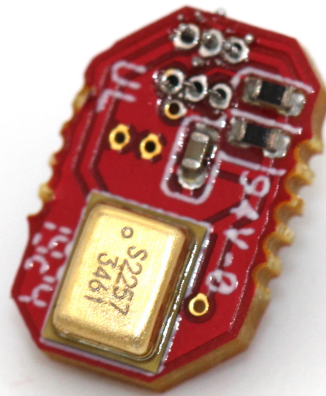
(b) Microphone and peripherals.

Figure B.1: First prototype of Soundscape system. The top of the PCB is seen on the left and the bottom of the PCB is seen on the right.

Figure B.2: Flex PCB version of device implanted in healthy free-roaming mouse.

Component	Connection	Software
Microphone	Analog output	CED 1401 / Spike2
Inertial Sensor	serial	serial monitor
Camera	CSI	Raspberry Pi / Python

Table B.1: Sensor Connectivity

The key parameter to collecting data in this system is synchronization. The connection protocol for each sensor is listed in Table B.1. A master sync signal was from a standalone microcontroller. Data is collected and transmitted from each component once it has received the sync signal.

B.2 Preliminary Data Collection

The device successfully measures sound, head movement, and pinna movement simultaneously. Recordings from each sensing mode is shown in Figures B.3- B.6. The microphone records sound up to 80 kHz. Spike 2 was used to visualize the sound recordings. The inertial sensor measures 9-axes of movement. Angular head displacement was calculated using the method presented in [144]. The pinna camera visually records movement. Image tracking was completed to track certain areas of the pinna.

B.3 Future Tasks

Future goals include transmitting component information via Bluetooth or another low power wireless protocol and using energy harvesting devices for powering the device. The device will be tested while recording various behaviors and emitting sounds from a speaker array.
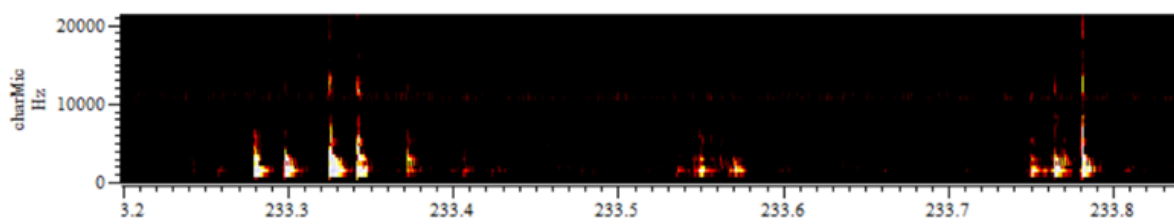
Figure B.3: Microphone recording.
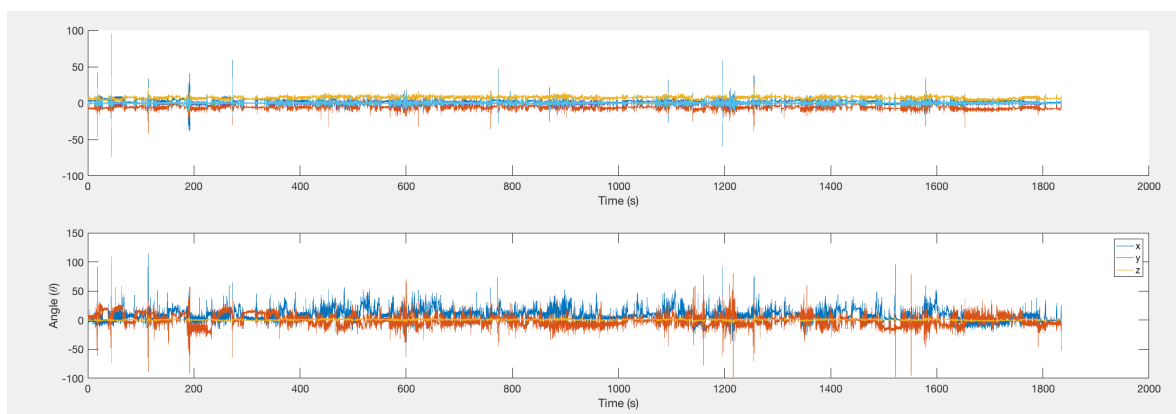
Figure B.4: Inertial recording: raw data (top) and calculated head angle movement around x and y axes (bottom).
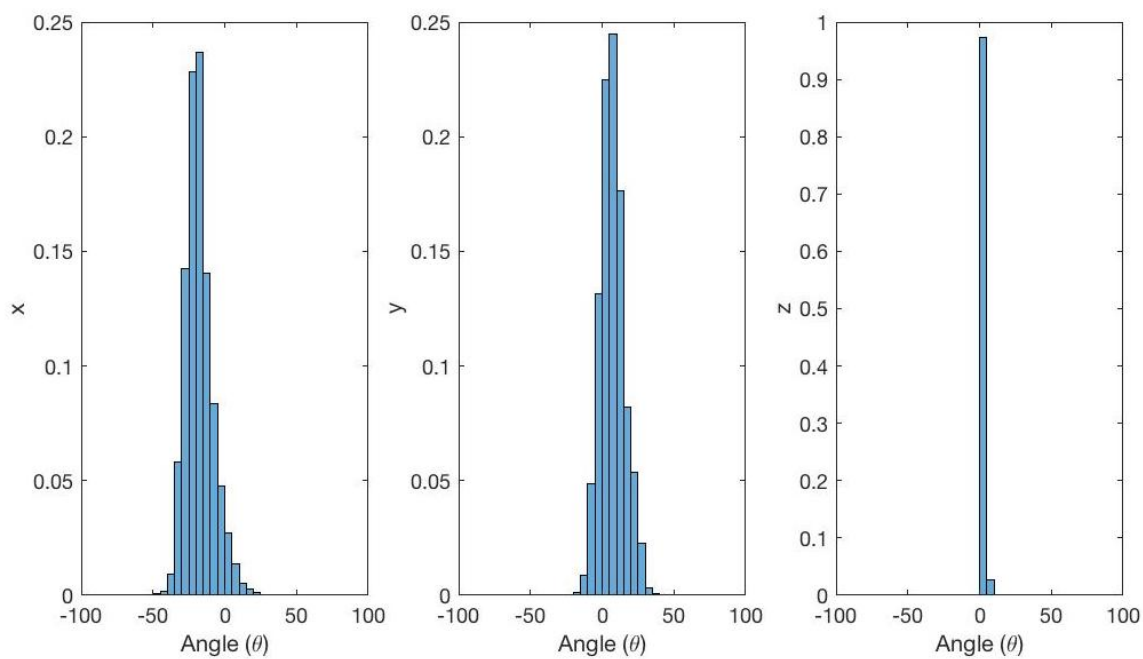
Figure B.5: Frequency histogram of angle movement. Results match well with recordings presented in [144].
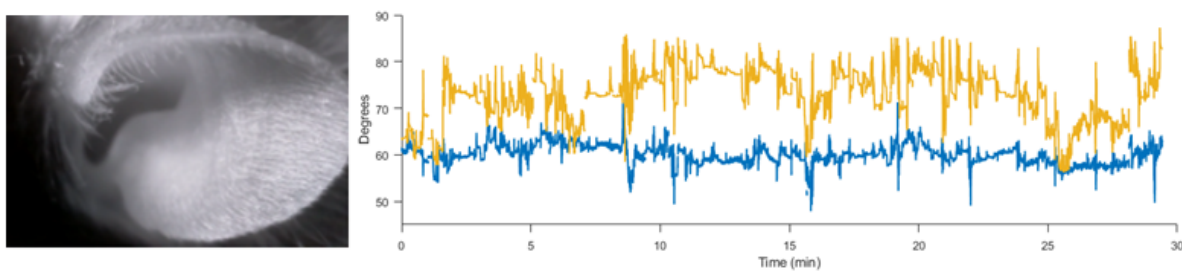
Figure B.6: Pinna movement video and movement tracking data.

Appendix C

Surface Energy Measurements

Table C.1: Measured surface energy components and total surface energy of various material surfaces. Values have units of mN/m.

Surface	Polar surface energy	Dispersive surface energy	Total surface energy
Parylene	0.499	41.090	41.589
Al/Parylene	13.420	34.636	48.056
Au/Parylene	3.111	49.600	52.711
Parylene/PDMS	1.711	45.376	47.087
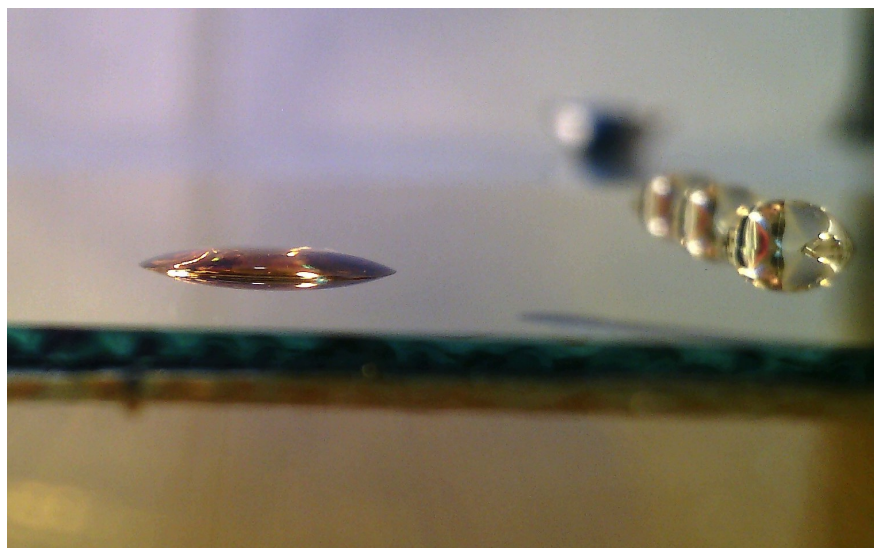
Figure C.1: Example contact angle measurement setup - diiodomethane (foreground) versus water (background) on gold/Parylene C. Glass substrate is rotated so that the liquid is in the middle/center of the image frame for measurement. The same volume of liquid was used for each liquid. A ray tracing image preview software was used to measure contact angle.

Bibliography

[1]   URL: https : / / www . parc . com / parc – forum / gyricon – llc – and – the – world – of – electronic-paper/.

[2]   URL: https://www.samsung.com/global/galaxy/galaxy-fold/.

[3]   URL: https://www.emdgroup.com/en/expertise/displays/solutions/oled-display-materials/oled-technology.html.

[4]   Yasser Khan et al. "Monitoring of Vital Signs with Flexible and Wearable Medical Devices". In: *Advanced Materials* 28 (2016). DOI: 10.1002/adma.201504366.

[5]   Alex Chortos, Jia Liu, and Zhenan Bao. "Pursuing prosthetic electronic skin". In: *Nature Materials* 15 (2016).

[6]   Dae Hyeong Kim et al. "Epidermal electronics". In: *Science* 333.6044 (2011), pp. 838–843. DOI: 10.1126/science.1206157.

[7]   "Flexible tactile sensing based on piezoresistive composites: A review". In: *Sensors* (2014).

[8]   "Flexible transparent conductive materials based on silver nanowire networks: a review". In: *IoT Science Nanotechnology* (2013).

[9]   "A review of fabrication and applications of carbon nanotube film-based flexible electronics". In: *Nanoscale* (2013).

[10] "Technologies for printing sensors and electronics over large flexible substrates: a review". In: *IEEE Sensors* (2014).

[11] "Tactile sensing for dexterous in-hand manipulation in roboticsfffdfffdfffdA review". In: *Sensors and Actuators A: Physical* (2011).

[12] Nanshu Lu. "Mechanics of Hard Films on Soft Substrates". In: *ProQuest Dissertations And Theses* (2009).

[13] Dupont. *Kapton B*. URL: https://www.dupont.com/products/kapton-b.html.

[14] James E. Mark. "Polymer data handbook". In: (2009).

[15] URL: http://www.ti.com/lit/an/sloa033a/sloa033a.pdf.

[16] OMEGA Engineering. *Full-Bridge for Bending or Axial Tension, Transducer-Quality*. URL: https://www.omega.com/en-us/sensors-and-sensing-equipment/pressure-and-strain/strain-gauges/sgt-full-bridge-diaphragm/p/SGT-3G-350-FB13.

[17] URL: https://www.analog.com/en/analog-dialogue/articles/capacitance-sensors-for-human-interfaces-to-electronics.html.

[18] Synaptive Medical. *BrightMatter Guide - Real Time Surgical Navigation*. 2018. URL: https://www.synaptivemedical.com/products/guide/.

[19] Jan Peirs et al. "A micro optical force sensor for force feedback during minimally invasive robotic surgery". In: *Sensors and Actuators, A: Physical* 115 (2004), pp. 447–455. ISSN: 09244247. DOI: 10.1016/j.sna.2004.04.057.

[20] Javad Dargahi and Siamak Najarian. "An integrated force position tactile sensor for improving diagnostic and therapeutic endoscopic surgery". In: *Bio-Medical Materials and Engineering* 14.2 (2004), pp. 151–166.

[21] M. Tavakoli, R.V. Patel, and M. Moallem. "A force reflective master-slave system for minimally invasive surgery". In: *Proceedings 2003 IEEE/RSJ International Conference on Intelligent Robots and Systems (IROS 2003)* (2003). DOI: 10.1109/IROS.2003.1249629.

[22] *MULTI-FORCE SENSING SURGICAL INSTRUMENT AND METHOD OF USE FOR ROBOTC SURGICAL SYSTEMS*. 2017.

[23] Hironobu Takizawa et al. "DEVELOPMENT OF A MICROFINE ACTIVE BENDING CATHETER EQUIPPED WITH MIFTACTILE SENSORS". In: *IEEE MEMS 2019* (1999), pp. 412–417. DOI: 10.1109/memsys.1999.746864.

[24] Roberto Sequeiros et al. "MRI-guided periradicular nerve root infiltration therapy in low-field (0.23-T) MRI system using optical instrument tracking". In: *European Radiology* 12.6 (2002), pp. 1331–1337. DOI: 10.1109/memsys.1999.746864.

[25] Nico Corp. *Navigation stylet for a tissue access system.* 2017.

[26] "Increasing the accuracy of 3D EEG implantations". In: *Journal of Neurosurgery* (2019), pp. 1–8. ISSN: 0022-3085. DOI: 10.3171/2019.2.jns183313.

[27] Fan Yang, Mahdieh Babaisi, and John P. Swensen. "Fracture-Directed Steerable Needles". In: *Journal of Medical Robotics Research* 4.1 (2018). DOI: 10.1142/S2424905X18420023.

[28] Amir Hossein Hadi Hosseinabadi, Mohammad Honarvar, and Septimiu E. Salcudean. "Optical Force Sensing In Minimally Invasive Robotic Surgery". In: *2019 International Conference on Robotics and Automation (ICRA)* (2019). DOI: 10.1109/ICRA.2019.8793589.

[29] "Deflection of Beams by Integration". In: (), pp. 396–419. URL: https://lwlin.me.berkeley.edu/me128/BeamDeflection.pdf.

[30] *Taiker Robot for Kids, Intellectual Gesture Sensor Rechargeable Robot Toys for Kids with Walking, Sliding, Turning, Singing, Dancing, Speaking and Teaching Science.* URL: https://www.amazon.com/Taiker-Intellectual-Rechargeable-Speaking-Teaching/dp/B07PQHN495.

[31] *Sensor Solution Provider - TDK Robot Sensor Solutions.* URL: https://product.tdk.com/info/en/pr/sensor/industry/index.html.

[32] Steve Park et al. "Stretchable energy-harvesting tactile electronic skin capable of differentiating multiple mechanical stimuli modes". In: *Advanced Materials* 26.43 (2014), pp. 7324–7332. DOI: 10.1002/adma.201402574.

[33] Nanshu Lu et al. "Highly sensitive skin-mountable strain gauges based entirely on elastomers". In: *Advanced Functional Materials* 22.19 (2012), pp. 4044–4050. DOI: 10.1002/adfm.201200498.

[34] M. Kim, H. Alrowais, and O. Brand. "All-soft Physical And Chemical Microsystems Based On Liquid Metal For Wearable Electronics Applications". In: *IEEE MEMS 2017* (2017), pp. 1162–1165. DOI: 10.1109/MEMSYS.2017.7863621.

[35] C. Pang. "A flexible and highly sensitive strain-gauge sensor using reversible interlocking of nanofibres". In: *Nature Materials* 11.9 (2012), pp. 795–801. DOI: 10.1038/nmat3380.

[36] Y. Cheng et al. "Stretchable electronic skin based on silver nanowire composite fiber electrodes for sensing pressure, proximity, and multidirectional strain". In: *Nanoscale* 11 (2017). DOI: 10.1039/c7nr00121e.

[37] H.J. Kim, A. Thukral, and C. Yu. "Highly sensitive and very stretchable strain sensor based on a rubbery semiconductor". In: *ACS Applied Material Interfaces* 10.5 (2018), pp. 5000–5006. DOI: 10.1021/acsami.7b17709.

[38] Takao Someya et al. "A large-area, flexible pressure sensor matrix with organic field-effect transistors for artificial skin applications". In: *Proceedings of the National Academy of Sciences of the United States of America* 101.27 (2004), pp. 9966–9970. DOI: 10.1073/pnas.0401918101.

[39] Robert A. Nawrocki et al. "300-nm Imperceptible, Ultraflexible, and Biocompatible e-Skin Fit with Tactile Sensors and Organic Transistors". In: *Advanced Electronic Materials* 2.4 (2016), pp. 2–5. DOI: 10.1002/aelm.201500452.

[40] Lijia Pan et al. "An ultra-sensitive resistive pressure sensor based on hollow-sphere microstructure induced elasticity in conducting polymer film". In: *Nature Communications* 5 (2014). DOI: 10.1038/ncomms4002.

[41] Ang Ke et al. "Fingertip Tactile Sensor with Single Sensing Element Based on FSR and PVDF". In: *IEEE Sensors Journal* 19.23 (2019), pp. 11100–11112. DOI: 10.1109/jsen.2019.2936304.

[42] Barrett Advanced Robotics. *BarrettHand*. 2019. URL: https://advanced.barrett.com/barretthand.

[43] Hao Dang and Peter K. Allen. "Stable grasping under pose uncertainty using tactile feedback". In: *Autonomous Robots* 36 (2014), pp. 309–330. DOI: 10.1007/s10514-013-9355-y.

[44] Chunyan Li et al. "Flexible dome and bump shape piezoelectric tactile sensors using PVDF-TrFE copolymer". In: *Journal of Microelectromechanical Systems* 17.2 (2008), pp. 334–341. DOI: 10.1109/JMEMS.2007.911375.

[45] Francis S Ingraham and D F Wooley. "ROBOTIC TACTILE SENSOR ARRAY FABRI-CATED FROM A PIEZOELECTRIC POLYVINYLIDENE FLUORIDE FILM". In: *Industrial & Engineering Chemistry* 56.9 (1964), pp. 53–55. DOI: 10.1021/ie50657a007. URL: http://dx.doi.org/10.1021/ie50657a007.

[46] "Piezoelectric polymer transducer arrays for flexible tactile sensors". In: *IEEE Sensors Journal* 13.10 (2013), pp. 4022–4029. ISSN: 1530437X. DOI: 10.1109/JSEN.2013.2268690.

[47] "High performance piezoelectric devices based on aligned arrays of nanofibers of poly(vinylidenefluoride-co-trifluoroethylene)". In: *Nature Communications* 4 (2013), p. 1633. DOI: 10.1038/ncomms2639.

[48] D.P.J. Cotton et al. "A novel thick-film piezoelectric slip sensor for a prosthetic hand". In: *IEEE Sensors Journal* 7.5 (2007), pp. 752–761. DOI: 10.1109/JSEN.2007.894912.

[49] Dirk Goeger, Nico Ecker, and Heinz Woern. "Tactile sensor and algorithm to detect slip in robot grasping processes". In: *2008 IEEE International Conference on Robotics and Biomimetics, ROBIO 2008* (2008), pp. 1480–1485. DOI: 10.1109/ROBIO.2009.4913219.

[50] Shouhei Shirafuji and Koh Hosoda. "Detection and prevention of slip using sensors with different properties embedded in elastic artificial skin on the basis of previous experience". In: *Robotics and Autonomous Systems* 62.1 (2014), pp. 46–52. DOI: 10.1016/j.robot.2012.07.016.

[51] Francis S Ingraham and D F Wooley. "ROBOTIC TACTILE SENSOR ARRAY FABRI-CATED FROM A PIEZOELECTRIC POLYVINYLIDENE FLUORIDE FILM". In: *Industrial & Engineering Chemistry* 56.9 (1964), pp. 53–55. DOI: 10.1021/ie50657a007.

[52] LUIGI PINNA. "Charge amplifier design methodology for pvdf-based tactile sensors". In: 22.8 (2013), pp. 1–23. DOI: 10.1142/S0218126613500667.

[53] Woojin Park et al. "Characteristics of a pressure sensitive touch sensor using a piezoelectric PVDF-TrFE/MoS 2 stack". In: *Nanotechnology* 24.47 (2013), p. 475501. DOI: 10.1088/0957-4484/24/47/475501.

[54] Woojin Park et al. "Characteristics of a pressure sensitive touch sensor using a piezoelectric PVDF-TrFE/MoS 2 stack". In: *Nanotechnology* 24.47 (2013), p. 475501. DOI: 10.1088/0957-4484/24/47/475501.

[55] Tushar Sharma et al. "Flexible thin-film PVDF-TrFE based pressure sensor for smart catheter applications". In: *Annals of Biomedical Engineering* 41.4 (2013), pp. 744–751. DOI: 10.1007/s10439-012-0708-z.

[56] Analog Devices. *Circuit Note CN-0350.*

[57] I. Kim. "A photonic sintering derived Ag flake/nanoparticle-based highly sensitive stretchable strain sensor for human motion monitoring". In: *Nanoscale* 10.17 (2018), pp. 7890–7897. DOI: 10.1039/c7nr09421c.

[58] N. Lu et al. "Highly sensitive skin-mountable strain gauges based entirely on elastomers". In: *Advanced Functional Materials* 22.19 (2012), pp. 4044–4050. DOI: 10.1002/adfm.201200498.

[59] Z. Yang. "Graphene Textile Strain Sensor with Negative Resistance Variation for Human Motion Detection". In: *ACS Nano* 12.9 (2018), pp. 9134–9141. DOI: 10.1021/acsnano.8b03391.

[60] J. Oh. "Pressure Insensitive Strain Sensor with Facile Solution-Based Process for Tactile Sensing Applications". In: *ACS Nano* 12 (2018), pp. 7546–7553. DOI: 10.1021/acsnano.8b03488.

[61] Q. Sun et al. "Active matrix electronic skin strain sensor based on piezopotential-powered graphene transistors". In: *Advanced Materials* 27.22 (2015), pp. 3411–3417. DOI: 10.1002/adma.201500582.

[62] M. Sezen et al. "Eliminating Piezoresistivity in Flexible Conducting Polymers for Accurate Temperature Sensing under Dynamic Mechanical Deformations". In: *Small* 12.21 (2016), pp. 2832–2838. DOI: 10.1002/smll.201600858.

[63] Hyung-kew Lee, Sun-il Chang, and Euisik Yoon. "Dual-Mode Capacitive Proximity Sensor for Robot Application : Implementation of Tactile and Proximity Sensing Capability on a Single Polymer Platform Using Shared Electrodes". In: *IEEE Sensors Journal* 9.12 (2009), pp. 1748–1755.

[64] Bo Zhang et al. "Dual functional transparent film for proximity and pressure sensing". In: *Nano Research* 7.10 (2014), pp. 1488–1496. DOI: 10.1007/s12274-014-0510-3.

[65] Yitao Ding, Hongyin Zhang, and Ulrike Thomas. "Capacitive Proximity Sensor Skin for Contactless Material Detection". In: *2018 IEEE/RSJ International Conference on Intelligent Robots and Systems (IROS)* (2018), pp. 7179–7184.

[66] Yin Cheng et al. "Stretchable electronic skin based on silver nanowire composite fiber electrodes for sensing pressure, proximity, and multidirectional strain". In: *Nanoscale* (2017), pp. 3834–3842. DOI: `10.1039/c7nr00121e`.

[67] Rui Rocha et al. "Soft-matter sensor for proximity , tactile and pressure detection". In: *2017 IEEE/RSJ International Conference on Intelligent Robots and Systems (IROS)* i (2017), pp. 3734–3738.

[68] Pei-hsuan Lo et al. "IMPLEMENTATION OF VERTICAL-INTEGRATED DUAL MODE INDUCTIVE-CAPACITIVE PROXIMITY SENSOR". In: *2012 IEEE 25th International Conference on Micro Electro Mechanical Systems (MEMS)* February (2012), pp. 640–643. DOI: `10.1109/MEMSYS.2012.6170268`.

[69] Hosam Alagi, Stefan Escaida Navarro, and Michael Mende. "A Versatile and Modular Capacitive Tactile Proximity Sensor". In: *2016 IEEE Haptics Symposium (HAPTICS)* (2016). DOI: `10.1109/HAPTICS.2016.7463192`.

[70] Il-joo Cho et al. "Compliant Ultrasound Proximity Sensor for the Safe Operation of Human Friendly Robots Integrated with Tactile Sensing Capability". In: 12.1 (2017), pp. 310–316.

[71] Haiting Wang et al. "Ultrasensitive Flexible Proximity Sensor Based on Organic Crystal for Location Detection". In: (2018). DOI: `10.1021/acsami.7b15352`.

[72] Haiting Wang et al. "Ultrasensitive Flexible Proximity Sensor Based on Organic Crystal for Location Detection". In: (2018). DOI: `10.1021/acsami.7b15352`.

[73] Mahmoud Tavakoli et al. "Autonomous Selection of Closing Posture of a Robotic Hand Through Embodied Soft Matter Capacitive Sensors". In: 17.17 (2017), pp. 5669–5677.

[74] Fan Xia et al. "Tri-Mode Capacitive Proximity Detection Towards Improved Safety in Industrial Robotics". In: *IEEE Sensors Journal* 18.12 (2018), pp. 5058–5066. DOI: `10.1109/JSEN.2018.2832637`.

[75] Yitao Ding, Hongyin Zhang, and Ulrike Thomas. "Capacitive Proximity Sensor Skin for Contactless Material Detection". In: (2018), pp. 7179–7184.

[76] R Thorn. "Design of sensor electronics for electrical capacitance tomography". In: *Environmental Science & Technology* 31.9 (1997), 395A. ISSN: 09563768. DOI: 10.1021/es972426s.

[77] Wuqiang Yang. "Design of electrical capacitance tomography sensors". In: *Measurement Science and Technology* 21.4 (2010). ISSN: 00223093. DOI: 10.1016/j.jnoncrysol.2010.04.040.

[78] I. Saied and M. Meribout. "Electronic hardware design of electrical capacitance tomography systems". In: *Philosophical Transactions of the Royal Society A: Mathematical, Physical and Engineering Sciences* 374.2070 (1996). ISSN: 1364503X. DOI: 10.1098/rsta.2015.0331.

[79] W. Q. Yang et al. "An image-reconstruction algorithm based on Landweber's iteration method for electrical-capacitance tomography". In: *Measurement Science and Technology* 10.11 (1999), pp. 1065–1069. ISSN: 09570233. DOI: 10.1088/0957-0233/10/11/315.

[80] Zhang Cao et al. "Electrical capacitance tomography for sensors of square cross sections using Calderon's method". In: *IEEE Transactions on Instrumentation and Measurement* 60.3 (2011), pp. 900–907. ISSN: 00189456. DOI: 10.1109/TIM.2010.2045255.

[81] "Nonlinear image reconstruction for electrical capacitance tomography using experimental data". In: *Measurement Science and Technology* 16.10 (2005), pp. 1987–1996. ISSN: 09570233. DOI: 10.1088/0957-0233/16/10/014.

[82] Chao Tan et al. "Image Reconstruction Based on Convolutional Neural Network for Electrical Resistance Tomography". In: *IEEE Sensors Journal* (2018). DOI: 10.1109/JSEN.2018.2876411.

[83] Stefania Russo et al. "Touch Position Detection in Electrical Tomography Tactile Sensors Through Quadratic Classifier". In: *IEEE Sensors Journal* 19.2 (2018), pp. 474–483. DOI: 10.1109/JSEN.2018.2878774.

[84] Fan Xia, Behraad Bahreyni, and Fabio Campi. "Multi-functional capacitive proximity sensing system for industrial safety applications". In: *Proceedings of IEEE Sensors* (2017), pp. 1–3. ISSN: 21689229. DOI: 10.1109/ICSENS.2016.7808496.

[85] "CapSeat - Capacitive Proximity Sensing for Automotive Activity Recognition ". In: *Proceedings of the 7th International Conference on Automotive User Interfaces and Interactive Vehicular Applications* (2015). DOI: `10.1145/2799250.2799263`.

[86] Fan Xia et al. "Tri-Mode Capacitive Proximity Detection Towards Improved Safety in Industrial Robotics". In: *IEEE Sensors Journal* 18.12 (2018), pp. 5058–5066. DOI: `10.1109/JSEN.2018.2832637`.

[87] M Stephan et al. "Short Range Capacitive Proximity Sensing". In: *IROS 2015 Workshop on Alternative Sensing for Robot Perception (WASRoP)* ().

[88] Kurt Bryan and Tanya Leise. "Impedance Imaging, Inverse Problems, and Harry Potter's Cloak". In: *SIAM Rev.* 52.2 (2010), pp. 359–377. DOI: `10.1137/090757873`.

[89] C.C. Bell. "An Efference Copy Which is Modified by Reafferent Input". In: 784.45 (1981).

[90] Ann Kennedy et al. "A temporal basis for predicting the sensory consequences of motor commands in an electric fish". In: *Nature Neuroscience* 17 (2014), pp. 416–422. DOI: `10.1021/nl061786n.Core-Shell`.

[91] Tim Requarth and Nathaniel B. Sawtell. "Plastic Corollary Discharge Predicts Sensory Consequences of Movements in a Cerebellum-Like Circuit". In: *Neuron* 82.4 (2014), pp. 896–907. DOI: `10.1016/j.neuron.2014.03.025`.

[92] URL: `https://sawtell-lab.neuroscience.columbia.edu/content/gallery`.

[93] Jinmo Jeong, Namsun Chou, and Sohee Kim. "Long-term characterization of neural electrodes based on parylene-caulked polydimethylsiloxane substrate". In: *Biomedical Microdevices* 18.3 (2016). ISSN: 15728781. DOI: `10.1007/s10544-016-0065-z`.

[94] "A lithographically-patterned, elastic multi-electrode array for surface stimulation of the spinal cord". In: *Biomedical Microdevices* 10.2 (2008), pp. 259–269. DOI: `10.1007/s10544-007-9132-9`.

[95] Jonathan Viventi et al. "Flexible, foldable, actively multiplexed, high-density electrode array for mapping brain activity in vivo". In: *Nature Neuroscience* 14.12 (2011), pp. 1599–1605. DOI: `10.1038/nn.2973`.

[96] Dhananjay Bodas and Chantal Khan-Malek. "Formation of more stable hydrophilic surfaces of PDMS by plasma and chemical treatments". In: *Microelectronic Engineering* 83 (2006), pp. 1277–1279. DOI: `10.1016/j.mee.2006.01.195`.

[97] *Technical Note - So You Want to Measure Surface Energy?* URL: `https://www.kruss-scientific.com/fileadmin/user_upload/website/literature/kruss-tn306-en.pdf`.

[98] Jean Pierre Montheard, Michel Chatzopoulos, and Daniel Chappard. "2-Hydroxyethyl methacrylate (hema): Chemical properties and applications in biomedical fields". In: *Journal of Macromolecular Science, Part C* 32.1 (1992), pp. 1–33. ISSN: 15205746. DOI: `10.1080/15321799208018377`.

[99] W. Ding et al. "Improve Efficiency and Reliability in Single-Hop WSNs with Transmit-Only Nodes". In: *Science of The Total Environment* 541 (Jan. 2016), pp. 1191–1199. DOI: `10.1016/j.scitotenv.2015.09.150`.

[100] "Stormwater infiltration capacity of street tree pits: Quantifying the influence of different design and management strategies in New York City". In: *Ecological Engineering* (2018), pp. 157–166.

[101] "EcoBT: Miniature, versatile mote platform based on bluetooth low energy technology". In: *2014 IEEE Int. Conf. Internet Things* (2014).

[102] "Wristband Vital: A wearable multi-sensor microsystem for real-time assistance via low-power Bluetooth link". In: *IEEE World Forum Internet Things* (2016).

[103] "CheepSync: A Time Synchronization Service for Resource Constrained Bluetooth Low Energy Advertisers". In: *14th Int. Conf. - IPSN fffdfffdfffd15* (2015).

[104] M. Collotta and G. Pau. "A Novel Energy Management Approach for Smart Homes Using Bluetooth Low Energy". In: *IEEE Journal on Selected Areas in Communications* 33.12 (2015), 2988fffdfffdfffd2996. DOI: `10.1109/JSAC.2015.2481203`.

[105] Johanna Nieminen et al. "Networking Solutions for Connecting Bluetooth Low Energy Enabled Machines to the Internet of Things". In: *IEEE Network* 28.6 (2015), pp. 83–90. DOI: `10.1109/MNET.2014.6963809`.

[106] Jonathon Furst et al. "Leveraging physical locality to integrate Smart appliances in non-residential buildings with ultrasound and Bluetooth Low Energy". In: *2016 IEEE First International Conference on Internet-of-Things Design and Implementation (IoTDI)* (2016). DOI: `10.1109/IoTDI.2015.35`.

[107] Hideki Matsuoka et al. "Development of A Control System for Home Appliances Based on BLE Technique". In: *2014 IEEE International Symposium on Independent Computing (ISIC)* (2014). DOI: `10.1109/INDCOMP.2014.7011751`.

[108] "Wireless sensor network based smart home: Sensor selection, deployment and monitoring". In: *IEEE Sens. App. Symp.* (2013).

[109] "Building the Internet of Things with bluetooth smart". In: *Ad Hoc Networks* (2016).

[110] B. Błaszczyszyn and B. Radunovic. "Using transmit-only sensors to reduce deployment cost of wireless sensor networks". In: *Proc. of IEEE INFOCOM'08* (Apr. 2008).

[111] Bernhard Firner. *Transmit only for dense wireless networks.* Ph.D. dissertation, Rutgers University. 2014.

[112] J. Zhao et al. "Improve Efficiency and Reliability in Single-Hop WSNs with Transmit-Only Nodes". In: *IEEE Trans. Parallel and Distributed Systems* 24.3 (Mar. 2013), pp. 520–534. ISSN: 1045-9219. DOI: `10.1109/TPDS.2012.148`.

[113] H. C. Keong, K. M. S. Thotahewa, and M. R. Yuce. "Transmit-Only Ultra Wide Band Body Sensors and Collision Analysis". In: *IEEE Sensors J.* 13.5 (May 2013), pp. 1949–1958. DOI: `10.1109/JSEN.2013.2245562`.

[114] K. Han and K. Huang. "Wirelessly Powered Backscatter Communication Networks: Modeling, Coverage, and Capacity". In: *IEEE Trans. Wireless Communications* 16.4 (Apr. 2017), pp. 2548–2561. ISSN: 1536-1276. DOI: `10.1109/TWC.2017.2665629`.

[115] Constantinos Kolias et al. "Breaking BLE Beacons For Fun But Mostly Profit". In: *Proc. ACM EuroSec'17.* Belgrade, Serbia: ACM, 2017. ISBN: 978-1-4503-4935-2. DOI: `10.1145/3065913.3065923`. URL: `http://doi.acm.org/10.1145/3065913.3065923`.

[116] K. E. Jeon et al. "BLE Beacons for Internet of Things Applications: Survey, Challenges, and Opportunities". In: *IEEE Internet of Things Journal* 5.2 (Apr. 2018), pp. 811–828. DOI: 10.1109/JIOT.2017.2788449.

[117] M. Gorlatova, R. Aiello, and S. Mangold. "Managing Base Station Location Privacy". In: *Proc. IEEE Military Communications Conference (MILCOM'11)*. Nov. 2011.

[118] URL: https://www.bluetooth.com/specifications/bluetooth-core-specification/technical-considerations.

[119] "Timing Channels in Bluetooth Low Energy". In: *IEEE Comm. Lett.* (2016).

[120] *Generic Attributes (GATT) and the Generic Attribute Profile*. 2016. URL: https://www.bluetooth.com/specifications/generic-attributes-overview.

[121] "A Measurement Study of BLE iBeacon and Geometric Adjustment Scheme for Indoor Location-Based Mobile Applications". In: *Mobile Information Systems* (2016).

[122] A. Dementyev et al. "Power Consumption Analysis of Bluetooth Low Energy, ZigBee and ANT Sensor Nodes in a Cyclic Sleep Scenario". In: (2013).

[123] "Enhancing iBeacon based micro-location with particle filtering". In: *IEEE Glob. Commun. Conf. GLOBECOM* (2015).

[124] "Preliminary Design for Sustainable BLE Beacons Powered by Solar Panels". In: *INFOCOM WKSHPS* (2016).

[125] "Cinamin : A Perpetual and Nearly Invisible BLE Beacon". In: *EWSN '16 Proc. of the 2016 Int. Conf. on Embedded Wireless Systems and Networks* (2016).

[126] *Bluetooth Low Energy Beacons*. URL: http://www.ti.com/lit/an/swra475a/swra475a.pdf.

[127] "IoT enabled Environmental Monitoring System for Smart Cities". In: *2016 International Conference on Internet of Things and Applications (IOTA)* (2016), pp. 383–388.

[128] *PSoC 4 Die Temperature (DieTemp)*. URL: http://www.cypress.com/file/139101/download.

[129] "Design and characterization of a low thermal drift capacitive humidity sensor by inkjet-printing". In: *Sensors Actuators, B: Chem.* (2014).

[130] "Low drift MEMS humidity sensor by intermittent heating". In: *IEEE Int. Meet. for Future of Electron Devices* (2015).

[131] *Capsense Controller*. URL: http://www.cypress.com/products/capsense-controllers.

[132] C. J. Walsh, T. D. Fletcher, and M. J. Burns. "Urban Stormwater Runoff: A New Class of Environmental Flow Problem". In: *PLOS ONE* 7.9 (2018), e45814–e45814.

[133] *Green Infrastructure - Rain Garden*. https://www1.nyc.gov/site/dep/water/rain-gardens.page.

[134] *Platinum RTD Sensor - PT100 - 3 Wire 1 meter long*. URL: https://www.adafruit.com/product/3290.

[135] Bita Alizadehtazi et al. "Comparison of Observed Infiltration Rates of Different Permeable Urban Surfaces Using a Cornell Sprinkle Infiltrometer". In: *Journal of Hydrologic Engineering* 21.7 (2016), pp. 06016003-1–06016003-5.

[136] T. B. Carson et al. "Hydrological performance of extensive green roofs in New York City: observations and multi-year modeling of three full-scale systems". In: *Environ. Res. Lett.* 8 (2013), pp. 1–13.

[137] Bilal Shabandri, Sahith Reddy Madara, and Piyush Maheshwari. *IoT-Based Smart Tree Management Solution for Green Cities*. Springer, 2016.

[138] Vaibhav Bhatnagar and Ramesh Chandra. *IoT-Based Soil Health Monitoring and Recommendation System*. Springer, 2016.

[139] Baris N. Ozbay et al. "3D multiphoton fiber-coupled microscopy using adaptable optics for brain imaging". In: *2016 Conference on Lasers and Electro-Optics, CLEO 2016* (2016), pp. 1–2.

[140] Baris N. Ozbay et al. "Three dimensional two-photon brain imaging in freely moving mice using a miniature fiber coupled microscope with active axial-scanning". In: *Scientific Reports* 8.1 (2018), pp. 1–14. ISSN: 20452322. DOI: 10.1038/s41598-018-26326-3. URL: http://dx.doi.org/10.1038/s41598-018-26326-3.

[141]   Anan Li, David H. Gire, and Diego Restrepo. "ϒ Spike-Field Coherence in a Population of Olfactory Bulb Neurons Differentiates Between Odors Irrespective of Associated Outcome". In: *Journal of Neuroscience* 35.14 (2015), pp. 5808–5822. ISSN: 15292401. DOI: 10.1523/JNEUROSCI.4003-14.2015.

[142]   Soraya Terrab et al. "Adaptive electrowetting lens-prism element". In: *Optics Express* 23.20 (2015), p. 25838. ISSN: 1094-4087. DOI: 10.1364/oe.23.025838.

[143]   M.D. Benoy et al. "Thickness dependence of the properties of indium tin oxide (ITO) films prepared by activated reactive evaporation". In: *Brazilian Journal of Physics* 39.4 (2009). DOI: 10.1590/S0103-97332009000600003.

[144]   Jonathan J. Wilson et al. "Three-Dimensional Representation of Motor Space in the Mouse Superior Colliculus". In: *Current Biology* 28.11 (2018), 1744–1755.e12. ISSN: 09609822. DOI: 10.1016/j.cub.2018.04.021. URL: https://doi.org/10.1016/j.cub.2018.04.021.

[145]   Subramaniam Venkatraman et al. "Investigating Neural Correlates of Behavior in Freely Behaving Rodents Using Inertial Sensors". In: *Journal of Neurophysiology* 104.1 (2010), pp. 569–575. ISSN: 0022-3077. DOI: 10.1152/jn.00121.2010.

[146]   Shobhit Singla et al. "A cerebellum-like circuit in the auditory system cancels responses to self-generated sounds." In: *Nature Neuroscience* 20 (2017).